Università di Pisa

Facoltà di Scienze Matematiche Fisiche e Naturali

Dipartimento di Fisica "E. Fermi"

Tesi di Laurea Magistrale in Fisica della Materia

Optical dipole trap for an erbium and dysprosium mixture

Relatore esterno:

Prof.ssa Francesca Ferlaino
(University of Innsbruck)

Candidato:

Claudia Politi
Matr. 527904

Relatore interno:

Prof.ssa Donatella Ciampini

Anno Accademico 2016/2017

Alla mia famiglia, la mia forza.

Contents

Introduction

At extremely low temperatures, on the order of a billionth of degree above the absolute zero, nine orders of magnitude lower than the coldest temperature of the universe, atomic gases reveal their quantum nature. In 1925 Satyendra Nath Bose and Albert Einstein predicted the appearance of a new state of matter, the Bose-Einstein condensate (BEC) [15, 27]. In this state, atoms occupy the same lowest energy level and display their wave-like properties, forming one macroscopic quantum mechanical wave. For decades scientists thought that the low temperatures needed to reach the BEC regime could never be achieved in laboratories. After the invention of the laser and the development of new laser cooling and trapping techniques in 1995, 70 years after the theoretical prediction, the first BEC was achieved at JILA [5] and shortly after at MIT [24]. Among these new techniques, the fundamental tool that enabled scientists to reach such low temperatures was the evaporative cooling. For fermions, that behave differently with respect to bosons, it took four years more to achieve the first quantum degenerate gas in 1999 [26]. In this case, due to the Pauli exclusion principle, atoms do not "condense" in the same state, rather they fill the lowest energy levels with at most one particle per state.

Ultracold atoms, confined in traps formed of magnetic fields and laser beams, provide ideal systems in which few- and many-body physics can be investigated with high control of internal and external degrees of freedom. In experiment, this is done through the use of Feshbach resonances as a "knob" to tune the interparticle interactions [19], or actively controlling the traps to change the dimensionality of the system. In the last decades, the interest in using ultracold gases for several applications grew enormously. One of the most exciting one, suggested by Feynman in 1981 [29], regards the use of these highly controllable quantum systems to simulate quantum phenomena in nature that are too complex to fully understand or simulate with standard computer, e. g. high temperature superconductivity [72]. Furthermore, laser beams can be combined in several ways to create artificial lattices, in which ultracold atoms can be easily manipulated to study solid-state problems. Other applications are precision measurements [75] and the development of atomic clocks [14], which are involved in our daily life as standard reference for GPS.

Since 1995 the field of ultracold gases keeps expanding with the addition of new ingredients, e. g. dipole-dipole interactions [9], atoms in highly excited states (Rydberg atoms) [56] or systems in which the spin becomes a new degree of freedom (spinor gases) [61]. The first experiments with ultracold gases used alkali atoms, whose interactions, at low temperatures, have a short-range and isotropic character. On the contrary, dipolar gases exhibit an additional interaction, the dipole-dipole interaction (DDI), which is long-range and anisotropic. The geometry-dependence provides a new "knob" to manipulate the interactions. The experimental studies on dipolar gases started in 2005 with the Bose-Einstein condensation of chromium [34]. The exciting results determined by the presence of the DDI encouraged scientists in further investigation of dipolar systems. Since the dipolar strength is higher for large mass and high magnetic moment, several groups have switched to heavy and strongly magnetic lanthanides to study systems with dominating dipolar interactions. The first lanthanide to be "condensed" was dysprosium [58] in 2011 by the group of B. Lev in Stanford and a year later erbium [3] was brought to the quantum degeneracy in Innsbruck by the group of F. Ferlaino.

The RARE experiment (Rydberg Atoms with Rare Earths) in Innsbruck, where this thesis work has been performed, is the first mixture experiment that combines two strongly magnetic atomic species, erbium and dysprosium. Both have several bosonic and fermionic isotopes with high abundances, which allow the study of Bose-Bose, Bose-Fermi and Fermi-Fermi mixtures. The energy spectra with similar cooling transitions and the similar atomic properties, such as mass and melting temperatures, enable a comparatively easy double-species implementation. Three science chambers, connected to each other by optical transport, will be implemented: main chamber, Rydberg chamber and single-site imaging chamber. This will allow us for the investigation of dipolar behaviour of rare earth atoms not only in the lowest energy state (main chamber) but also in highly excited states (Rydberg chamber). Furthermore, in the single-site imaging chamber, an high resolution imaging system will enable us to manipulate and control the two species on the single-atom level.

When I joined the group in October 2016, the main chamber was just implemented and, soon after, the experiment was at the stage of MOT lights implementation and achievement of our first Dy MOT. Thus, it was the time to develop and implement trapping scheme to simultaneously confine Er and Dy and to then further cool the mixture to quantum degeneracy. The design and the realization of such optical dipole trap is the subject of my thesis. The structure of the thesis is the following:

Chapter 1 introduces the basic properties of erbium and dysprosium as the particular electronic configurations and energy spectra, which lead to their strongly magnetic nature. Furthermore, it describes the main features of dipole-dipole interactions.

Chapter 2 gives the theoretical description of atoms trapping by means of far detuned laser beams and the introduction of the tools necessary to characterize it. Particular emphasis is given to one of the key quantities involved in atom-light interaction, the atomic polarizability.

Chapter 3 describes the experimental realization of the optical dipole trap and its tunable geometry. The tunability is obtained using a time-averaged potential created by an acousto-optic deflector. This feature is a fundamental tool to investigate phenomena triggered by the anisotropic character of the DDI. It is used to increase the loading efficiency of the ODT reaching the "mode-matching" condition with the magneto-optical trap. Additionally, it can be used to tune the elastic collision rate and maximize the efficiency of the evaporative cooling necessary to reach the degenerate regime.

Chapter 4 gives an overview of the RARE apparatus and describes the implementation of the optical setup in the experiment and a preliminary characterization of the optical dipole trap, e. g. loading efficiency of atoms and trap frequency measurements.

Chapter 1

Properties of erbium and dysprosium

Erbium and dysprosium are both rare-earth metals and they belong to the group of lanthanides[1]. Despite from their name, rare-earth elements have quite high abundance, e. g. cerium is the 25$^{\text{th}}$ most abundant element in nature, while dysprosium (Dy) and erbium (Er) are the 43$^{\text{rd}}$ and 45$^{\text{th}}$, respectively. In nature, they are found together in form of alloy and it is quite difficult to isolate one from the other, indeed the name dysprosium has Greek origins and it means "hard to get".

These elements got their name for historical reasons, in fact in the 19$^{\text{th}}$ century only one deposit of rare earths, located in Sweden, was known. This explains the adjective "rare", but why "earth"? Rare-earth elements were mainly extracted as oxide that in French was known as "terre" while in German "erde" which means "earth" [85]. Erbium and dysprosium are both extensively used for technological applications.

Er has attracted particular attention as a dopant for YAG crystals and phosphate glasses to produce lasers with an output wavelength of 2.9 μm and 1.54 μm, respectively. Both wavelengths are absorbed by water, leading to interest in medical applications and eye safe military range-finders[2] [11]. In the lately years erbium played also an important role enhancing the energy conversion efficiency in solar cells. Indeed Er^{3+} ions convert the photons with an energy that exceeds the bandgap of the absorber, which typically would be transformed in heat, into infrared photons [76].

Dy is usually added to neodymium to produce the strongest permanent magnets and it is also used as a dopant in different hosts for laser applications.

In this chapter the first section introduces the basic properties of Er and Dy as lanthanides. The second and third sections treat the electronic configuration and the energy spectrum,

---

[1]Not all the rare-earth elements are lanthanides, i. e. scandium and yttrium belong to this group just because of the similar chemical properties.

[2]The water present in the eyes absorbs the light before it reaches the retina.

respectively. Finally, the last section is devoted to the interaction between highly magnetic atoms.

1.1   Basic properties

Dysprosium has an atomic number $Z = 66$ and an atomic mass of $162.50\,\mathrm{u}^3$, while erbium has $Z = 68$ and an atomic mass of $167.26\,\mathrm{u}$, see Fig. 1.1.

Lanthanum 57	Cerium 58	Praseodymium 59	Neodymium 60	Promethium 61	Samarium 62	Europium 63	Gadolinum 64	Terbium 65	Dysprosium 66	Holmium 67	Erbium 68	Thulium 69	Yitterbium 70	Lutetium 71
La	Ce	Pr	Nd	Pm	Sm	Eu	Gd	Tb	Dy	Ho	Er	Tm	Yb	Lu
138.91	140.12	140.91	144.24	145	150.36	151.96	157.25	158.93	162.50	164.93	167.26	168.93	173.05	174.97

Figure 1.1 Periodic table's row of lanthanides. Dy has an atomic number $Z = 66$ and an atomic mass of $162.50\,\mathrm{u}$, while Er has $Z = 68$ and an atomic mass of $167.26\,\mathrm{u}$.

Erbium and dysprosium have several bosonic and fermionic stable isotopes[4]. In Table 1.1 all the stable isotopes and their abundances are listed.

Table 1.1 Relative abundances and type of quantum statistics for all stable isotopes of Er and Dy. B and F stand for bosonic and fermionic statistics, respectively .

	Isotope	Abundance (%)	Statistics
Erbium	^{162}Er	0.14	B
	^{164}Er	1.61	B
	^{166}Er	33.6	B
	^{167}Er	23.0	F
	^{168}Er	26.8	B
	^{170}Er	15.0	B
Dysprosium	^{156}Dy	< 0.1	B
	^{158}Dy	< 0.1	B
	^{160}Dy	2.3	B
	^{161}Dy	18.9	F
	^{162}Dy	25.5	B
	^{163}Dy	24.9	F
	^{164}Dy	28.3	B

$^3 1\,\mathrm{u} = 1.660\,540\,2 \times 10^{-27}\,\mathrm{kg}$.

^{4}Among the rare-earth elements only promethium has no stable isotopes.

Another important property of erbium and dysprosium is their large magnetic moment of $7\,\mu_B$ and $10\,\mu_B$, respectively, where μ_B is the Bohr magneton[5]. Among the rare-earth elements also europium ($7\,\mu_B$), terbium ($10\,\mu_B$) and holmium ($9\,\mu_B$) present this feature. For comparison, alkali atoms, which are extensively used as quantum gas, have magnetic moments of the order of $1\,\mu_B$ in the ground state. The main reason for this is that the electronic ground state of Er and Dy has a large total angular momentum, as will be shown in the next sections.

1.2 Electronic configuration

The ground-state electronic configuration of the rare-earth atoms consists of a core identical to xenon plus additional electrons in orbits with higher energy, as shown below:

$$[1s^2 2s^2 2p^6 3s^2 3p^6 3d^{10} 4s^2 4p^6 4d^{10} 5s^2 5p^6]_{Xe}\ 4f^m 6s^2$$

where m is the index representing the number of electrons occupying the $4f$ shell.

Starting from the electronic configuration of xenon, the rare-earth atoms fill the inner vacant $4f$ orbits, e. g. the first is cerium with $m = 1$, erbium and dysprosium instead have $m = 12$ and $m = 10$, respectively. Due to the Madelung rule, electrons occupy the $6s$ orbital ($n + l = 6$) before the $4f$ ($n + l = 7$) that remains an open shell. This type of electronic configuration is called *submerged-shell*.

Figure 1.2 displays the angular dependence of the 4f electronic wavefunction, which is highly anisotropic in comparison to the spherically symmetric cloud of alkali and alkaline-earth atoms. This is the origin of a strongly anisotropic van der Waals potential [43] and it plays an important role on the interaction between light and atoms, as it will be mentioned in Chapter 2.

1.3 Energy spectrum

The bosonic isotopes of Er and Dy have nuclei with an even number of protons and neutrons, this causes a zero nuclear spin $\mathbf{I}$. On the other hand, fermionic isotopes have an even number of protons and an odd number of neutrons leading to a nuclear spin $\mathbf{I} = 5/2$ and $\mathbf{I} = 7/2$ for Dy and Er, respectively. Due to a non zero nuclear spin $\mathbf{I}$, the total angular momentum $\mathbf{J}$ couples with $\mathbf{I}$ giving rise to the hyperfine structure. This chapter will focus mainly on the

---

[5]The Bohr magneton is defined as $\mu_B = \frac{e\hbar}{2m_e}$, where e and m_e are the elementary charge and the electron mass.

(a) $m_l = 0$ (b) $m_l = 1$ (c) $m_l = 2$ (d) $m_l = 3$
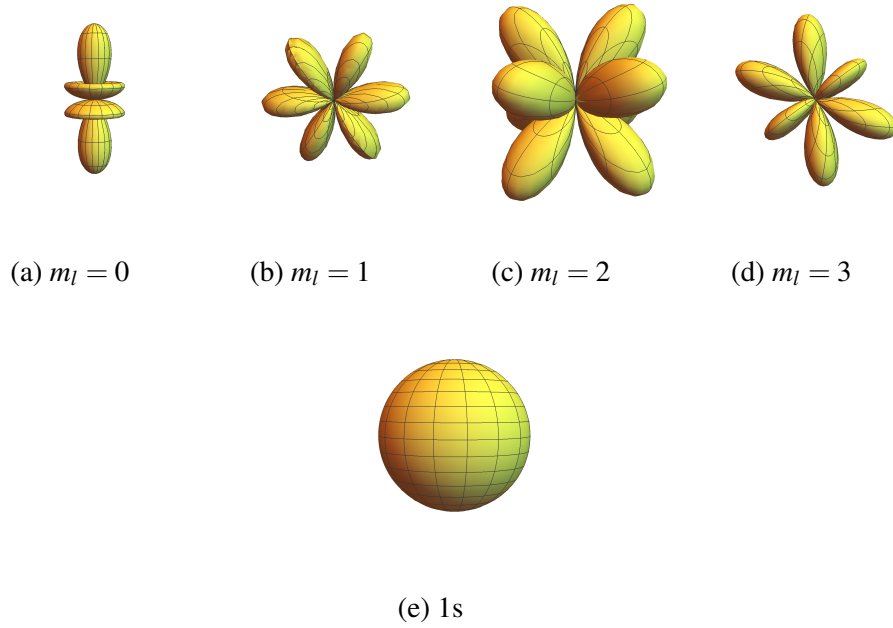
(e) 1s

Figure 1.2 Angular dependence of the $4f$ wavefunction in the four different m_l states. The electronic clouds manifest a high anisotropy, which clearly affects the properties of rare-earth elements [36].

properties of bosonic isotopes since all the measurements of this thesis work are performed with bosons.

According to Hund's rules, in the state with the lowest energy, electrons have to fill the $4f$ orbital[6] in the following way:

- the multiplicity, defined as $2\mathbf{S} + 1$, and so the total spin $\mathbf{S}$, has to be maximized;

- for fixed $\mathbf{S}$, the angular momentum $\mathbf{L}$ has to be maximized;

- finally, for Er and Dy, which have the outermost subshell more than half filled, the total angular momentum $\mathbf{J}$ has to be maximized;

This leads to a ground state with

$$\mathbf{L} = 5, \quad \mathbf{S} = 1, \quad \mathbf{J} = 6 \qquad \text{for Er.}$$
$$\mathbf{L} = 6, \quad \mathbf{S} = 2, \quad \mathbf{J} = 8 \qquad \text{for Dy.}$$

In the Russel-Saunders coupling scheme ($^{2S+1}L_J$) the ground states are written as $^3H_6$ and $^5I_8$ for Er and Dy, respectively. The angular momentum is large compared to the ground state with $L = 0$ of the alkali and alkaline-earth atoms, as listed in Table 1.2.

---

[6]Only electrons in the unfilled shell ("open shell") have to be considered.

Erbium and dysprosium present two and four vacancies in the $4f$ orbital, respectively. According to the first Hund's rule[7], these unpaired electrons are aligned in the states $m_l = 2, 3$ for Er and $m_l = 0, 1, 2, 3$ for Dy with the spin in the same direction and this gives rise to their large magnetic moment. The presence of unpaired electrons is also the reason why the spectrum of rare-earths is so complex compared to the case of alkali and alkali-earth elements. Indeed, in the case of lanthanides, several transitions can take place involving the $4f$ electrons together with other valence electrons.

Table 1.2 Ground state of different elements belonging to the group of alkali, alkaline-earth and rare-earths, which have been "Bose-Einstein-condensed". Dy and Er have a large angular momentum **L** in the ground state with respect to other species.

Element	Electronic configuration	Ground state
Lithium	$[He]2s^1$	$^2S_{\frac{1}{2}}$
Sodium	$[Ne]3s^1$	$^2S_{\frac{1}{2}}$
Potassium	$[Ar]4s^1$	$^2S_{\frac{1}{2}}$
Rubidium	$[Kr]5s^1$	$^2S_{\frac{1}{2}}$
Caesium	$[Xe]6s^1$	$^2S_{\frac{1}{2}}$
Calcium	$[Ar]4s^2$	$^1S_0$
Strontium	$[Kr]5s^2$	$^1S_0$
Dysprosium	$[Xe]4f^{10}6s^2$	$^5I_8$
Erbium	$[Xe]4f^{12}6s^2$	$^3H_6$

Figure 1.3 shows the energy spectrum of Er and Dy up to an energy of $E = h \times 749\,\text{THz}$, which corresponds to the wavenumber $k = 25\,000\,\text{cm}^{-1}$. The levels shown in red (black) present an even (odd) parity. According to the selection rules, optical dipole transitions can only couple the ground state $J = 6$ with $J = [5, 7]$ and the state $J = 8$ with $J = [7, 9]$ for erbium and dysprosium, respectively.

In the Er-Dy experiment atoms are laser cooled in a first stage with resonant light. This stage includes the transversal cooling (TC), in which the atomic beam is optically collimated and the Zeeman slower (ZS) which reduces the velocity of the atoms in such a way to be captured by the magneto optical trap (MOT). In the picture the broad transitions chosen for ZS and TC $(401\,\text{nm}, 421\,\text{nm})$[8] are shown in light blue, while the narrow lines chosen

---

[7]The first Hund's rule is also known as the "bus seat rule" because electrons, like the bus passengers, first tend to singly occupy all the double seats.

[8]A broad transition, which is characterized by short lifetime of the excited state, is more suited for the ZS because it guarantees a large number of scattering events with the light. On the other hand, a narrow line is more suited for the MOT because it leads to lower temperature achievable. The request is that the velocity of the atoms coming from the ZS has to be close to the capture velocity of the MOT.
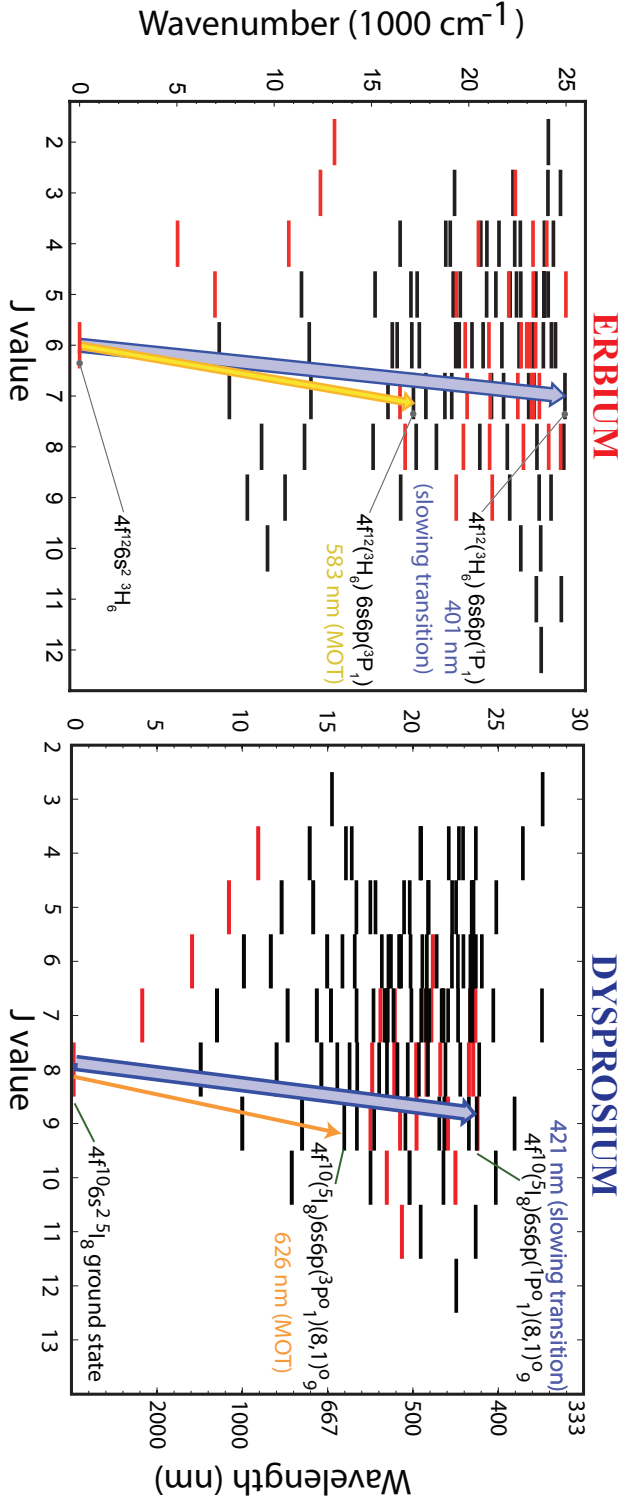
Figure 1.3 Energy spectrum of erbium and dysprosium [8, 87]. The levels shown in red (black) have an even (odd) parity. The ground state, which has an even parity, according to the selection rules, can only be coupled to an energy level with a total angular momentum within the interval $J = [5, 7]$ for erbium and $J = [7, 9]$ for dysprosium and with an odd parity. The broad cooling transitions used for the Zeeman slower and transversal cooling (401 nm, 421 nm) are displayed in light blue, while in yellow and orange are shown the narrow lines used for the magneto optical trap (583 nm, 626 nm) for erbium and dysprosium, respectively. To trap both species and reach the degeneracy, an optical dipole trap running at a wavelength of 1064 nm was chosen.

for the MOT (583 nm, 626 nm) are shown in yellow and orange for Er and Dy, respectively. The energy spectrum of Er and Dy shows similar cooling transitions. The informations regarding the lines used for cooling are listed in Table 1.3. After the laser-cooling stage, the mixture is loaded into an optical dipole trap (ODT). This is a conservative potential and the wavelength (λ) of the ODT should be far off resonance. Thus, an ODT running at a wavelength of 1064 nm was chosen for the optical trapping and the evaporative cooling to reach the degenerate phase of both species.

Table 1.3 Wavenumber, wavelength, linewidth of the cooling transition and the Doppler temperature used for the Zeeman slower and the magneto optical trap of Er and Dy [18].

	Wavenumber (cm^{-1})	Wavelength (nm)	Linewidth (MHz)	T_{Doppler} (μK)
Erbium	24943.272	401	29.7	714
	17157.307	583	0.19	4.6
Dysprosium	23736.61	421	32.2	773
	17727.15	626	0.136	3.3

1.4   Dipole-dipole interaction

The interaction potential between two atoms, in a first order approximation, is given by the van der Waals potential

$$U_{\text{vdW}}(r) = -\frac{C_6}{r^6}, \tag{1.1}$$

where r is the internuclear distance and C_6 is the van der Waals coefficient.

For a potential that scales as r^{-6} the total scattering cross section becomes negligible for partial waves with $l \neq 0$ as the wavenumber k approaches zero, so in the limit of vanishing collision energy. Therefore, in the case of ultracold quantum gases usually only s-waves scattering play a role [69].

The real interatomic potential can then be replaced by a pseudo-potential which is fully described by a single parameter: the s-wave scattering length a [22]. These potentials are short-range and isotropic and the pseudo-potential is usually referred as *contact interaction*

$$U_{\text{contact}}(r) = \frac{4\pi\hbar^2 a}{m}\delta(r), \tag{1.2}$$

where m is the atomic mass.

In the case of highly magnetic atoms, like Er and Dy, it has been shown [9] that the interatomic potential has also a second contribution which is long-range and anisotropic: the *dipole-dipole interaction* (DDI).

The interaction potential between two dipoles with magnetic moment μ_1 and μ_2 pointing in direction $\mathbf{e_1}$ and $\mathbf{e_2}$, respectively, is expressed by the following relation

$$U_{\text{DDI}}(r) = \frac{C_{\text{dd}}}{4\pi} \frac{(\mathbf{e_1} \cdot \mathbf{e_2})r^2 - 3(\mathbf{e_1} \cdot \mathbf{r})(\mathbf{e_2} \cdot \mathbf{r})}{r^5}, \tag{1.3}$$

where C_{dd} is the dipolar coupling constant, which in case of magnetic dipoles[9] is given by $\mu_0\mu_1\mu_2$, with μ_0 the vacuum permeability and r the distance between the dipoles.

Applying an external magnetic field it is possible to polarize the sample in such a way that all dipoles point in the same direction, in this case Eq. (1.3) takes the simple form

$$U_{\text{DDI}}(r) = \frac{\mu_0\mu_1\mu_2}{4\pi} \frac{1 - 3\cos^2\theta}{r^3}, \tag{1.4}$$

where θ is the angle between the direction of the magnetic field and the relative position of the dipoles.

Relation (1.4) shows the anisotropic and the long-range[7] character of the DDI. In particular, tuning the angle θ from 0 (*head-to-tail* configuration) to $\pi/2$ (*side-by-side* configuration), the interaction potential switches from attractive to repulsive. Furthermore, since $1 - 3\cos^2\theta$ goes from -2 to 1, the maximum repulsion is half the maximum attraction and there is a critical angle equal to $\theta_m = 54.7°$ at which the dipole-dipole interaction vanishes. A sketch of the DDI in the not polarized and polarized case is shown in Fig. 1.4a and in Fig. 1.4b, respectively.

Since DDI scales as r^{-3}, the total scattering cross section contains the contributions given by all the partial waves, not only the s-wave[10]. Furthermore, it does not vanish for identical fermions at low temperature.

The magnetic moment's projection along the direction of the magnetic field can be expressed as

$$\mu_i = m_{J_i} g_{J_i} \mu_B \qquad \text{with } i = 1, 2 \tag{1.5}$$

---

[9]This relation can easily be applied to atoms with an electric dipole moment d writing $C_{\text{dd}} = d^2/\varepsilon_0$.

[7]The DDI shows a long-range character in three dimensions, in one and two dimensions is short-range.

[10]$\delta_k \sim k$ for all partial waves, thus for small k the phase shift does not vanish [69].

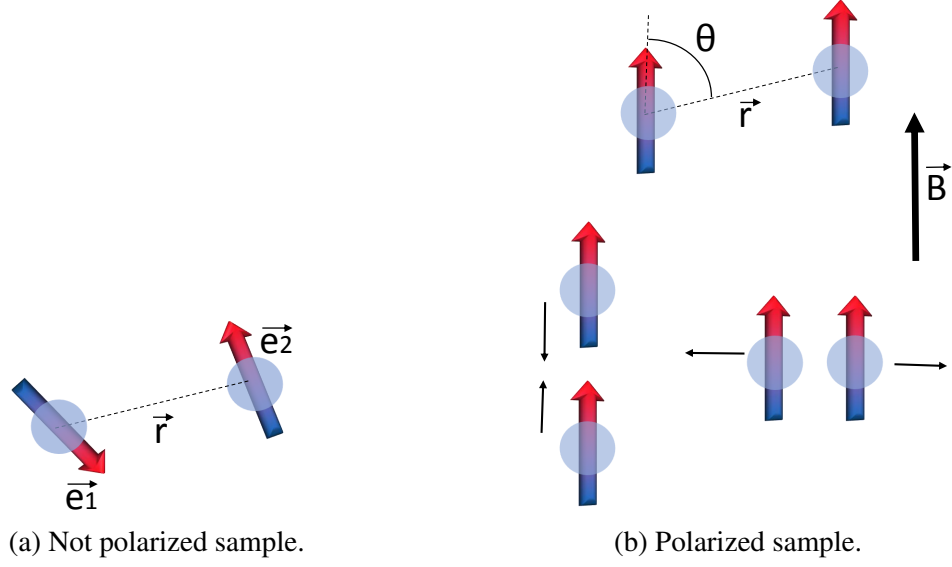(a) Not polarized sample.   (b) Polarized sample.

Figure 1.4 Dipole-dipole interaction between two particles for a not polarized sample (a) and a sample polarized by an external magnetic field (b). The *head-to-tail* configuration shows an attractive interaction while when the dipoles sit *side-by-side* the interaction is repulsive.

where m_J is the projection of the total angular momentum along the direction of the magnetic field and g_J is the Landé g-factor given by

$$g_J = 1 + (g_S - 1)\frac{J(J+1) - L(L+1) + S(S+1)}{2J(J+1)}, \qquad (1.6)$$

with $g_S \approx 2.002$ the gyromagnetic ratio of the electron spin. In the lowest energy level Er occupies the state $|J, m_J\rangle = |6, -6\rangle$ while Dy is in the state $|J, m_J\rangle = |8, -8\rangle$, by approximating $g_S = 2$ in Eq. (1.6), the magnetic moments read:

$$\mu_{\text{Er}} = 6.98\,\mu_{\text{B}}, \qquad \mu_{\text{Dy}} = 9.93\,\mu_{\text{B}}. \qquad (1.7)$$

Our experiment, called from now on "RARE", combines for the first time two dipolar species, thus for an Er and Dy mixture one has to consider the dipole-dipole intra-species interactions:

$$U_{\text{DDI}}^{\text{intra}}(r) = \frac{\mu_0 \mu_{\text{Er}} \mu_{\text{Er}}}{4\pi}\frac{1 - 3\cos^2\theta}{r^3}, \qquad U_{\text{DDI}}^{\text{intra}}(r) = \frac{\mu_0 \mu_{\text{Dy}} \mu_{\text{Dy}}}{4\pi}\frac{1 - 3\cos^2\theta}{r^3} \qquad (1.8)$$

and the inter-species interactions:

$$U_{\text{DDI}}^{\text{inter}}(r) = \frac{\mu_0 \mu_{\text{Er}} \mu_{\text{Dy}}}{4\pi}\frac{1 - 3\cos^2\theta}{r^3}. \qquad (1.9)$$

Table 1.4 Comparison of dipole moments and relative dipolar strengths between different atoms and heteronuclear molecules. The relative dipolar strength can be tuned changing the s-wave scattering length through Feshbach resonance [51].

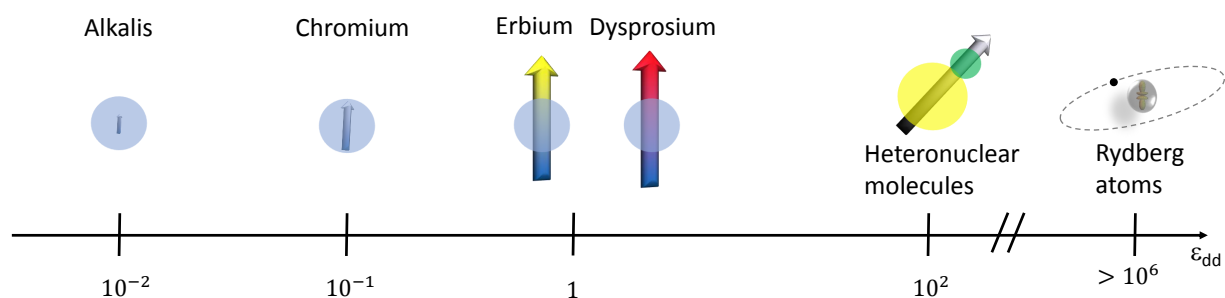| Element	Dipole moment	ε_{dd}
Rb	$1\,\mu_B$	0.007
Cr	$6\,\mu_B$	0.16
Dy	$10\,\mu_B$	$0.1-1$
Er	$7\,\mu_B$	$0.1-1$
KRb	$1.5\,D$	20
HCN	$3.0\,D$	240

Figure 1.5 Sketch of the relative dipolar strengths for different species. The hard sphere represents the contact interaction. In the alkalis the dipolar contribution is almost negligible while it becomes relevant with dipolar atoms like Er and Dy.

To quantify the absolute strength of the dipolar interactions usually the dipolar length is defined:

$$a_{dd} \equiv \frac{C_{dd}m}{12\pi\hbar^2}. \tag{1.10}$$

DDI is also often expressed relatively to the strength of the contact interactions, given by the scattering length a, by the quantity

$$\varepsilon_{dd} \equiv \frac{a_{dd}}{a} = \frac{C_{dd}m}{12\pi\hbar^2 a}. \tag{1.11}$$

Figure 1.5 shows the relative dipolar strengths of different species. In particular, the values of the dipole moment and ε_{dd} for different atoms (Rb, Cr, Er and Dy) are compared with the huge values of the heteronuclear molecules in Table 1.4. Tuning the contact interactions through Feshbach resonances [19, 49] allows the system to get into the strongly dipolar

regime in which $\varepsilon_{dd} > 1$. In this regime new exotic many-body phases are raising particular interest [20, 21, 28].

Chapter 2

Optical dipole trap: theory and simulations

One of the crucial steps to create a quantum-degenerate gas, such as a Bose-Einstein condensate for bosons or a degenerate Fermi gas for fermions, is to use evaporative cooling to get phase-space density that could not be reached in a magneto optical trap.

The first Bose-Einstein condensate was obtained in 1995, at JILA [5], with laser precooled, magnetically trapped atoms of ^{87}Rb using RF evaporative cooling. Afterwards, several groups tried to switch to optical schemes. Compared to magnetic traps, that can only confine atoms in "low-field seeking states[1]", optical traps can trap all Zeeman sublevels. Furthermore, they allow the use of Feshbach resonances to tune the interaction strength without changing the parameters of the trapping potential. Only in 2001, in the group of Chapman [10], a Bose-Einstein condensate of ^{87}Rb was achieved by evaporative cooling in a crossed optical dipole trap generated by a CO_2 laser ($\lambda = 10.6\,\mu m$).

In this chapter the basic principles of optical trapping will be introduced to understand and characterize the optical dipole trap implemented in the Er-Dy-experiment. Special attention will be devoted to the important role of the polarizability in trapping efficiency. Finally, the last section will be dedicated to the simulations of the trapping potential implemented for the two species.

2.1   Optical trapping: basic concepts

When an atom is exposed to an electric field, the displacement of the electrons with respect to the nucleus will induce an atomic dipole moment given by $\vec{p} = \sum_i -e\vec{r}_i$, where $\vec{r}_i$ is the

---

[1]From Wing's theorem only local minima of the magnetic field modulus can be achieved in free space.

position vector of the i-th electron. For laser light of a certain frequency ω, the induced dipole moment oscillates at the driving frequency and his amplitude is related to the electric field amplitude by the following relation [35],

$$p(r) = \alpha(\omega)E(r), \tag{2.1}$$

where $\alpha(\omega)$ is the complex dynamical polarizability which determines the interaction energy of the induced dipole moment with the driving field.

The real part of α, which corresponds to the in-phase dipole oscillation, is important for calculating the dipole potential:

$$U_{\text{dip}}(r) = -\frac{1}{2}\langle \vec{p}\cdot\vec{E}\rangle = -\frac{1}{2\varepsilon_0 c}\text{Re}\{\alpha\}I(r), \tag{2.2}$$

where $\langle\cdot\rangle$ denotes the time average, ε_0 is the vacuum permittivity, c is the speed of light and $I = 2\varepsilon_0 c|E|^2$ is the intensity of the electric field.

Atoms can also absorb energy and re-emit it, this can be seen as a scattering process with rate Γ_{sc}, which represents the out-of-phase oscillation and it is given by the imaginary part of the polarizability,

$$\Gamma_{\text{sc}}(r) = \frac{P_{\text{abs}}}{\hbar\omega} = \frac{1}{\hbar\varepsilon_0 c}\text{Im}\{\alpha\}I(r), \tag{2.3}$$

where $P_{\text{abs}} = \langle\vec{p}\cdot\vec{E}\rangle$ is the power absorbed by the atom.

To get an expression for the polarizability, it is possible to start considering the atom as a classical oscillator like in the Lorentz's model, where an electron is elastically bound to the nucleus with an eigenfrequency equivalent to the frequency of the optical transition ω_0. Denoting Γ as the damping rate corresponding to radiative energy loss, m_e as the electron's mass and integrating the equation of motion $\ddot{x} + \Gamma\dot{x} + \omega_o^2 x = -eE(t)/m_e$, the polarizability takes the form:

$$\alpha(\omega) = 6\pi\varepsilon_0 c^3 \frac{\Gamma/\omega_o^2}{\omega_o^2 - \omega^2 - i(\omega^3/\omega_o^3)\Gamma}. \tag{2.4}$$

The dynamical polarizability can be replaced by the scalar polarizability α if the condition $\omega \ll \omega_0$ is fulfilled. In the semiclassical approach, for a two-level quantum system, Γ corresponds to the spontaneous decay rate for an allowed transition in the dipole approximation from the excited state $|e\rangle$ to the ground state $|g\rangle$ and it is proportional to the dipole matrix element

$$\Gamma = \frac{\omega_0^3}{3\pi\varepsilon_0\hbar c^3}|\langle e|\mu|g\rangle|^2, \tag{2.5}$$

where $\hat{\mu} = \vec{p} \cdot \hat{e}$ is the electric dipole moment operator and $\hat{e}$ is the direction of the electric field.

In the case of optical dipole traps, which use light far-detuned from the optical transition ω_0, since the saturation can be really small and the population of the excited state is basically negligible, the condition $\Gamma_{sc} \ll \Gamma$ is fulfilled and the classical model yields the same results given by the semiclassical approach. This leads to the following expressions for the dipole potential and the scattering rate:

$$U_{\text{dip}}(r) = -\frac{3\pi c^2}{2\omega_o^3} \left(\frac{\Gamma}{\omega_0 - \omega} + \frac{\Gamma}{\omega_0 + \omega} \right) I(r), \tag{2.6}$$

$$\Gamma_{\text{sc}}(r) = -\frac{3\pi c^2}{2\hbar\omega_o^3} \left(\frac{\omega}{\omega_0} \right)^3 \left(\frac{\Gamma}{\omega_0 - \omega} + \frac{\Gamma}{\omega_0 + \omega} \right)^2 I(r). \tag{2.7}$$

If the detuning from the resonance $\Delta = \omega - \omega_0$ is not too large ($|\Delta| \ll \omega_0$) , the *rotating-wave approximation* can be applied, by neglecting the term that involves $\omega_0 + \omega$, to get the two simple expressions:

$$U_{\text{dip}}(r) = \frac{3\pi c^2}{2\omega_o^3} \left(\frac{\Gamma}{\Delta} \right) I(r) \simeq \frac{I}{\Delta}, \tag{2.8}$$

$$\Gamma_{\text{sc}}(r) = \frac{3\pi c^2}{2\hbar\omega_o^3} \left(\frac{\Gamma}{\Delta} \right)^2 I(r) \simeq \frac{I}{\Delta^2}. \tag{2.9}$$

Equations (2.8) and (2.9) provide us the first tool to underline two important features of optical dipole traps:

- if the frequency of the laser light is below the frequency of the atomic transition ($\Delta < 0$), the dipole potential assumes negative values and the atoms, trying to minimize the interaction energy, will be attracted towards regions of higher intensity (*red detuned trap*). Whereas, if the detuning is positive ($\Delta > 0$) the atoms will be pushed away from the high intensity regions (*blue detuned trap*).

- by increasing the intensity of the light and the detuning, the same trap depth can be reached with a reduced scattering rate. This shows the advantage of using optical dipole trap at high power and large detunings, since less scattering means less heating of the atomic sample.

Up to now the polarizability has been considered independent on the orientation of the electric field. This would be right in case of alkali or alkali-earth atoms which are characterized by a ground state with zero angular momentum. In the contrary, as described in Chapter 1, dipolar gases like erbium and dysprosium feature an electronic configuration with an incompletely

filled $4f$ shell which leads to a ground state with angular momentum $L \neq 0$. Therefore, the electronic distribution around the core is not spherically symmetric, resulting in an highly anisotropic response to the light.

This anisotropy manifests a tensorial form of the polarizability and the trapping potential accordingly contains also terms dependent on the light's polarization and on the different M_J sublevels. Equation (2.2) has to be modified to

$$U_{M_J}(r, \omega, \theta_p, \theta_k, A) = -\frac{1}{2\varepsilon_0 c} I(r) \left\{ \text{Re}[\alpha_s(\omega)] + A\cos\theta_k \frac{M_J}{2J} \text{Re}[\alpha_v(\omega)] + \right.$$
$$\left. + \frac{3M_J^2 - J(J+1)}{J(2J+1)} \frac{3\cos^2\theta_p - 1}{2} \text{Re}[\alpha_t(\omega)] \right\}, \tag{2.10}$$

where $\alpha_s(\omega)$ contains the diagonal elements of the polarizability tensor, $\alpha_v(\omega)$ is the anti-symmetric part and $\alpha_t(\omega)$ is the symmetric part of the off-diagonal terms. θ_k is defined by the angle between the quantization axis, given by the magnetic field direction, and light's polarization. θ_p is defined by the angle between the quantization axis and wave vector. Finally, A is the ellipticity coefficient of the polarization [53].

The polarization of an optical dipole trap beam is usually linear, in this case the expression above simplifies because $A = 0$. Thus, the term due to the vectorial part plays no role and the dipole potential will depend only on the polarization angle θ_p and on the given state $|J, M_J\rangle$. Up to now both theoretical calculations [53, 54] and experimental results [12] have demonstrated that even though for their electronic configuration erbium and dysprosium should respond to the light in an anisotropic way, the trapping potential created by an infrared laser beam is almost isotropic. On the other hand, this is not the case for the scattering rate which results extremely anisotropic. Indeed, as can be seen from the experiment, the lifetime of the atoms in the dipole trap depends strongly on the light's polarization.

So far, we have reported only about the dipole potential and the scattering rate for a two-level system. However, in reality atoms have several electronic transitions between different energy levels. Furthermore, the spectrum is very rich in the case of Er and Dy. The effect of the electric field on the atom can be seen as a perturbation given, in the dipole approximation, by the term $H^{(1)} = -\hat{\mu} \cdot \vec{E}$. Since atomic states have a definite parity and the perturbation is an odd operator, the first order's contribution to the perturbation vanishes. Thus, the energy shift of the ground state $|g_i\rangle$ is given by the second order term and it is related to the dipole matrix elements of all the excited states $|e_j\rangle$ as below:

$$\Delta E_i = \sum_j \frac{|\langle e_j|\mu|g_i\rangle|^2}{\Delta_{ij}} \frac{I}{2\pi\varepsilon_0 c}, \tag{2.11}$$

where Δ_{ij} is the detuning between $|g_i\rangle$ and $|e_j\rangle$. The dipole matrix elements $|\langle e_i|\mu|g_i\rangle|$ and the scattering rate can be expressed in terms of the transition coefficients (c_{ij}) which take into account the coupling strength between the specific sublevels and can be obtained by the use of 3J-symbol[2]:

$$\mu_{ij} = c_{ij}||\mu||\,, \qquad \tilde{\Gamma}_j = c_{ij}^2\Gamma_j,$$

with $||\mu||$ the reduced matrix element given by relation (2.5). Equations (2.6) and (2.7) can then be generalized as below:

$$U_{\text{dip}}(r) = \left[-\sum_j \frac{3\pi c^2}{2\omega_{ij}^3}\left(\frac{\tilde{\Gamma}_j}{\omega_{ij}-\omega}+\frac{\tilde{\Gamma}_j}{\omega_{ij}+\omega}\right)\right]I(r) = \tilde{U}I(r), \qquad (2.12)$$

$$\Gamma_{\text{sc}}(r) = \left[\sum_j \frac{3\pi c^2}{2\hbar\omega_{ij}^3}\left(\frac{\omega}{\omega_{ij}}\right)^3\left(\frac{\tilde{\Gamma}_j}{\omega_{ij}-\omega}+\frac{\tilde{\Gamma}_j}{\omega_{ij}+\omega}\right)^2\right]I(r), \qquad (2.13)$$

where the quantity in square brackets in Eq. (2.12) represents the polarizability $\tilde{U}$. In Fig. 2.1 the total polarizability, including the scalar and tensorial parts, is plotted as a function of the wavelength. The strongest transition is at 401 nm for Er in contrast to 421 nm for Dy, with the effect that everyline above (below) this wavelength is red (blue) detuned. The stars represent the experimental data listed in Table 2.1.

Table 2.1 List of experimental values of the polarizability expressed in atomic units and measured by other groups [12, 58, 60]. The huge systematic uncertainties derive from the measurement of the beam waist, as explained in section 2.3.

Erbium		Dysprosium	
Wavelength (nm)	Re$\{\alpha\}$ a.u.	Wavelength (nm)	Re$\{\alpha\}$ a.u.
532	$430 \pm 8_{\text{st}} \pm 80_{\text{sys}}$ [12]		
1064	$166 \pm 3_{\text{st}} \pm 61_{\text{sys}}$ [12]	1064	136 ± 15 [60], 116 [58]
1570	$163 \pm 9_{\text{st}} \pm 36_{\text{sys}}$ [12]		

2.2 Optical trap with Gaussian beams

Optical trapping of neutral atoms relies on two types of radiative forces:

---

[2]The Wigner 3J-symbols are related to the Clebsch-Gordan coefficients, which quantify the wavefunction overlap.
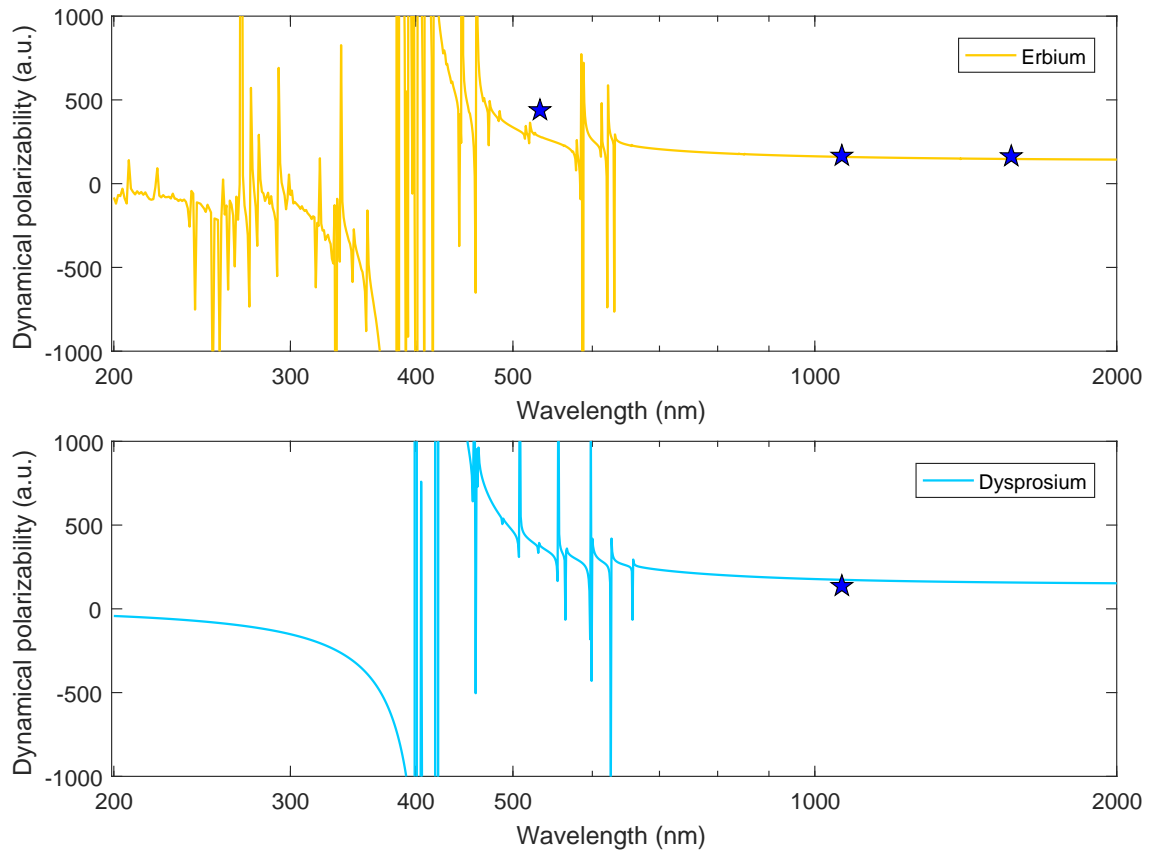
Figure 2.1 Dynamic polarizability as a function of the wavelength for Er (top) and Dy (bottom). In this simulation the contribution of the tensorial part has been taken into account [12].

- the *scattering force* due to the absorption of the radiation followed by the spontaneous emission, which is classified as a scattering process with the rate Γ_{sc},

- the *dipole force* resulting from the spatial gradient of the dipole potential U_{dip} and thus the gradient of the light's intensity.

With lasers it is possible to achieve high intensity and high spatial intensity gradient that allow to modify the motion of the atoms and stably trap them. Thus, the simplest form of an optical dipole trap is the focus of a red-detuned Gaussian laser beam.

2.2.1   Single beam

Let's consider an elliptic Gaussian beam[3] propagating along the y direction, with z direction coincident with the axis of gravity, with beam waist $w_{x,z}$ and power P. The intensity profile of an elliptic beam for a fixed power can be expressed by the following relation:

$$I(x,y,z) = \frac{2P}{\pi w_x(y)w_z(y)} \exp\left[-2\left(\frac{x^2}{w_x^2(y)} + \frac{z^2}{w_z^2(y)}\right)\right].$$
(2.14)

The beam radius, in terms of the beam waist $w_{x,z}$ and the Rayleigh length $z_{R_{x,z}}$, can be written as

$$w_{x,z}(y) = w_{x,z}\sqrt{1+\left(\frac{y}{z_{R_{x,z}}}\right)^2} \qquad \text{with} \quad z_{R_{x,z}} = \frac{\pi w_{x,z}^2}{\lambda}.$$
(2.15)

For a given laser power P, the intensity reaches its maximum in $(x,y,z) = (0,0,0)$ where it assumes the expression

$$I_0 \equiv I(0,0,0) = \frac{2P}{\pi w_x w_z}.$$
(2.16)

One of the important parameters to be defined for an optical dipole trap is the total trap depth $\hat{U}$, which is given by Eq. (2.12) replacing $I(r)$ with I_0:

$$\hat{U} = \tilde{U}I_0 = \tilde{U}\frac{2P}{\pi w_x w_z}.$$
(2.17)

If the thermal energy $k_B T$ is much less than the trap depth $\hat{U}$, the atomic cloud will occupy mainly the central region of the trap where the dipole potential can be approximated as

$$U_{\text{dip}} \simeq \hat{U}\left[1 - \frac{2x^2}{w_x^2} - \frac{2z^2}{w_z^2} - \frac{1}{2}y^2\left(\frac{1}{z_{R_x}} + \frac{1}{z_{R_z}}\right)^2\right].$$
(2.18)

---

[3]The choice of an elliptic Gaussian beam is made because the shape of the beam is modified during the experimental cycle as it will be described deeply in Chapter 3.

Equation (2.18) can be rewritten as an harmonic potential. The trapping frequencies can then be obtained writing the harmonic dipole potential in terms of the oscillation frequencies:

$$U_{\text{dip}} \simeq \hat{U} \left[1 - \frac{2x^2}{w_x^2} - \frac{2z^2}{w_z^2} - \frac{1}{2}y^2 \left(\frac{1}{z_{R_x}} + \frac{1}{z_{R_z}} \right)^2 \right] \simeq$$
$$\simeq \hat{U} \left[1 - \frac{1}{2}m\omega_x^2 x^2 - \frac{1}{2}m\omega_y^2 y^2 - \frac{1}{2}m\omega_z^2 z^2 \right] \tag{2.19}$$

$$\omega_{x,z} = \sqrt{\frac{4\hat{U}}{mw_{x,z}^2}}, \quad \omega_y = \sqrt{\frac{2\hat{U}}{mz_{R_h}^2}}, \tag{2.20}$$

where z_{R_h} is the effective Rayleigh length for the elliptic beam defined as:

$$\frac{1}{z_{R_h}^2} = \left(\frac{1}{z_{R_x^h}} + \frac{1}{z_{R_z^h}} \right)^2. \tag{2.21}$$

As we can see from Eq. (2.17) and (2.20), the choice of the beam waist is highly critical. The trap depth and the trapping frequencies, which are the most important parameters to control during the forced evaporative cooling, rely exactly on the dimension of the waist.
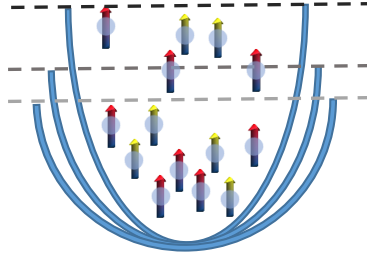
The basic idea of the forced evaporative cooling is to allow the hotter atoms to escape lowering the trap depth while the colder atoms remain trapped and rethermalize. In optical dipole traps this is usually done reducing the power of the laser beam. The desired condition would be to reduce the depth keeping the curvature of the trap, i. e. the trapping frequencies, constant but, as it is written in the equations above, together with the trap depth which scales as P also the trapping frequencies scale down as $\sqrt{P}$. This situation is depicted in the simple cartoon representing the evaporative cooling in Fig. 2.2. Since evaporative cooling depends on the elastic collisions rate which decreases with decreasing frequencies, the cooling process can be stuck. This is the reason why trap depth, trapping frequencies and evaporation's time steps have to be chosen carefully to get an efficient evaporative cooling. Indeed if the evaporation rate is too low, atoms can be lost due to collisions with background gas or photon scattering processes. In contrary if the evaporation rate is too high, with almost constant trapping frequencies, three-body losses can become important.

2.2.2 Crossed beams

From relations (2.20) it comes out that a single focused beam creates an anisotropic trap with a longitudinal confinement that is weak compared to the radial one. Instead, crossing two
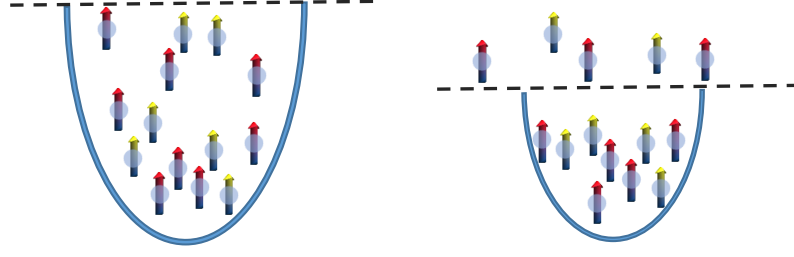
(a) Ideal case.

(b) Real case.

Figure 2.2 Sketch representing the basic idea of evaporative cooling. (a) Ideal case in which the trap depth is lowered without influencing the trapping frequencies. What happens in reality during evaporative cooling in an optical dipole trap is depicted in (b). Lowering the power of the laser not only reduces the trap depth but also the trapping frequencies.

focused laser beams, it is possible to create a trapping potential with a tight confinement along all the three directions.

As a second beam let's consider another elliptic Gaussian beam propagating along the direction of the gravity and crossing the first beam at an angle of 90°. The resulting trapping potential is just given by the sum of the two dipole potentials:

$$
U_{\text{cross}} \simeq \hat{U}_h \left[1 - \frac{2x^2}{w_x^2} - \frac{2z^2}{w_z^2} - \frac{1}{2} y^2 \left(\frac{1}{z_{R_x}} + \frac{1}{z_{R_z}} \right)^2 \right] +
$$
$$
+ \hat{U}_v \left[1 - \frac{2x^2}{w_x^2} - \frac{2y^2}{w_y^2} - \frac{1}{2} z^2 \left(\frac{1}{z_{R_x}} + \frac{1}{z_{R_y}} \right)^2 \right],
$$

(2.22)

where $\hat{U}_h$ and $\hat{U}_v$ are the total trap depth of the beam propagating along y and z direction, respectively. In the following pages the first will be referred as *horizontal beam* while the second one *vertical beam*. Applying the harmonic approximation and defining the effective

Rayleigh length also for the vertical beam:

$$\frac{1}{z_{R_v}^2} = \left(\frac{1}{z_{R_x^v}} + \frac{1}{z_{R_y^v}} \right)^2, \qquad (2.23)$$

the trapping frequencies can be expressed as below:

$$
\begin{aligned}
\omega_x &= \sqrt{\frac{4}{m} \left(\frac{\hat{U}_h}{w_{hx}^2} + \frac{\hat{U}_v}{w_{vx}^2} \right)}, \\
\omega_y &= \sqrt{\frac{1}{m} \left(\frac{4\hat{U}_v}{w_{vy}^2} + \frac{2\hat{U}_h}{z_{Rh}^2} \right)}, \\
\omega_z &= \sqrt{\frac{1}{m} \left(\frac{4\hat{U}_h}{w_{vz}^2} + \frac{2\hat{U}_v}{z_{Rv}^2} \right)}.
\end{aligned}
\qquad (2.24)
$$

The Rayleigh lengths are much smaller than the waist thus, from relations (2.24), it is clear that each beam contributes to the trap frequency orthogonal to the direction of propagation, while the trap frequency along the direction of propagation is mostly given by the other beam.

2.2.3 Gravity and astigmatism

When dealing with real life, the parameters of the trap, like the depth and the frequencies, may be influenced due to several reasons. The most obvious one is the presence of the gravity which adds to the trapping potential the quantity $U_g = mgz$. Thus, along the z direction, the trapping potential is tilted, the trap depth is reduced and the atoms can be lost. This effect is mainly visible in shallow trap rather than in the tight ones. Below a certain minimum power the trap is not able anymore to hold the atoms. Considering the conservative force arising from the dipole potential $F_{\mathrm{dip}}(r) = -\frac{d}{dr} U_{\mathrm{dip}}(r)$ it is possible to get the minimum power necessary to beat the gravity, equating the dipole force to the force due to gravity, which for our trap parameters[4] are $P \simeq 70\,\mathrm{mW}$ and $P \simeq 60\,\mathrm{mW}$ for Er and Dy, respectively.

In this case again the polarizability is crucial, the lanthanides are characterized by quite small values of the polarizability with respect to other species. For example in comparison with Cs or Rb is more than a factor of three lower[5]. This means that, for a fixed waist, more power is needed to trap the atoms. The effect of gravity is taken into account substituting the trap depths, in the expression (2.24) relative to the z direction, with the reduced ones.

---

[4] $w_{x,z} = 20.5\,\mu\mathrm{m}$, $\mathrm{Re}^{\mathrm{Dy}}\{\alpha\} = 136\,\mathrm{a.u.}$ and $\mathrm{Re}^{\mathrm{Er}}\{\alpha\} = 166\,\mathrm{a.u.}$
[5] $\mathrm{Re}\{\alpha\}^{\mathrm{Cs}} = 1153\,\mathrm{a.u.}$, $\mathrm{Re}\{\alpha\}^{\mathrm{Rb}} = 677\,\mathrm{a.u.}$

Another source of reduction of the trap depth is the astigmatism. A finite astigmatism has to be taken into account, indeed the position of the foci along the two different axes may not coincide

$$\Delta y = y_{\text{focus,x}} - y_{\text{focus,z}} \neq 0.$$

When the astigmatism is on the same size or larger than the Rayleigh lengths, the relation (2.15) has to be modified considering that the waists along the different axes reach the minimum in two different points along the y-direction:

$$w_x(y) = w_x \sqrt{1 + \left(\frac{y}{z_{R_x^h}}\right)^2} \qquad w_z(y) = w_z \sqrt{1 + \left(\frac{y - \Delta y}{z_{R_z^h}}\right)^2} \tag{2.25}$$

The astigmatism modifies the dipole potential with the presence of two minima, inducing a reduction of the effective trap depth and trapping frequencies.

2.3   A trap for Er and Dy

To simulate the trap implemented in the Er-Dy experiment, let's first consider a single laser beam propagating along the *y* direction with a wavelength of 1064 nm, a power of 30 W and radial waists equal to $w_{x,z} = 20.5 \, \mu$m. The trapping potential for the two species are calculated taking as values for the polarizability the experimental values measured in other groups, $\text{Re}\{\alpha\} = 136$ a.u. [60] and $\text{Re}\{\alpha\} = 166$ a.u. [12] for Dy and Er, respectively. The parameters chosen to reproduce the trapping potential are listed in Table 2.2.

Table 2.2 Parameters of the horizontal and vertical beam chosen to simulate the optical dipole trap implemented in the Er-Dy experiment. The values of the polarizability have been experimentally measured by other groups.

	Power (W)	Beam waist (μm)		Polarizability (a.u.)	
		w_x	w_z	Er	Dy
Horizontal beam	30	20.5	20.5		
		w_x	w_y	166	136
Vertical beam	8	103.5	95.0		

The polarizabilities' values play a fundamental role in the trapping efficiency and, although the measurements of the polarizability may seem straightforward, the latter still do have a huge uncertainty. This is due to the strong dependence on the waist, indeed, from

Eq. (2.17) and (2.20), writing the polarizability in atomic units[6], one gets:

$$\text{Re}\{\alpha\} = \frac{\omega_{x,z}^2 \pi \varepsilon_0 c m}{4P \times 1.6488 \times 10^{-41}} w_x^3 w_z \propto w^4 .$$

(2.26)

Thus, even a small error in the waist leads to a large error on the polarizability.

Furthermore, also from a theoretical point of view estimate the value of the polarizability is quite tricky. In fact unlike alkali atoms, which have a simple electronic structure with an isotropic s-shell and a not crowded energy spectrum, the lanthanides are characterized by a complex electronic structure and the knowledge of their spectroscopy is still not complete. On the left side of Fig. 2.3 the trapping potential for dysprosium atoms is sketched considering different values of the polarizabilities and on the right side is shown the trapping potential resulting from the experimental values of the polarizability for Er and Dy[7].
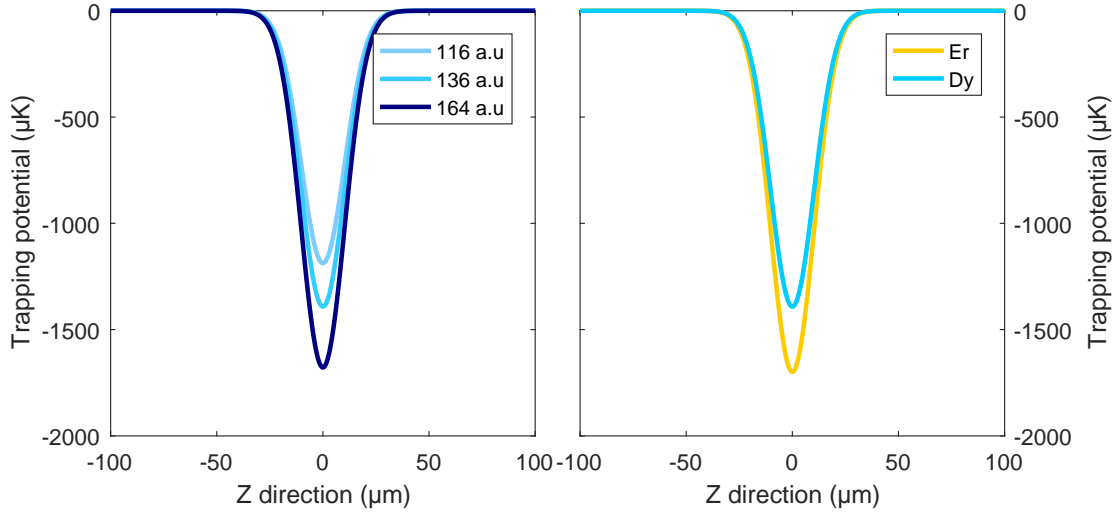

Figure 2.3 Trapping potential for Er and Dy given by a single elliptic Gaussian beam propagating along the *y* direction. The curve on the left side of the figure represents the trapping potential for dysprosium atoms choosing as values for the polarizability the two experimentally measured values 116a.u. [58] and 136a.u. [60] and the theoretical value 164a.u. [54]. On the right side, instead, the trapping potential for Er and Dy is shown choosing the measured values of the polarizability166a.u. and 136a.u..

As mentioned before, the trapping frequencies are crucial for further evaporative steps to reach the degenerate regime. Table 2.3 shows the values of the trap depths and trapping frequencies. These values point out the weak confinement of the trap along the propagation axis, which means that the atoms may spread along that direction even more during the

---

[6]$\tilde{U} = \frac{1}{2\varepsilon_0 c} \text{Re}\{\alpha\} \times 1.6488 \times 10^{-41}$.

[7]In ultracold groups, the trapping potential is usually in units of k_B and expressed in Kelvin.

Table 2.3 Trap depth and trapping frequencies of the horizontal beam. The frequency along the *y* direction, i. e. the direction of propagation, shows a weak confinement with respect to the radial directions.

	Trap depth (µK)	v_x (Hz)	v_y (Hz)	v_z (Hz)
Erbium	1698	4502	53	4502
Dysprosium	1391	4124	48	4124

forced evaporative cooling when the trapping frequencies are reduced due to the decreasing of the power. Therefore, another laser beam may be needed to keep a strong longitudinal confinement and "close the doors" to the atoms during the evaporation and reach the critical phase-space density for the quantum degeneracy.
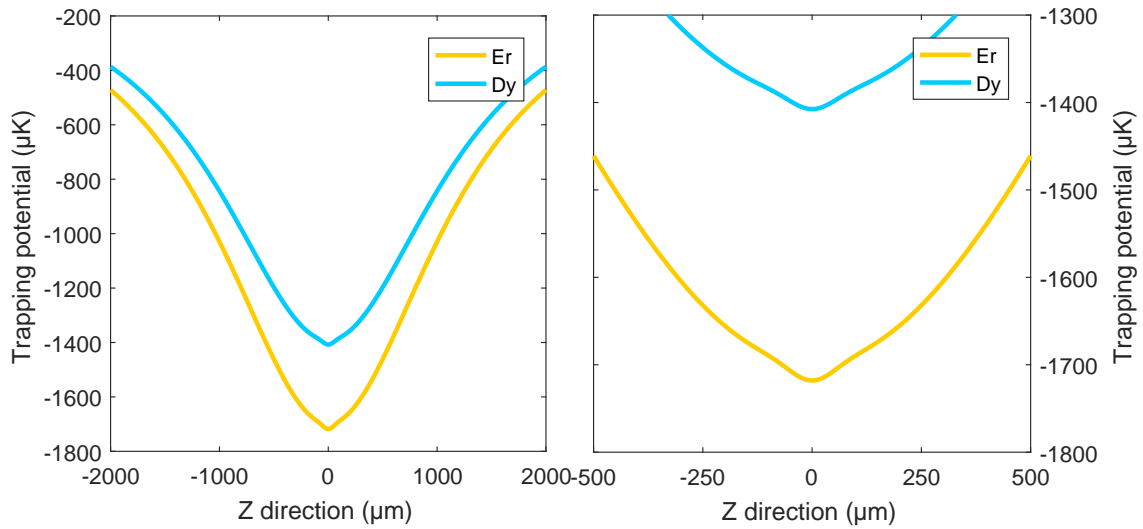

Figure 2.4 Trapping potential for Er and Dy given by the two crossed elliptic Gaussian beams. The vertical beam adds another dipole potential which is represented by the small dip at the origin of the *x*-axis and it is enlarged in the picture on the right.

A second elliptic Gaussian beam, operating at the same wavelength and propagating along the *z* direction, crosses the horizontal beam at an angle of 90°. Considering a power of 8 W, the same polarizabilities as before and the waists $w_x = 101.3\,\mu m$ and $w_y = 95.0\,\mu m$, the resulting trapping potential of the crossed optical dipole trap is depicted in Fig. 2.4 while in Table 2.4 the values for the horizontal ($\hat{U}_h$) and vertical ($\hat{U}_v$) trap depths and the trapping frequencies are listed. The contribution of the vertical beam to the total dipole potential results in a small dip in the central region. Its depth is just around 20 µK deep, this means that as long as the atoms have a much higher thermal energy, they will not see the effect of

Table 2.4 Trap depth of the horizontal and vertical beam and trapping frequencies of the potential resultant from crossing the two beams.

	$\hat{U}_h$ (μK)	$\hat{U}_v$ (μK)	ν_x (Hz)	ν_y (Hz)	ν_z (Hz)
Erbium	1698	20	4503	117	4502
Dysprosium	1391	16	4125	107	4124

the vertical beam. Thus, the second beam becomes useful only when a first stage of plain evaporation and then forced evaporation cooling is applied.

The RARE experiment is the first mixture experiment with two highly magnetic atoms. One of the interesting features of this mixture, in comparison to other mixtures studied up to now in the ultracold groups, is the small mass imbalance and the quite similar values of the polarizability for wavelengths in the infrared region. Erbium and dysprosium offer a wide choice of isotopes and both present isotopes with a mass of 162 u and 164 u. Thus, it would be also possible to have a mixture of two species with the same mass. Table 2.5 shows a list of several mixtures that have been involved up to now in ultracold groups.

Table 2.5 List of mixtures adopted by ultracold groups. Almost all the mixtures are characterized by large mass imbalances except for RbSr and ErDy.

Mixtures	
^{87}Rb^{133}Cs [71], ^{6}Li^{41}K [55], ^{23}Na^{6}Li [40]	Alkali + Alkali
^{87}Rb^{84}Sr [68]	Alkali + Alkali earth metal
^{87}Rb^{171}Yb [83], ^{133}Cs^{174}Yb [44]	Alkali + Rare earth metal
^{168}Er^{162}Dy	Rare earth metal + Rare earth metal

The mass plays an important role in the efficiency of trapping both species. Indeed, strong mass imbalances result in a discrepancy between the confinement seen by atoms of different species. Combining Eq. (2.17) and (2.20), the trap frequencies can be expressed in such a way to underline the mass and the polarizability dependence:

$$\omega_{x,z} = \sqrt{\frac{4}{mw_{x,z}^2} \frac{\tilde{U}2P}{\pi w_x w_z}}, \tag{2.27}$$

from which, considering two species 1 and 2 and calling $\tilde{U}_{1,2}$ and $m_{1,2}$ the polarizability and the mass of each specie, the trap frequencies ratio is given by

$$\frac{\omega_{x,z}^1}{\omega_{x,z}^2} = \sqrt{\frac{m_2 \tilde{U}_1}{m_1 \tilde{U}_2}} . \qquad (2.28)$$

This feature can be used as a tool to reduce the discrepancy of the polarizability, changing among the available isotopes the ones with the right mass ratio. Looking at Table 2.5 it is possible to see that almost all the mixtures are characterized by large mass imbalances except for RbSr and ErDy. In particular, by choosing the fermionic isotope ^{87}Sr, a Bose-Fermi mixture with atoms with the same mass can be realized. However, rubidium and strontium present a larger difference in polarizability values with respect to Er-Dy.

As said in the previous paragraph, the trapping potential is tilted by the gravity. Figure 2.5 displays the trapping potential modified by the gravity for a tight trap with a power of 30 W and a very shallow trap with a power of 0.1 W. In both cases the waists are the same as in the previous simulations. From these pictures it is visible that the effect of the gravity is almost negligible for strong trap as also shown by the values of trap depth and trapping frequencies including gravity, in Table 2.6. Gravity covers an important role in the evaporation process. Indeed, when the power of the laser beam is reduced it becomes more and more important its contribution on the reduction of the trap depth. The crucial point is that gravity reduces the deepness of the trap without influencing the trapping frequencies in the central region.
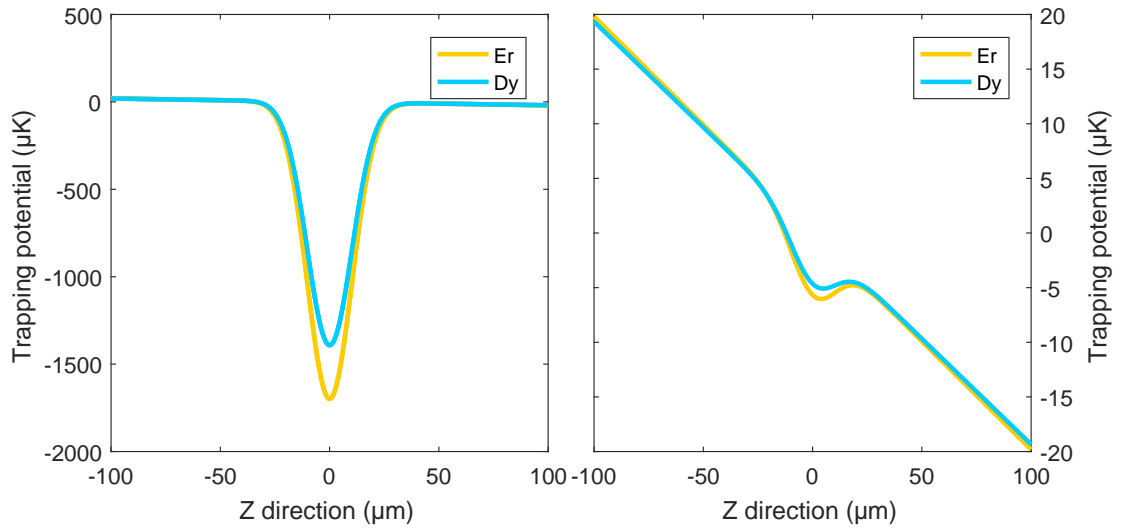

Figure 2.5 Trapping potential for Er and Dy given by the horizontal beam and modified by the gravity. On the left side, the laser beam has a power of 30 W and the effect of the gravity is hardly visible. Instead on the right side, where the power is 0.1 W, the reduction of the trap depth is clear.

Table 2.6 Trap depth of the horizontal and vertical beam and trapping frequencies of cODT modified by the gravity.

	$\hat{U}_h$ (μK)	$\hat{U}_v$ (μK)	ν_x (Hz)	ν_y (Hz)	ν_z (Hz)
Erbium	1690	0	4503	117	4491
Dysprosium	1383	0	4125	107	4112

Finally, the trapping potential may be modified by the astigmatism, whose effect has to be considered if the difference between the foci is on the same order of the Rayleigh length. The Rayleigh lengths of the horizontal and vertical beam are shown in Table 2.7. Furthermore,
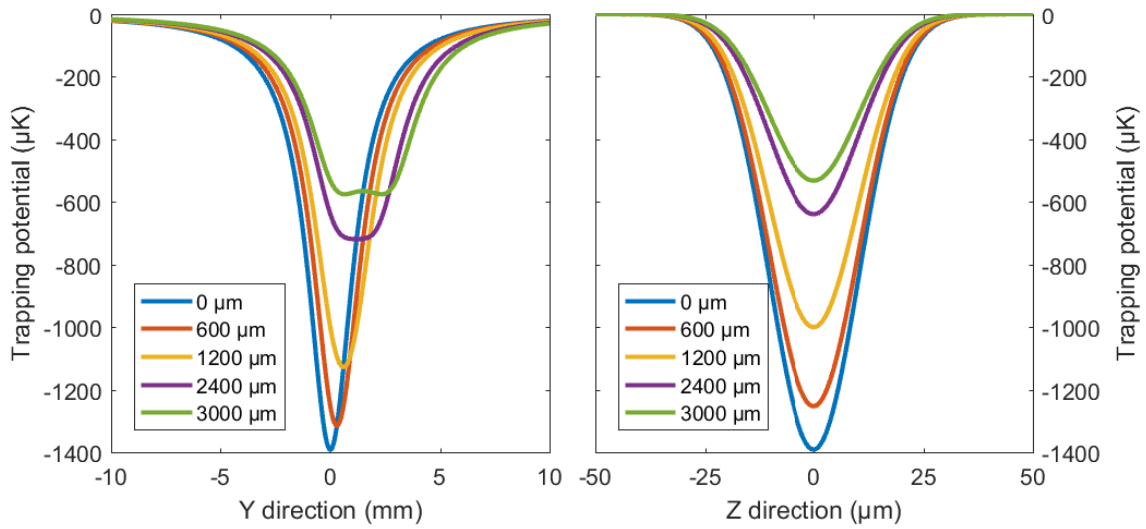

Figure 2.6 Trapping potential for dysprosium atoms along *y* and *z* directions for different values of the astigmatism. The reduction of the trap depth increases when the distance of the two foci raises. Furthermore, when it becomes larger than the Rayleigh length, two minima start to appear along the *y* direction.

for an high astigmatic beam this has to be corrected. As it is shown in Fig. 2.6 for dysprosium, along the *z* direction the depth of the trapping potential is more and more reduced for an increasing astigmatism, whereas along the *y* direction it also assumes a two-well shape. The trap depth for different values of astigmatism is listed in Table 2.8.

Table 2.7 Rayleigh lengths of the horizontal and vertical beams.

Rayleigh length	
Horizontal (z_{R_h}) (mm)	Vertical (z_{R_v}) (mm)
1.2	28.3

Table 2.8 Trap depth for dysprosium atoms calculated for different values of astigmatism. The deepness of the trap is strongly reduced when the astigmatism is on the same order of the Rayleigh length.

Dysprosium	
Astigmatism (Δy) (mm)	Trap depth ($\hat{U}_h$) (μK)
0	1391
0.6	1253
1.2	1000
2.4	639
3.0	532

Chapter 3

Optical dipole trap: experimental realization

Optical dipole traps are a fundamental tool to produce and manipulate ultracold atoms. The interest in building systems to actively control the parameters and the shape of the trap grew enormously. This, indeed, allows to increase the available number of degrees of freedom to manipulate atoms. The first section of this chapter points out the motivations that drive the choice of an optical dipole trap with tunable geometry. The second section introduces the different methods that can be implemented to get a tunable trap and the final section treats the experimental setup necessary to realize a time-averaged potential with an acousto-optic device.

3.1   Why an optical dipole trap with tunable geometry?

The optical dipole trap implemented in the RARE experiment presents a tunable geometry. Indeed, both the shape and the beam size can be changed dynamically during the experimental cycle. This section points out why a tunable dipole trap is so crucial for the experiment. A variable beam waist plays an essential role during the loading of the atoms into the dipole trap, providing a nice "mode matching" between the MOT volume and the ODT volume. Furthermore, the evaporation cooling strongly depends on the particles density, which can be modified changing the trap's volume. Finally, a lot of interesting phenomena arise from the geometry dependence of the dipole-dipole interaction.

3.1.1 Loading efficiency

Let's assume that the atoms in the magneto-optical trap (MOT) follow the Maxwell-Boltzmann energy distribution. When the optical dipole trap is switched on, considering that the atoms in the trap reach the thermal equilibrium with the MOT atoms, which represent the reservoir, the population of the ODT will be given by [1]:

$$N_{\text{ODT}} = \int n f(\text{r},\text{p}) g(\varepsilon) d\text{r} d\text{p}, \tag{3.1}$$

where n is the MOT's particle density, $f(\text{r},\text{p})$ is the distribution function dependent on the position and momentum vector (r,p) and finally, $g(\varepsilon)$ is the ratio of the density of states for the potential created by the ODT to the density of states of the MOT potential, with energy ε. This critical parameter varies from 0 to 1. The first case, $g(\varepsilon) = 0$, is for a δ-like potential, while $g(\varepsilon) = 1$, is for a very shallow trap.

To simplify the expression, let's assume $g(\varepsilon)$ to be constant and equal to g_0 over the overlapping volume, relation (3.1) assumes the form:

$$N_{\text{ODT}} = n_0 V_0 \eta_{\text{loading}}, \tag{3.2}$$

where n_0 and V_0 are the MOT peak density and the overlapped volume, respectively, while η_{loading}:

$$\eta_{\text{loading}} = \frac{4g_0}{\sqrt{\pi}} \int_0^q u^2 e^{-u^2} d\text{u}, \tag{3.3}$$

with u and q defined as below:

$$u = \frac{|p|}{\sqrt{K_B T}}, \qquad q = \frac{U_0}{K_B T}.$$

An increase of the laser power makes the trap deeper and the parameter q as well, but η_{loading} will not rise forever, on the contrary, it saturates and the loading efficiency becomes independent on the laser's power. Relation (3.2) points out that the atom number, loaded into the optical dipole trap, increases linearly with the overlapped volume, as long as the trap depth is above the saturation regime. The overlapped volume scales as $w_x w_z z_{R_h} \pi^{3/2}$, thus to make it larger the beam waist has to be increased, leading to a reduction of the trap depth and consequently a less efficient trap for the evaporation cooling stage.

The ideal situation would be the one in which the initial waist of the laser beam is quite large, in order to get a nice overlap between the ODT and the MOT volume and an high

loading efficiency as well. Then, it is reduced in such a way to get a tight trap useful for starting the evaporation process.

3.1.2 Role of the tunability in evaporative cooling

The possibility of tuning the geometry of the trap plays an important role also in the evaporation process. The latter, indeed, relies on the elastic collision rate between the particles and this depends on the density. The goal at the end of the evaporation steps is to get as many atoms as possible in the degenerate phase. Thus, the elastic collision rate has to be much higher than the rate with which the atoms are lost due to three-body collisions or scattering with background gas.

Considering n_0 the particle density at the center of the trap, the elastic collision rate depends linearly on the density and it can be written as [63]:

$$\Gamma_{el} = \frac{n_0 \sigma \bar{v}}{2\sqrt{2}}, \tag{3.4}$$

where $\sigma = 8\pi a^2$ is the total elastic cross section, a is the s-wave scattering length and $\bar{v}$ is the mean thermal velocity. In contrary, the three-body losses rate depends stronger on the particles density:

$$\Gamma_{3B} = \frac{L_{3B} n_0^2}{3\sqrt{3}}, \tag{3.5}$$

where L_{3B} is the three-body losses coefficient and can be determined measuring the atoms number N after a certain time t from the rate equation [17]

$$\frac{dN}{dt} = -L_{3B} \int_V n^3(x,t) d^3x, \tag{3.6}$$

where n is the particles density over the volume V.

Tuning the geometry of the trap, by changing in a dynamical way the beam waist of the laser beam along one axis, allows the density to be changed in order to improve the evaporation efficiency. Therefore, besides the light power, the tunability of the trap geometry represents an additional experimental parameter to fine tune the evaporation steps.

3.1.3 Tool to probe the anisotropy of DDI

In Chapter 1 the anisotropic character of the dipole-dipole interaction was introduced through the Eq. (1.4). Thus, thanks to this feature, it is possible to tune the interactions from attractive to repulsive, by rotating the magnetic field. Furthermore, it depends on the geometry, so for a

given orientation of the magnetic field, atoms can organize in the *head-to-tail* configuration in which the potential is predominantly attractive or in the *side-by-side* configuration in which they tend to repel each other. To induce the atoms in choosing one or the other, the geometry can be tuned by changing the aspect ratio of the laser beam and its power.

Let's consider the trapping potential, taken in the harmonic approximation, as in Eq. (2.19), with oscillation frequencies $(\omega_x, \omega_y, \omega_z)$. If the magnetic field points in the z direction, the aspect ratio of the trap (AR) is defined as

$$\text{AR} = \frac{\omega_z}{\omega_x} = \frac{w_x}{w_z},$$

for AR > 1 the trap will be oblate (*pancake trap*) while for AR < 1 will be prolate (*cigar trap*). In the first case the atoms will sit side by side giving an overall repulsive interaction, while for a cigar shaped trap the potential will be mostly attractive.

Lot of interesting phenomena came out in the last years taking advantage of this feature of the dipole-dipole interaction as the discovery of new exotic phase of matter [20, 21, 47].

3.2   How to get a tunable dipole trap?

Different methods can be used to change dynamically the beam waist, either with active devices like electro-optic (EOD) or acousto-optic (AOD) deflectors, both based on the creation of time-averaged potential, or with mechanical solutions which involve the use of several optical elements. During the course of this thesis different systems had been tested: first, a system consisting of cylindrical lenses and then, a system built with an acousto-optic modulator (AOM) which was afterwards changed with an AOD. The possibility of using the EOD, which is adopted by other groups to create tailored time-averaged potential [86], was rejected from the beginning because this device may be not suited for high power[1].

3.2.1   System with cylindrical lenses

Following the description in the paper [73], a similar system, formed by five cylindrical lenses, was built to test the possibility of tuning the aspect ratio of our optical dipole trap. Among these lenses, three are convex and the other two are concave. The basic idea is to keep the convex lenses fixed and move the other two jointly along a distance of 25 mm. Figure 3.1a shows a simulation with the software *Zemax OpticStudio* of the optical setup, in which a

---

[1]In our setup a 50 W single mode fiber laser, from the company *Azur Light System* (ALS-IR-1064-50W-SF), with a mean beam waist of 500 µm at 180 cm from the laser head, is implemented to create the optical dipole trap.

magnification of the beam, along the vertical direction, can be seen. The lenses are planned to get a system with a tunable magnification from 1 to a maximum value of 6. Table 3.1 shows a list of distances to observe between the lenses to get the predicted magnifications. Starting from the configuration that leads to a magnification of 1, the concave lenses are

(a) Cylindircal telescope.
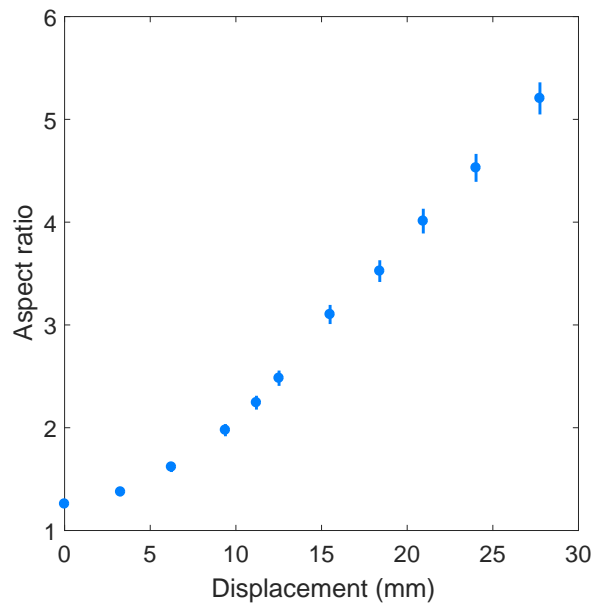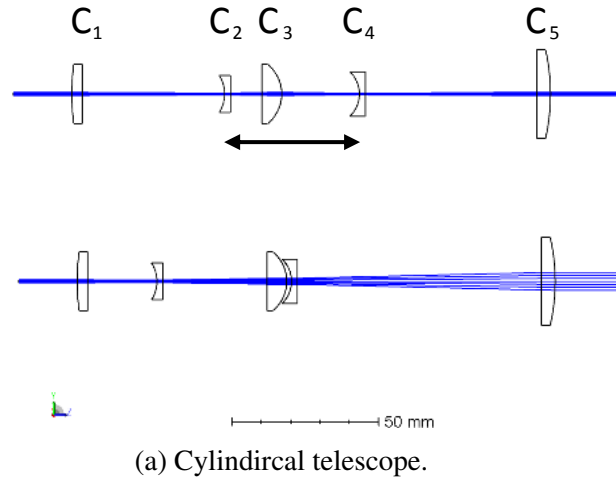
(b) Measured aspect ratio.

Figure 3.1 Sketch of the operation of the cylindrical telescope. (a) Working principle of the cylindrical telescope, simulated with the software *Zemax OpticStudio*, by fixing the lens distances to the values in Table 3.1. In the upper and lower part of the figure, the configuration leading to magnification of 1 and 6 are shown, respectively. (b) Aspect ratio measured by changing the travelling distances of the C2 and C4 lenses.

Table 3.1 List of the distances, between the cylindrical lenses, necessary to reach a magnification of 1 and 6. The concave lenses, C2 and C4, are moved back and forth together, while the convex lenses, C1, C3 and C5, are fixed. These values are taken from [73] and verified with simulations using the software *Zemax OpticStudio*.

	Magnification	
	×1	×6
	Distance	
Lenses	(mm)	(mm)
C1 - C2	48.54	23.63
C2 - C3	10.73	35.64
C3 - C4	26.54	1.63
C4 - C5	58.562	83.47
C2 - C4	37.27	37.27

moved on a motorized linear stage[2] in such a way to get the lens C4 closer to C3. Thus, the beam size along the vertical direction (z) increases with respect to the horizontal one (x). When the laser beam reaches the last lens, used to focus the light on the atoms in the chamber, the vertical dimension, which is now larger, will be focused more, resulting in a smaller beam waist along the z direction. Figure 3.1b shows the AR reached moving the two concave lenses on the linear stage. On the x-axis the distance travelled by the two concave lenses is plotted starting from the position correspondent to the theoretical unitary magnification. The initial position leads to an AR of 1.26 ± 0.04, due to the fact that the laser beam is slightly elliptical. The maximum achievable AR is 5.3 ± 0.2, which do not follow the predicted value, probably due to technical problems involving the test mount, which did not allow to get the lens C4 exactly in the desired position. It is worth to underline that this method is completely different from the one involving time-averaged potential. Indeed, the lenses change the real beam waist and it is not an effect related to a fast modulation. As a consequence, the beam behaves as a Gaussian beam also along the y direction. The big issue of this technique is the implication of the motion of mechanical parts. Furthermore, it requires a linear stage with a maximum travelling velocity compatible with the time scale of experimental cycle ($\sim 10\,\mu$s).

3.2.2 Time-averaged potential

In the last years, time-averaged potentials have been used to investigate the physics of ultracold atoms in optical dipole traps with particular geometry, like ring traps [13], box-shaped trap [33] or traps with several numbers of wells [81]. Indeed, the trap can be shaped

---

[2]Thorlabs KMTS50E/M.

in different ways making use of the principle of the time-averaged potential, in which the beam is sweeped in one or two dimensions at a frequency much higher than the oscillation frequency of the atoms in the trap. In this way, atoms do not follow the beam but just see the resultant averaged potential. Thus, the request for this type of potential is summarized in the following relation:

$$U_{\text{trap}} \propto I_{\text{trap}} = \langle I(r,t) \rangle_{T_{\text{mod}}} \qquad \text{with} \quad \omega_{\text{mod}} \gg \bar{\omega}, \tag{3.7}$$

where T_{mod} is the modulation period, $f_{\text{mod}} = \frac{\omega_{\text{mod}}}{2\pi}$ is the frequency at which the beam is sweeped and $\bar{\omega} = (\omega_x \omega_y \omega_z)^{\frac{1}{3}}$ is the average trapping frequency. Time-averaged potential can be created in different ways using electro-optic or acousto-optic modulation. The principles of operation is briefly presented below.

Electro-optic deflectors are based on the creation of a gradient in the refractive index of the active material as a result of an applied electric field. Usually, these devices are used to realize time-averaged potentials with complex shape because, since the deflection angle of the beam is directly proportional to the applied voltage across the medium, is much easier to spatially control the beam and thus the geometry of the resultant potential [74, 86]. Furthermore, EODs are preferred to AODs for high resolution applications because of few reasons: the transmittance does not vary as much as in AODs with the deflection, the beam is entirely deflected and AODs usually suffer from systematic angular deviations from linear response to the acoustic driving frequency [84]. On the other hand, EODs are usually quite expensive and the commercial ones are not suited for high power.

Acousto-optic deflectors, as well as acousto-optic modulators (AOMs), consist of an optically transparent material to which a piezo-electric element launches acoustic waves. In this way a periodic change in refractive index, which acts as an optical grating, is created and deflects the laser beam travelling through the crystal. The main difference between AOD and AOM is that the latter has just one radio frequency (RF) signal which drives the acoustic wave. In contrary, in the former there are more than one radio frequency signal which are delayed in phase in such a way to create a resultant signal that makes the response to the acoustic wave uniform over the broadest possible range of deflection angles. The transmittance from an acousto-optic device depends, indeed, on the driving acoustic frequency and it is maximum at the Bragg angle, defined by the following relation:

$$\theta_B = \frac{\lambda f_c}{2v_a}, \tag{3.8}$$

where λ is the wavelength of the laser beam diffracted by the crystal, f_c is the central frequency of the total bandwidth, defined as the frequency at which the diffraction efficiency

reaches its maximum value and v_a is the velocity of the acoustic wave in the material. When the driving frequency is changed to deflect the beam in different points of the space, the diffraction efficiency decreases. With the presence of several electrodes with RF signals progressively delayed in phase, the Bragg condition (3.8) is reached over a larger acoustic frequency range [42].

3.3 Time-averaged potential with acousto-optic devices

When acousto-optic devices are used for standard applications, like adjusting the intensity of the laser beam or shifting the frequency in the RF range in a controlled way, a single driving radio frequency is chosen, to which corresponds a fixed deflection of the beam. The basic idea of creating time-averaged potential, either with AOMs or with AODs, is to send to the piezo-electric element a RF signal modulated with a certain shape. In this way, the beam is deflected horizontally back and forth according to the selected shape. The key feature of this method is the possibility of creating time-averaged potential with different geometry just changing the shape of the driving signal, few simple example are in Fig. 3.2. The figure shows how the beam profile looks like for different shapes of the modulation function, these pictures were taken during a first test of the scanning system with an AOM.

The resultant potential is given by the time-averaged sum of the overlapping Gaussian beams. In our case the beam will be scanned only in the horizontal direction x, this leads to the following expression:

$$U_{\text{tot}}(x,0,0) = \frac{\hat{U}}{T_{\text{mod}}} \int_0^{T_{\text{mod}}} dt \exp\left[-\frac{2(x_S(t)-x)^2}{w_x^2}\right], \tag{3.9}$$

where $\hat{U}$ is the total trap depth defined in Eq. (2.17), T_{mod} is the modulation period, which has to follow the request (3.7), $x_S(t)$ is the function that defines the shape of the potential and w_x is the beam waist along the x direction. The principal use of the scanning system will be to increase the size of w_x, while keeping a Gaussian shape. From earlier experiments [6, 48] an arcus-cosine wave was proved to be suited for this aim.
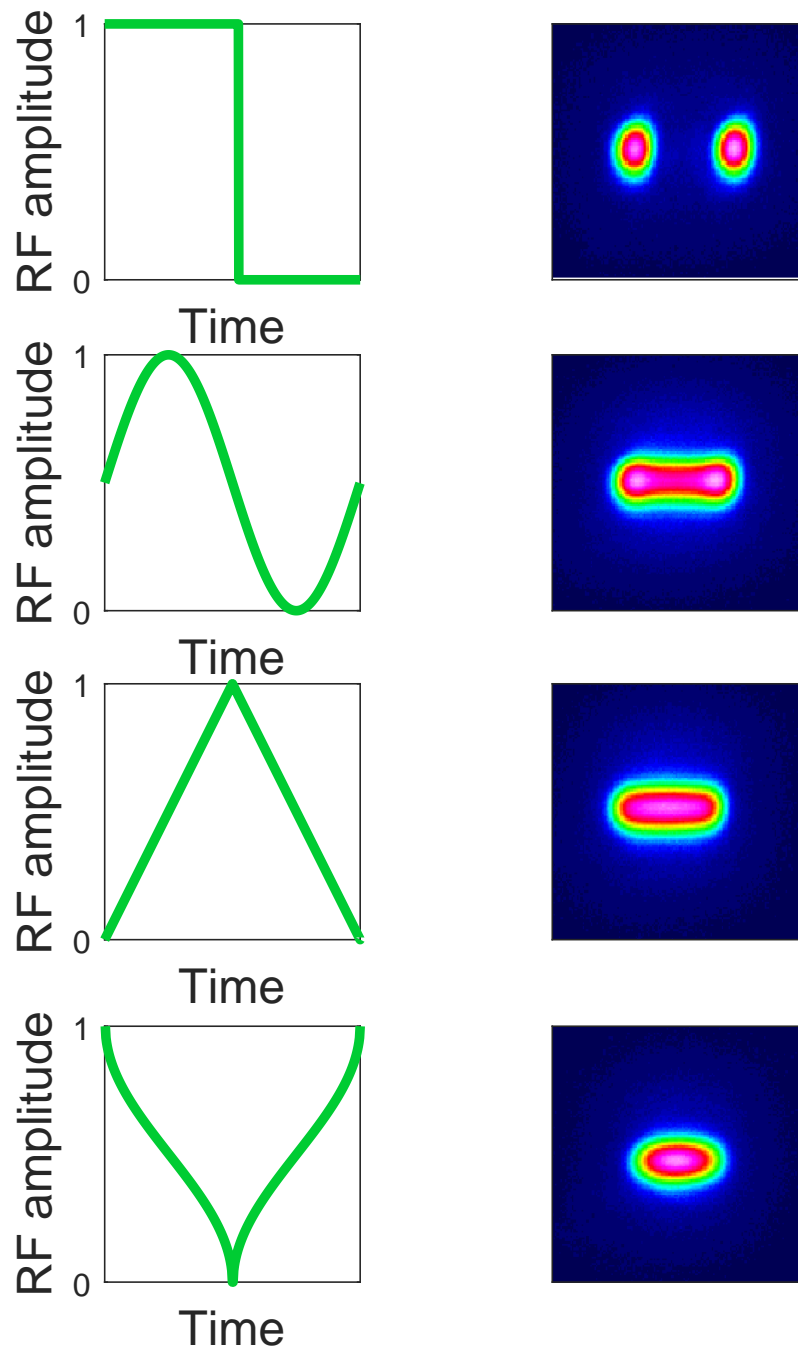
Figure 3.2 Different trap geometry, along the horizontal direction, given by different shapes of the modulated RF signal. Starting from the top, a square wave results in two separated angle deflections and thus two traps for the atoms. A sine and a triangular wave lead to a double well and a box potential, respectively. Finally, a modulation with an arcus-cosine shape, as proved in previous experiments [6, 48], leads to a Gaussian potential. The pictures of the laser beam, shown on the right, were taken with a CCD-camera beam profile during the test of the scanning system with an AOM.

Other functions like sine wave or triangular wave result in a final double well trapping potential and a box potential, respectively. The tools necessary to create an arbitrary time-averaged potential and control his shape during the experimental cycle are combined in Fig. 3.3 and listed below:

- Arbitrary Function Generator (AFG)[3], to create the desired function which has to be sent to the acousto-optic device. The upper limit of the modulation frequency is fixed by the maximum sample rate of the AFG and the number of points of the arbitrary function, directly loaded through USB-stick. In our case, since the maximum sample rate is 250 Msample/s, we choose 1002 points to get a maximum modulation frequency of $\omega_{\mathrm{mod}} = 2\pi \times 250\,\mathrm{kHz}$[4];

- Mixer[5], needed to combine the signal coming from the AFG (V_{signal}) with two other input voltages. One, V_{gain}, is needed to control the amplitude of the RF wave, which is directly related to the width of the resultant time-averaged beam. A second input voltage, V_{offset}, is used as an offset to shift the central frequency of the signal. The mixer combines all the three inputs and gives as output the following signal [4]:

$$V_{\mathrm{mod}} = V_{\mathrm{offset}} + \frac{V_{\mathrm{signal}}V_{\mathrm{gain}}}{10V}. \tag{3.10}$$

Both V_{offset} and V_{gain} can be changed in the range $0\,\mathrm{V} - 10\,\mathrm{V}$. The voltage of the former is chosen accordingly to the voltage-frequency conversion of the VCO. Looking at Eq. (3.10), $V_{\mathrm{gain}} = 0\,\mathrm{V}$ means no modulation, while $V_{\mathrm{gain}} = 10\,\mathrm{V}$ corresponds to a modulation with the maximum amplitude.

- Voltage Controlled Oscillator[6] (VCO), which receives as input a voltage from the mixer and gives as output a frequency which is directly related to the applied voltage. The VCO has a 3 dB modulation bandwidth of 180 kHz and a working range of 50 MHz – 100 MHz. A voltage of 8 V is needed to get an output frequency of 75 MHz. Since the mixer is specified with a maximum output of 10 V, an operational amplifier was implemented in the electronic circuit after the mixer, to reach the voltage range 3 V – 13 V. See Appendix A for the scheme of the electronic circuit;

- Radio frequency amplifier (RF-AMP), which receives the RF signal from the VCO and supplies the acousto-optic device with the RF power needed to achieve a diffraction

---

[3]Model Keysight 33521B.

[4]An higher modulation frequency is not needed at the moment in the experiment. Furthermore, the VCO implemented in the setup would not respond linearly to frequency higher than $2\pi \times 180\,\mathrm{kHz}$.

[5]Model Analog Devices AD734.

[6]Model Mini-Circuits ZX95-100.

efficiency as higher as possible. It is also used, combined with a Voltage Controlled Attenuator (VCA), to actively control the power of the laser beam during the experimental cycle.

In the first part of the thesis a test setup with an acousto-optic modulator[7] was implemented following the electronic scheme shown in Fig. 3.3a. The AOM has a central frequency $f_c = 110\,\text{MHz}$, a RF bandwidth BW $= 15\,\text{MHz}$ and an active aperture of $1.25\,\text{mm}$[8]. Afterwards, another test setup with an AOD[9] was built in order to compare the performance of these two devices for our purpose. The AOD has a central frequency $f_c = 75\,\text{MHz}$, a bandwidth BW $= 32\,\text{MHz}$ and an active aperture of $2.5\,\text{mm}$. Among the measurements, an

(a) AOM.

(b) AOD.
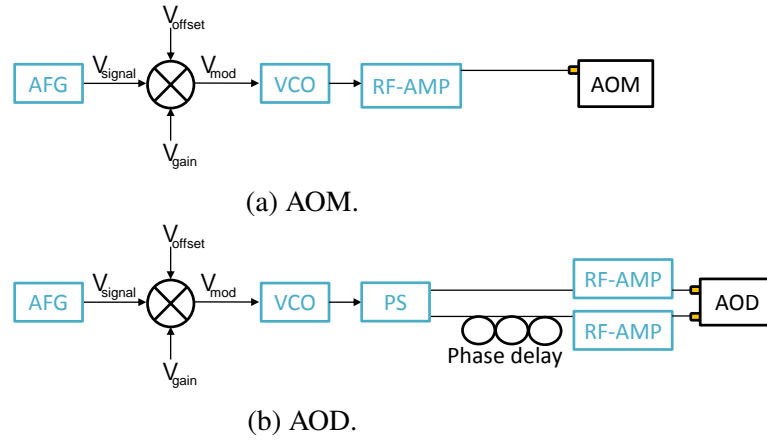
Figure 3.3 Sketch of the electronic scheme used for AOM (a) and AOD (b). A mixer combines the signal coming from the AFG (V_{signal}) with V_{gain} and V_{offset}. The resultant V_{mod} is sent to the VCO, which converts it in a radio frequency output. In the case of the AOM, this output is amplified by the RF-AMP and sent to the AOM. For the AOD, a power splitter (PS) generates two signals, which feed two different RF-AMPs. SMA cables, with a well defined length difference, are used to create a delay in phase between the two signals.

interesting one for our purpose examines the dependence of the diffraction efficiency on the frequency of the RF signal and thus, on the angle of deflection. In Fig. 3.4 the large bandwidth of the AOD is clearly visible compared to the restricted one of the AOM. The diffraction efficiency of the AOM decreases dramatically when the frequency moves away from the central one. After $10\,\text{MHz}$ already a reduction of almost 30% is visible. In the contrary, the efficiency of the AOD is kept almost constant up to $15\,\text{MHz}$ from f_c. The AOD minimizes the decreasing of the diffraction efficiency when the frequency is shifted far

---

[7]Model 3110-197 Gooch & Housego.

[8]The active aperture is $2.5\,\text{mm} \times 1.25\,\text{mm}$ but the smaller dimension has to be considered as an effective aperture to not cut the beam along that direction.

[9]Model 4075-2 from Crystal Technology, Inc.

away from the central one, thus it is more suited for the purpose of creating a time-averaged potential. Furthermore, the active aperture of the AOM is smaller than the one of the AOD, this makes the latter even more suited for our system, which uses a high power laser. These motivations drove us to the choice of a setup built with the AOD. A sketch of the electronic setup implemented for this device, is shown in Fig. 3.3b. The deflector has two radio frequency inputs to compensate for the deviation from the Bragg condition (3.8). A power splitter[10] receives the output of the VCO and creates two RF signals. Each of them feeds an RF-AMP, travelling along two SMA cables with different lengths[11], in such a way to create a delay in phase.
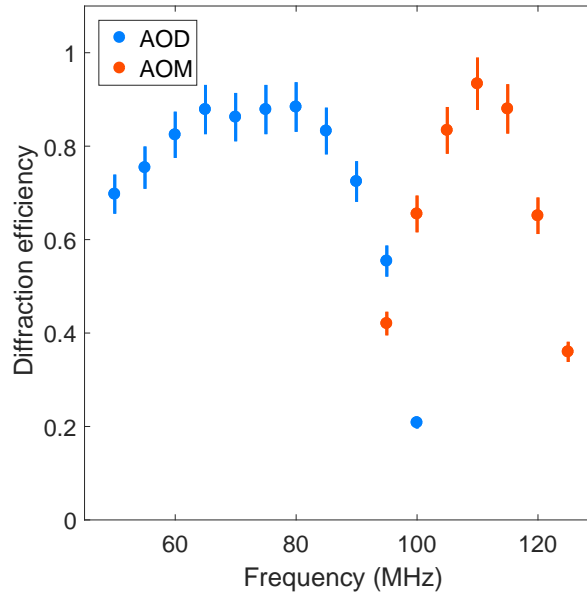
Figure 3.4 Diffraction efficiency measured changing the driving frequency of the AOD (blue points) and AOM (orange points). Starting from the central frequency of the AOM ($f_c = 110\,\mathrm{MHz}$), already at $10\,\mathrm{MHz}$, the efficiency is reduced by almost 30%, while for the AOD is kept nearly constant up to $15\,\mathrm{MHz}$ from $f_c = 75\,\mathrm{MHz}$.

3.3.1 Optical setup: scanning system

In addition to the electronics needed to control the AOD, from the point of view of optical elements, the setup necessary to create a time-averaged potential requires few parts: the AOD and a lens placed at a distance of one focal length, whose task is to transform angle deflections in horizontal shifts. To adjust the beam waist to the desired value on the atoms at the center of the chamber, a telescope can be realized using as a first lens the one in front of

---

[10]Model MiniCircuits ZFSC-2-1-S+.

[11]The right length difference (Δl) is provided by the company. In our case $\Delta l = 2.461\,\mathrm{m}$.

the AOD. A simple sketch of the setup is shown in Fig. 3.5. The range, in which the laser
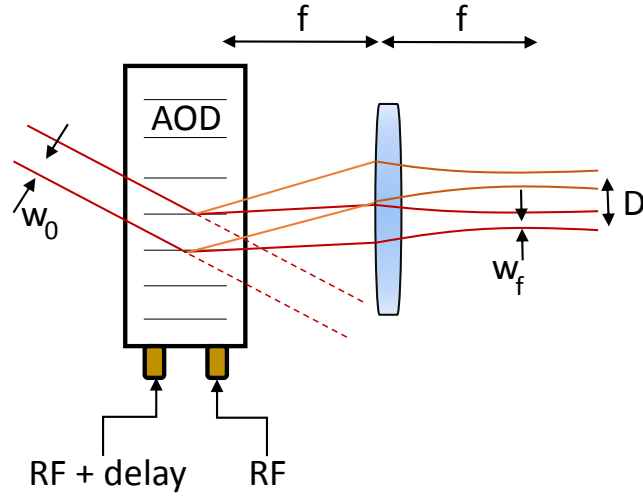

Figure 3.5 Working principle of the scanning system. The AOD has two electrodes for two RF inputs. The electrode on the left receives the RF signal with a delay in phase with respect to the one on the right. A lens, placed at a distance of one focal length from the AOD, converts the angle deflections in horizontal shifts. The main quantities that play a role in the maximum aspect ratio achievable are depicted (w_0, w_f, f and D).

beam can be deflected, fixes the maximum width of the resultant potential and the AR of the trap. This quantity is strictly related to two parameters: the resolution (R), which is the number of resolvable spots, and the bandwidth (BW) of the AOD. In our case the dimension of one spot is given by the diameter of the beam in the focus of the lens ($2w_f$). The maximum distance by which the beam can be deflected (D) is given by the RF bandwidth, which is fixed by the frequencies at which the diffraction efficiency decreases by 3 dB. Thus, the resolution can be written as:

$$R = \frac{D}{2w_f}. \tag{3.11}$$

It is useful to express R in terms of the AOD's parameters and the laser beam waist. To do this, Eq. (3.8) and the following relations can be used:

$$w_f = \frac{\lambda f}{w_0 \pi}, \qquad D = \frac{\text{BW} D_0}{f_c}, \qquad D_0 = \theta_B f,$$

where w_0 is the waist of the incoming beam, f is the focal length of the lens and D_0 is the shift of the beam relative to the zero order. Equation (3.11) can then be expressed as below:

$$R = \frac{2\pi}{4v_a} w_0 \text{BW}. \tag{3.12}$$

The resolution and thus the final aspect ratio achievable, depends only on the intrinsic characteristics of the AOD and on the initial beam waist of the laser beam. The telescope built afterwards will not influence this value at all. For fixed BW and v_a, which depend on the device, by increasing the initial beam waist w_0 it is possible to achieve larger values of resolution. The limit is, of course, imposed by the active aperture of the AOD.

The crystal of the AOD used in the setup is made of TeO_2, to which corresponds a sound velocity $v_a = 4200 \, \text{m s}^{-1}$. Considering our values of v_a and BW and taking as w_0 the maximum waist of the incoming laser beam, fixed by the AOD's active aperture $w_0 = 1.25 \, \text{mm}$, Eq. (3.12) leads to a maximum theoretical value of AR $= 15$.

As a first test, instead of the system made by VCO, power splitter and cables with different lengths, a function generator[12] able to create two signals at a frequency of 75 MHz with a delay in phase, was used. The signal from the AFG, with an amplitude expressed in V_{pp}, can be superimposed on the RF signals as external modulation. The radio frequency ranges, covered during the scanning, are related to the voltage amplitude of the modulation, the calibration is reported in Table 3.2.

Table 3.2 Radio frequency ranges correspondent to different values of voltage amplitude of the modulation.

Modulation amplitude	
Voltage (V_{pp})	Frequency (MHz)
0	75
1	70 – 80
2	65 – 85
3	60 – 90
4	55 – 95

The scanning is applied on the laser beam used for the horizontal ODT. This beam propagates along the y direction and the modulation involves the x direction (z corresponds to the axis of gravity). To verify the performance of the scanning, after selecting an arcus-cosine function as modulation, the beam waist was measured using a CCD-camera beam profiler[13] along both directions (x and z). In the following measurements, the size of the incoming beam was adjusted with a telescope in order to get $w_0 = (1.15 \pm 0.01) \, \text{mm}$, this leads to a predicted resolution of $R = 14$ according to Eq. (3.12). The plot in Fig. 3.6 shows,

---

[12]Model RSDG5162 from RS Pro.

[13]Model BC106-VIS CCD-camera beam profiler from Thorlabs. This camera has a pixel size of $6.45 \, \mu\text{m} \times 6.45 \, \mu\text{m}$, an aperture size of $8.8 \, \text{mm} \times 6.6 \, \text{mm}$ and can measure beam diameter down to $30 \, \mu\text{m}$.
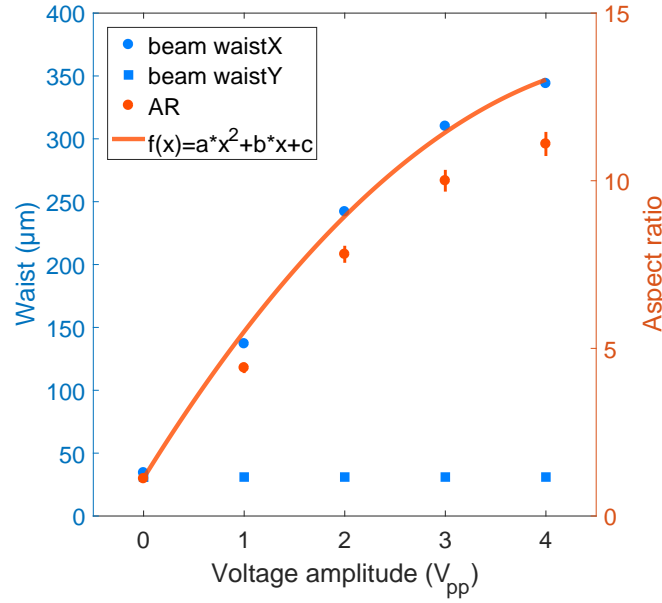
Figure 3.6 Measurement of the waist as a function of the modulation amplitude, expressed in V_{pp}. The axis on the left shows the waist along both directions x and z, whereas the axis on the right shows the resultant AR. The orange curve shows the fit function $f(x) = ax^2 + bx + c$. Where $a = -12.4\,V_{pp}^{-2}$, $b = 129.0\,V_{pp}^{-1}$ and $c = 30.2\,\mu m$.

on the left axis, the beam waist measured along the x (circles) and z (squares) directions while, on the right axis, the resultant AR. The data shown in the plot are obtained taking with the CCD the x and z profile of the beam for each chosen voltage amplitude and fitting the curve with a Gaussian function. In a first test of the dipole trap the beam waist at the center of the chamber was planned to be around $w_0 = 35\,\mu m$. Thus, starting from a beam waist of $w_x = (34.4 \pm 0.5)\,\mu m$, along x, and $w_z = (30.9 \pm 0.8)\,\mu m$, along z, the final beam waist achieved with the maximum modulation amplitude reads $w_x = (344 \pm 1)\,\mu m$ and $w_z = (31 \pm 1)\,\mu m$, respectively, leading to the aspect ratio AR $= 11.1 \pm 0.4$. In Table 3.3 all the measured waists for different modulation amplitudes and the relative AR are listed.

The next step is to check that the shape of the beam modulated with an arcus-cosine wave follows a Gaussian function. The profile along the x direction, taken again using the CCD-camera beam profiler, is shown in Fig. 3.7. This profile displays a single pixel row of the received image and on the curve is shown the relative intensity (100% represents the maximum on that row). On the left side of the figure the Gaussian profile of the beam is shown without any modulation on. Whereas, on the right side, the profile resultant from a maximum amplitude of the modulation ($4\,V_{pp}$) is displayed. The Gaussian fit follows in a nice way the experimental points.

Table 3.3 Beam waist measured along the x and z directions for different modulation amplitudes. The beam itself is slightly elliptic, thus the AR starts from 1.11 ± 0.03, with no modulation, and reaches the maximum value of 11.1 ± 0.4.

Amplitude (V_{pp})	w_x (μm)	w_z (μm)	AR
0	34.4 ± 0.5	30.9 ± 0.8	1.11 ± 0.03
1	137 ± 2	31 ± 1	4.4 ± 0.2
2	242 ± 1	31 ± 1	7.8 ± 0.3
3	310 ± 1	31 ± 1	10.0 ± 0.3
4	344 ± 1	31 ± 1	11.1 ± 0.4

A second test was made choosing a triangular wave as modulation function in order to check the maximum range in which the time-averaged potential assumes the shape of a box along the direction of the scanning. The measurements, relative to the triangular function, are shown similarly to the arcus-cosine case in Fig. 3.8. The beam profile looks quite uniform up to a frequency range of $70 \, \text{MHz} - 80 \, \text{MHz}$. Afterwards, it starts to assume a different shape quite close to a Gaussian function. This is probably due to the high harmonics induced by the sharp corners of the triangular wave, which will need further investigation. The maximum beam size, measured for the two different modulation shapes are shown in Table 3.4 with the correspondent aspect ratio.

Table 3.4 Maximum beam size and relative aspect ratio, choosing an arcus-cosine and a triangular function as modulation for the driving frequency.

Modulation function	Maximum beam size (μm)	AR
Arcus-cosine	344 ± 1	11.1 ± 0.4
Triangular	388 ± 2	12.5 ± 0.4

3.3.2 Driving RF signal

To fully test the performance of the scanning system, in the previous measurements, the initial waist of the incoming beam was chosen close to the limit of the active aperture of the AOD and the modulation frequency was fixed in a region in which the effective bandwidth was not limited by the electronics ($\omega_{mod} = 2\pi \times 1 \, \text{kHz}$). When shining the time-averaged beam on the atoms, the modulation frequency has to be much higher than the oscillation frequency of the atoms in the trap. In particular, it has been proved that f_{mod} has to be at

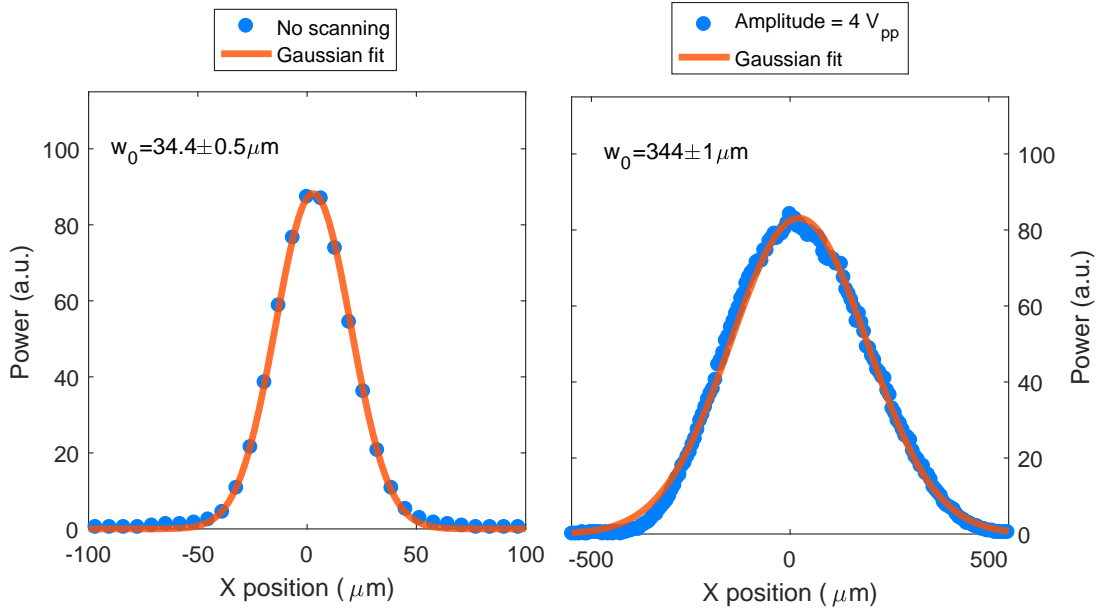Figure 3.7 Beam profile along the direction of the scanning (x) for a not modulated driving frequency (left) and for an arcus-cosine shape of the modulation with the maximum amplitude $4\,V_{pp}$ (right).

least 100 times larger than ω_x to not induce heating [64]. Thus, from the simulation shown in the Chapter 2, the modulation frequency should be around $\omega_{mod} = 2\pi \times 400\,\text{kHz}$ to satisfy this rule. However, find a VCO suitable for a center frequency of $f_c = 75\,\text{MHz}$ with such high RF modulation bandwidth, is not straightforward. The VCO implemented, up to now, has a modulation bandwidth of $\omega_{mod} = 2\pi \times 180\,\text{kHz}$.

Already at $\omega_{mod} = 2\pi \times 50\,\text{kHz}$, the VCO starts to cut the range of radio frequencies sent to the AOD and this leads to a smaller aspect ratio achievable. In the experiment the AOD is controlled with the electronic scheme shown in Fig. 3.3b and the modulation frequency is fixed to $\omega_{mod} = 2\pi \times 100\,\text{kHz}$. In Fig. 3.9 the RF bandwidth, measured looking the signal coming out of the RF-AMPs and sent to the AOD on a spectrum analyzer, is plotted for three different modulation frequencies ($f_{mod} = 10\,\text{kHz}$, $50\,\text{kHz}$ and $100\,\text{kHz}$) changing the voltage V_{gain} responsible for the modulation amplitude. For the modulation frequency of $100\,\text{kHz}$, the VCO levels out the maximum RF bandwidth at around $8\,\text{V}$. The RF signal sent to the channels of the AOD, for three different values of V_{gain} ($0\,\text{V}$, $4\,\text{V}$ and $8\,\text{V}$), is shown in Fig. 3.10 for a triangular wave as modulation function.

The influence of the VCO on the final achievable size of the beam is clearly seen in Fig. 3.11. For this test the initial beam waist was $(46.4 \pm 0.7)\,\mu\text{m}$ and the modulation amplitude was fixed at $V_{gain} = 5\,\text{V}$. Increasing the modulation frequency the width of the beam decreases. For an arcus-cosine function, at the end of the bandwidth, the beam size is
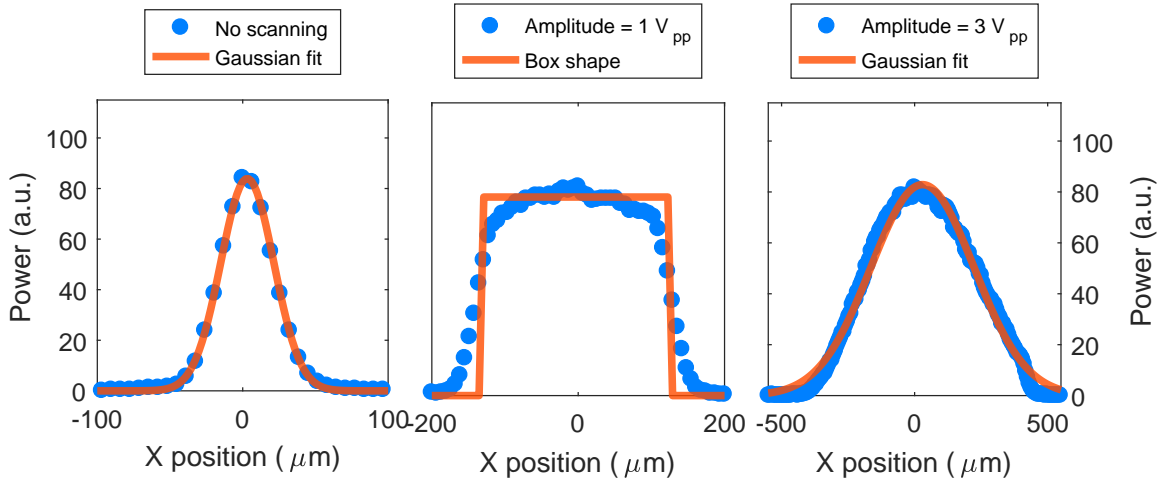
Figure 3.8 Beam profile along the direction of the scanning (*x*) for a not modulated driving frequency (left) and for a triangular shape of the modulation with an amplitude of $1\,V_{pp}$ (center) and $3\,V_{pp}$ (right). The beam profile looks quite uniform up to a range of $70\,MHz - 80\,MHz$, afterwards it starts to assume a nearly Gaussian shape.

reduced by 15% with respect to the one measured at $60\,kHz$. The reduction is stronger for the triangular wave where, at the modulation frequency limit, the reduction is of almost 25%.

To summarize the motivations that drove our choice for the acousto-optic deflector, advantages and disadvantages of the three tested systems are listed as follows:

- **Cylindrical lenses**: the setup built with cylindrical lenses has the advantage to change the real aspect ratio of the laser beam. This leads to an optical dipole trap with Gaussian behaviour in all the three directions. On the other hand, the lenses need to be moved on a linear stage. This means dealing with the drawback of movement of mechanical parts, which could affect the beam pointing stability necessary for an efficient optical trap. Thus, to be implemented, the system requires good translational stages in terms of deviations from the true direction of travel and reproducibility. Furthermore, during an experimental cycle, the beam waist has to be tuned on time scales down to $10\,\mu s$, demanding high maximum velocity. All these conditions require an expensive translational stage, whose price would be comparable to the cost of two acousto-optic deflectors.

- **Acousto-optic modulators**: these devices have been used since decades now and have the advantage to be well known systems. However, for time-averaged potential applications, diffraction efficiency curves as uniform as possible are required. Thus, the short bandwidth of the AOM is often corrected rescaling the diffraction curve to the minimum value, with a dramatic impact on the output power.
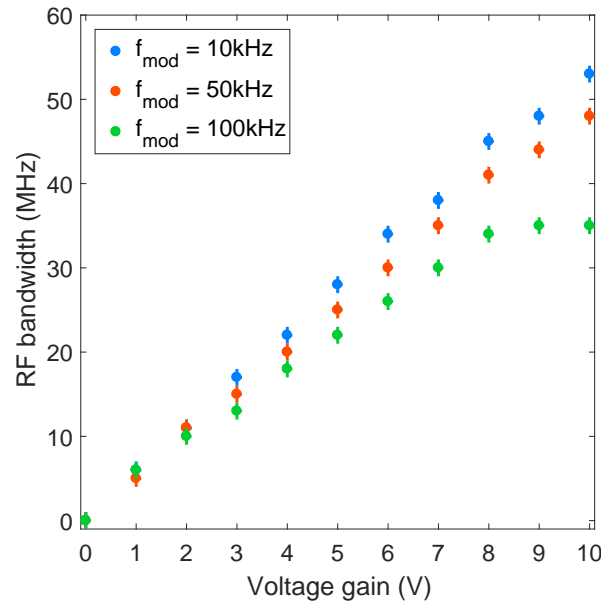
Figure 3.9 Measurement of the radio frequency bandwidth as a function of V_{gain} for different values of modulation frequencies (10 kHz, 50 kHz and 100 kHz). For a modulation frequency of 100 kHz, the VCO levels out the maximum RF banwidth at around 8 V.
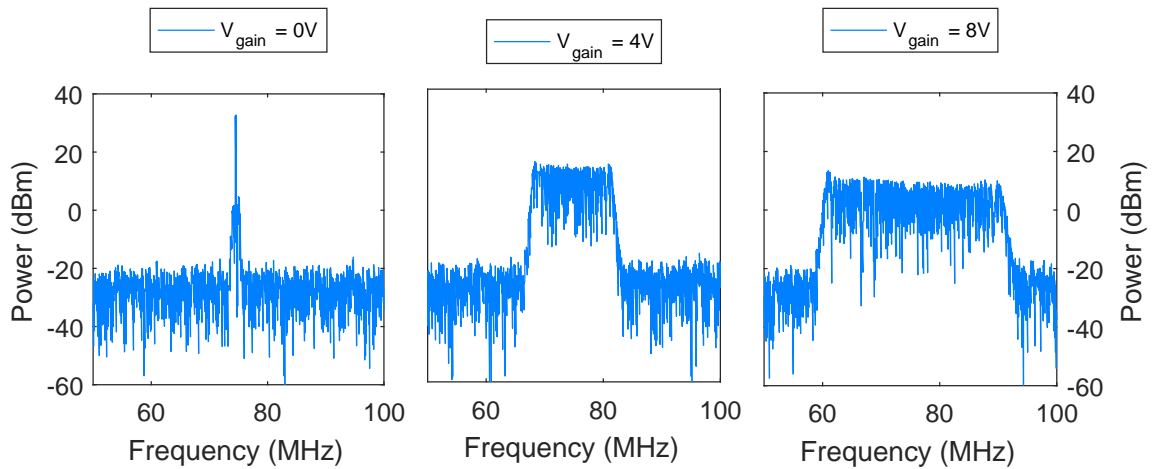

Figure 3.10 Radio frequency signal, coming out from the RF-AMPs and sent to the AOD, measured with a spectrum analyzer. The three plots show the signal for different modulation amplitude (0 V, 4 V and 8 V), choosing as modulation function a triangular wave. Each channel of the AOD receives a maximum RF power of 33 dBm (2 W).

- **Acousto-optic deflectors**: these devices are made for applications in which the laser beam has to be deflected back and forth maintaining the diffraction efficiency curve almost constant. They, as the modulators, are easily controllable in experimental cycles tuning the driving RF frequency and changing the RF-AMP parameters. Both AOMs and AODs exhibit the drawback of the creation of a resultant potential which
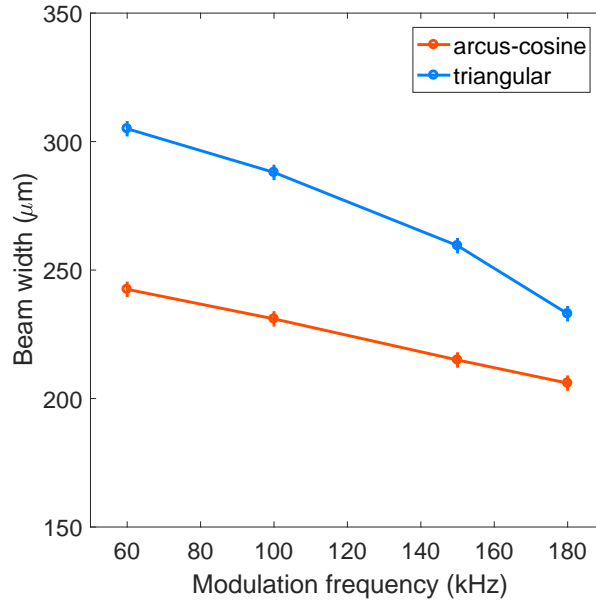
Figure 3.11 Reduction of the beam size for increasing modulation frequencies, induced by the limited bandwidth of the VCO. In this test the initial beam waist was $(46.4 \pm 0.7)\,\mu$m and the modulation amplitude was fixed at $V_{\text{gain}} = 5\,$V.

does not follow the behaviour of a Gaussian beam along the direction of propagation. Furthermore, they require high modulation frequencies, which are quite often difficult to reach for central radio-frequencies in the range $0\,$MHz $- 200\,$MHz. Even if AOD results in a more complex system with respect to the AOM because it requires several RF inputs, it is the most suited for creating time-averaged potentials, among the three tested systems.

3.3.3 Measurement of the waist

The setup was built to reach a waist of around $w_x = w_z = 20\,\mu$m. The measurement of the beam waist is crucial to fully characterize the dipole trap and for further measurements of the polarizability. To estimate the value of the beam waist, the CCD-camera beam profile was mounted on a linear stage and moved in such a way to scan the laser beam along the direction of propagation (y). The data, taken for the horizontal beam of the dipole trap, are plotted in Fig. 3.12. In each point, the $1/e^2$ radius of the beam along the x and z axis is measured. The right side of the figure shows a zoom of the region around the foci. The points are fitted with the expression for the radius of a Gaussian beam, given by Eq. (2.15). From the fit the beam waists of the horizontal beam, along the x and z directions, are $w_x = w_z = (20.5 \pm 0.2)\,\mu$m. Where the uncertainty are given by the statistical errors of the fit. Around the focal points, the fit for both directions does not follow nicely all the data. This can be related to the difficulty
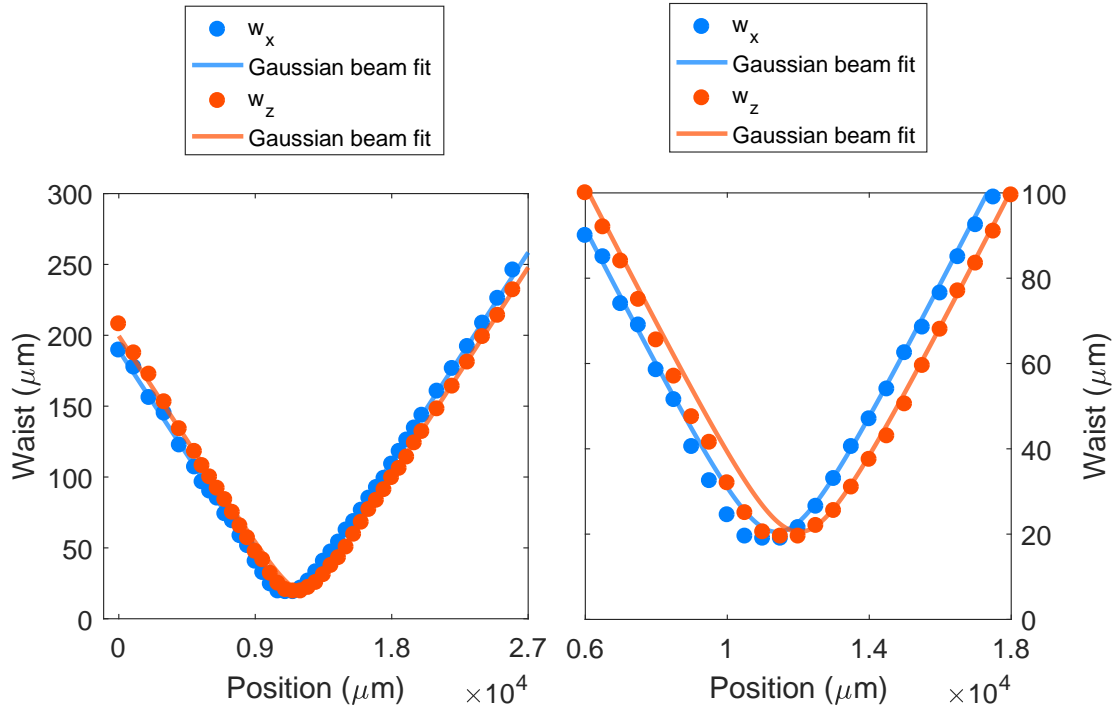
Figure 3.12 Measurement of the beam waist along the x (blue) and z (red) axis of the horizontal beam. The data points are the $1/e^2$ radius of the beam measured with the CCD-camera beam profiler. The plot on the right is a zoom of the region around the foci.

of measuring such small beam waists with the CCD-camera beam profiler. A beam waist of 20.5 μm is, indeed, quite close to the resolution limit of the CCD, which can measure beam diameters down to 30 μm.

In the RARE experiment the vertical dipole trap, which crosses the horizontal one and propagates along the z axis, is obtained splitting the initial beam coming from the laser head with a polarizing beam splitter (PBS) and a waveplate ($\lambda/2$). In this way, with a motorized waveplate, the power can be redistributed arbitrarily during the experimental cycle between the horizontal and the vertical beam. The beam waist of the vertical beam is measured similarly to the horizontal one. The results are shown in Fig. 3.13. As for the hODT, the data are fitted with the relation of the Gaussian beam radius. The fit gives as results the beam waists of the vertical beam, along the x and y directions, $w_x = (101.3 \pm 0.2)$ μm and $w_y = (95.0 \pm 0.2)$ μm. The uncertainties are given by the statistical errors of the fit.

From the measurement relative to the horizontal optical dipole trap, there is a clear difference in the position of the foci along the two different axes. This value is comparable to the Rayleigh length and leads to an astigmatic beam. On the contrary, the astigmatism does not affect the vertical beam in which the distance of the foci is much less than the Rayleigh length. All the result of the beam waist measurements are summarized in Table 3.5.
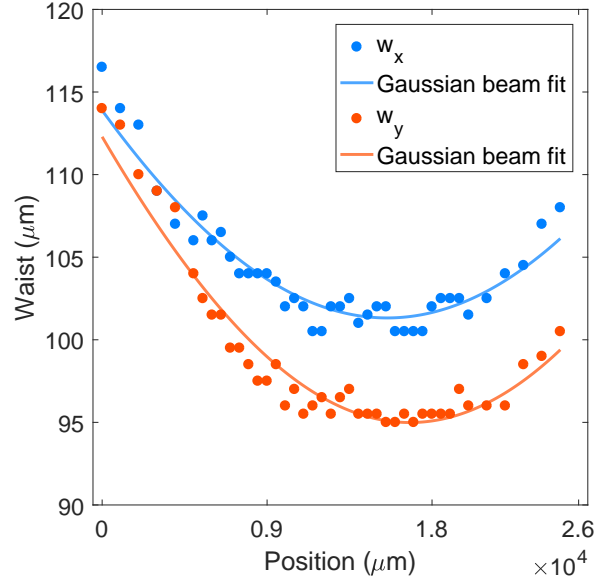
Figure 3.13 Measurement of the beam waist along the x (blue) and y (red) axis of the vertical beam. The data points are the $1/e^2$ radius of the beam measured with the CCD-camera beam profiler.

Table 3.5 Measured beam waist of the horizontal and vertical optical dipole trap. Δy and Δz represent the shift between the foci of the horizontal and vertical beam, respectively. z_{R_h} (z_{R_v}) is the Rayleigh length of the horizontal (vertical) beam.

	Beam waist (μm)		Astigmatism (mm)	Rayleigh length (mm)
Horizontal beam	w_x 20.5 ± 0.2	w_z 20.5 ± 0.2	Δy 0.6 ± 0.1	z_{R_h} 1.2
Vertical beam	w_x 101.3 ± 0.2	w_y 95.0 ± 0.2	Δz 1.2 ± 0.4	z_{R_v} 28.3

In Fig. 3.14 is shown how the beam waist, starting from $w_x = 20.5\,\mu$m increases as a function of the modulation amplitude (V_{gain}). The rise of the waist is levelled out due to the limitation in the bandwidth of the VCO, as discussed previously. This effect is enhanced by the fact that to make the electronic circuit more compact the voltage range sent to the VCO was reduced. At the moment in the experiment it seems we are not limited by this effect for the loading of the ODT, for both species of erbium and dysprosium, if necessary the electronics can be easily modified as shown in Appendix A.
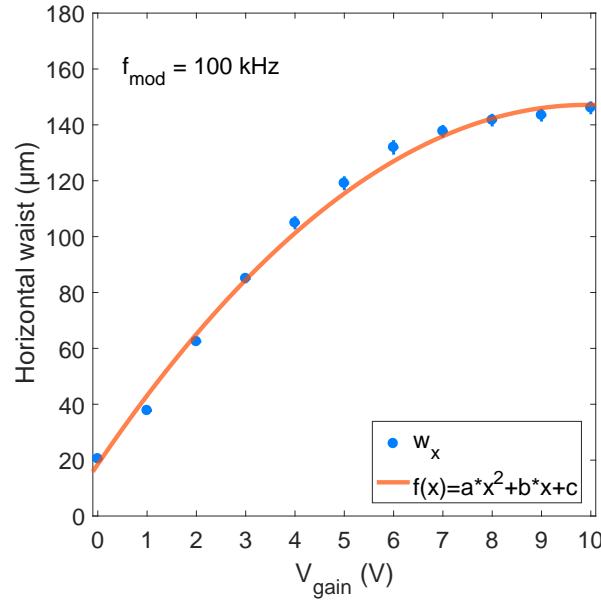
Figure 3.14 Dependence of the beam waist on the modulation amplitude (V_{gain}) choosing the arcus-cosine function as modulation with a frequency of $f_{\text{mod}} = 100\,\text{kHz}$. The limited bandwidth of the VCO levels out the curve around 7 V. The orange curve shows the fit function $f(x) = ax^2 + bx + c$. Where $a = -1.3\,\text{V}^{-2}$, $b = 25.9\,\text{V}^{-1}$ and $c = 18.5\,\mu\text{m}$.

3.3.4 Implementation in the experiment

After the test, the setup was built on a small breadboard to be implemented in the experiment. The final setup of the horizontal and vertical dipole trap is shown in Fig. 3.15. The 1064-nm light comes from a 50 W Yb^{3+} fiber laser. In the laser head is already included an high power infrared (IR) isolator to prevent damage coming from intense back reflections. This reduces the available power to 45 W. After the laser head the beam path is folded several times due to a bad shape of the profile in the near field. Two systems, PBS plus waveplate ($\lambda/2$), control the distribution of the power. In particular, the first controls the total power[14] and the second controls the power distribution between the horizontal and vertical ODT. In the picture, the path of the horizontal beam is depicted in red while the vertical one in yellow. On the hODT path, after the AOD, a series of lenses are installed to get a final waist of $w_x = w_z = 20.5\,\mu\text{m}$ on the atoms. All the lenses and mirrors are made by Fused Silica and coated for 1064 nm[15]. Indeed, due to the high power, it is preferable to use Fused Silica instead of the standard N-BK7, which has a thermal expansion coefficient 14 times higher, to prevent thermal lensing effect. As discussed in Chapter 2, the lifetime of the atomic sample strongly depends on the

---

[14]This was installed for preliminary test, since the minimum power coming out of the laser is 400 mW, and it will be removed afterwards.

[15]The lenses and the high power mirrors are from the company LENS-Optics. High power mirrors: M1064/1"-2"/45. Fused Silica lenses: LPX1"Q, LPV1"Q.

light polarization due to the tensorial nature of the atomic polarizability. Thus, a waveplate is placed behind the last lens to rotate the linear polarization. The AOM in the vertical path is not involved in any scanning but plays the role of controlling the power of the laser beam during the experimental cycle. All the shutters implemented in the setup of the optical dipole trap are built with high power mirrors and fan-cooled[16] beam dumps.

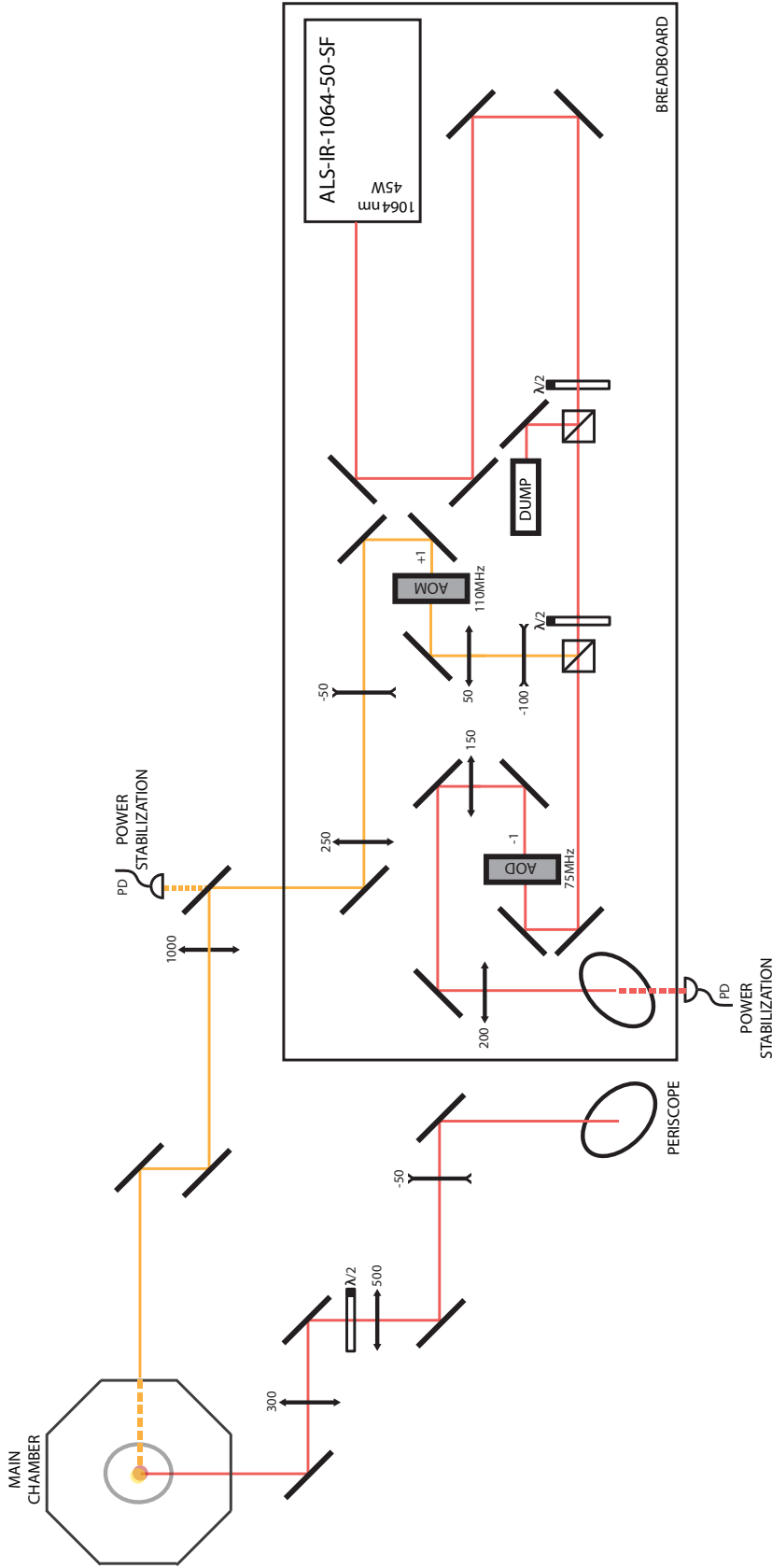[16]This system will be exchanged with water-cooled beam dumps.

Figure 3.15 Scheme of the optical dipole trap setup. After the laser head two systems, PBS plus waveplate ($\lambda/2$), control the distribution of the power. The path of the horizontal beam is depicted in red while the vertical one in yellow. On the hODT path, after the AOD, a series of lenses are installed to get a final waist of $w_x^h = w_z^h = 20.5\,\mu m$ on the atoms. The AOM on the vODT path controls the power of the vertical beam during the experimental cycle. The beam waist is adjusted to the final size $w_x^v = 101.3\,\mu m$ and $w_y^v = 95.0\,\mu m$. The grey circle in the main chamber represents the mirror used to reflect the MOT and vODT beams from the bottom along the axis of gravity.

Chapter 4

Measurements with atoms

The previous chapters introduced the tools necessary to characterize an optical dipole trap, as trap depth, trap frequencies, and polarizability. We also discussed the possibility to change dynamically the trap geometry as an additional degree of freedom and how to implement it in the experimental cycle. This chapter is devoted to test the ODT on atoms. In particular, the first section introduces the RARE experimental apparatus. The second section focuses on the effect of the scanning system on the atom loaded into the ODT. The third section treats the trap frequency measurements as a tool to characterize the trap geometry and to determine the polarizability, and the final section is devoted to the planning of further evaporative steps.

4.1   RARE experimental setup

RARE experiment combines for the first time Er and Dy in a dual species machine which, with a three-chamber concept, will investigate several aspects of dipolar physics. The apparatus is shown in Fig. 4.1. The atom flux of Er and Dy is created in a commercial oven[1], in which solid pieces of Er and Dy in form of alloy are evaporated at a temperature of about 1100 °C. The oven includes two sections: the effusion cell, which contains the material, and the hot lip[2]. The two species have close melting temperature (1414 °C and 1529 °C for Dy and Er, respectively [43]) resulting in a similar atom flux density. To compensate the difference in melting point, and thus atomic flux[3], Er was added recently in the hot lip section, which operates at 1150 °C. The atomic beam is collimated first, through a set of apertures in the oven section and then through two-colour transversal cooling, using the

---

[1]Model DFC-40-10-WK-2B from CreaTec Fischer & Co. GmbH.

[2]The effusion cell is usually operating at a temperature of 1100 °C, while the hot lip is set to a temperature of 1150 °C.

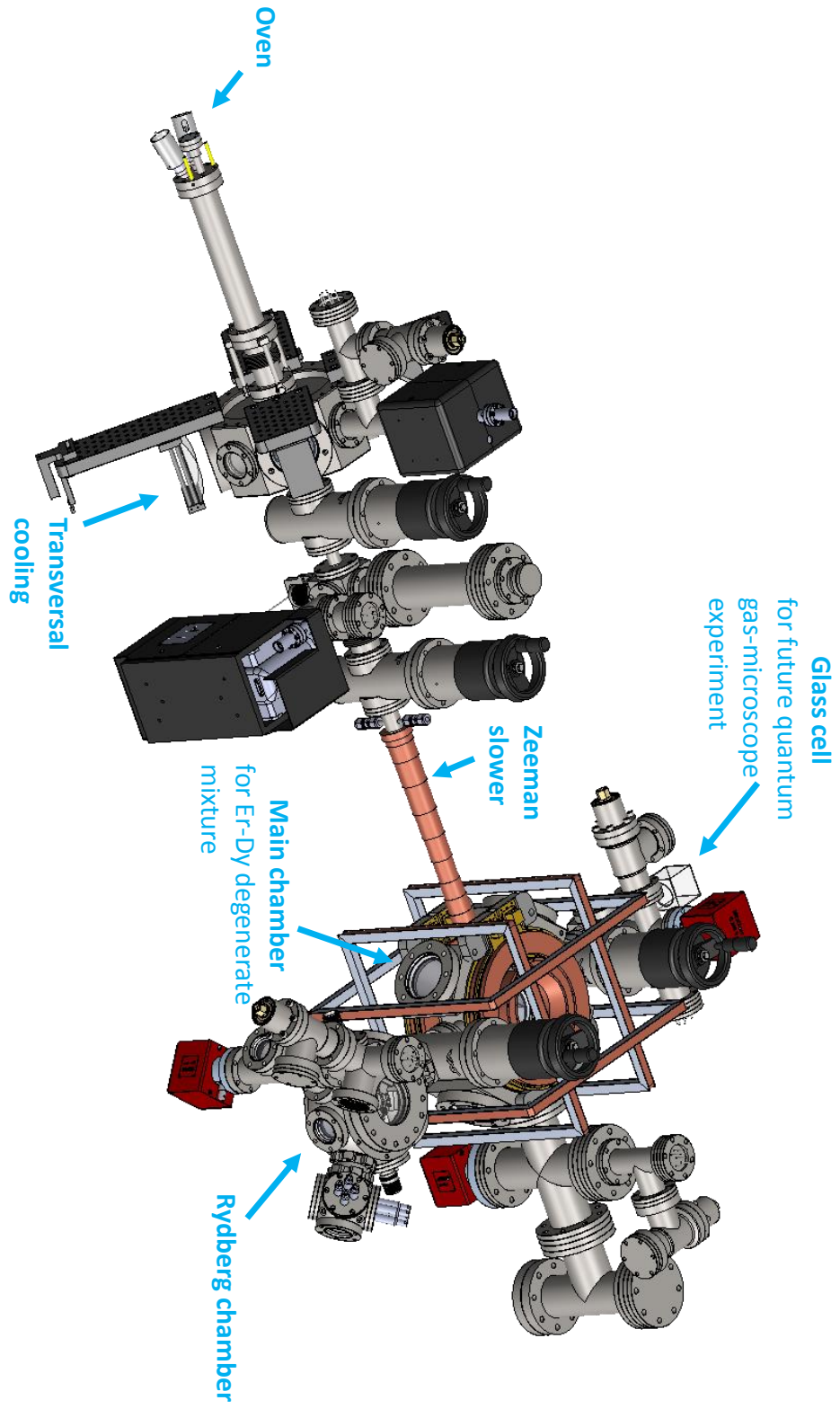[3]Erbium has a lower vapour pressure, which leads to a lower evaporation rate.

Figure 4.1 RARE experimental apparatus. The oven generates the atomic flux of Er and Dy, which is then collimated by a two-colour transversal cooling (401-nm light and 421-nm for Er and Dy, respectively). The Zeeman slower slows the atoms down to the capture velocity of the two-colour MOT (583-nm light and 626-nm for Er and Dy, respectively). The figure shows the three chambers: main chamber, Rydberg chamber and the future glass cell for quantum gas-microscope experiment. Up to now, only the main chamber is fully implemented and operative.

Oven

Transversal cooling

Glass cell for future quantum gas-microscope experiment

Zeeman slower

Main chamber for Er-Dy degenerate mixture

Rydberg chamber

401-nm light for Er and 421-nm for Dy [31]. Atoms are then slowed by the Zeeman slower down to the respective capture velocity of the MOT (few $\mathrm{m\,s^{-1}}$). The RARE experimental setup plans to include three chambers. Atoms will be moved from one chamber to the others by implementing an optical transport.

In the main chamber atoms of Er and Dy are trapped first in the MOT and then they are transferred into the ODT for evaporative cooling to the degenerate phase. The MOT provides a confining force which, in our case, is comparable to gravity. Thus, the shape of the atomic cloud is deformed and atoms accumulate to the lower boundary of the MOT, from which they predominantly absorb light from the bottom and get spin-polarized in the Zeeman sublevel $m_J = -6$ and $m_J = -8$ for erbium and dysprosium, respectively. This particular feature allows a MOT configuration, which employs only five beams instead of the standard six beams. With only five beams, the laser beam coming from the bottom does not need to be retro-reflected, leading to free optical access from the top side of the chamber. The MOT parameters as power, detuning, magnetic field gradient and compression time are optimized to load both species simultaneously into the ODT. The ODT setup consists of an horizontal beam (hODT) travelling along the y direction and a vertical beam (vODT) travelling along the axis of gravity z. Figure 4.2 shows a top view of the main chamber with the laser beams of MOT, ODT and ZS.

The second chamber is dedicated to Rydberg physics, in which atoms are excited in states with a principle quantum number $n \gg 1$. The high value of n, usually in the range of $20-100$, leads to typical sizes of the electronic wave function on the order of $\approx$ nm and to extraordinarily large electric dipole moment [16, 32].

In the third chamber a single site resolution imaging [7, 80] is planned to detect single atoms in a optical lattice. Among the three only the main chamber is, up to now, fully implemented and operative.

The RARE experiment plans to investigate, in the main chamber, the behaviour of dipolar atoms in presence of a magnetic field B, which polarizes the sample. In particular, the influence on the interactions of the dipolar imbalance induced by the different magnetic moment can be studied together with the interspecies scattering physics. Furthermore, in the single-site imaging chamber, dipolar atoms will be studied in an ideally zero magnetic field ($B \approx 0$). In this way, atoms are not forced by the external field to orient the spin in a fixed direction and the magnetization is free. To study this particular behaviour, the B field has to be controlled at the $100\,\mu\mathrm{G}$ level [67]. Due to this reason, to compensate the earth's magnetic field and other external magnetic fields, compensation cages will surround all the three chambers and the optical table. Furthermore, mostly all the equipment on the optical

table devoted to the experimental apparatus (screws included) is made by non magnetic materials.
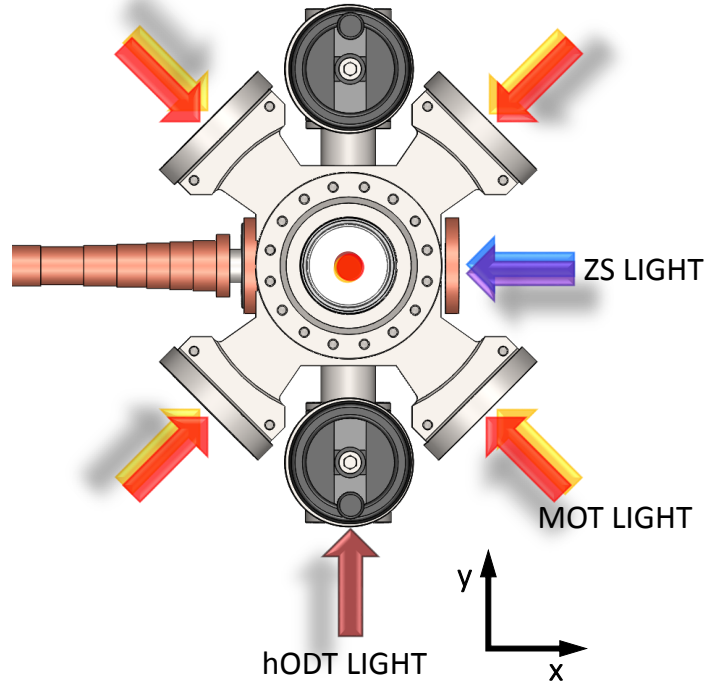

Figure 4.2 Top view of the main chamber. Atoms, travelling along the *x*-axis, are slowed down by the Zeeman slower with light at 401 nm (violet arrow) and 421 nm (blue arrow). The yellow and red arrows indicate the direction of the MOT beams for erbium (583 nm) and dysprosium (626 nm), respectively. The dark red arrow, along the *y*-axis, shows the direction of the horizontal beam of the ODT (1064 nm). In the center of the chamber the other two beams of the MOT and the vertical beam of the ODT are visible and propagate along the direction of the gravity *z*.

4.2   ODT loading

Once atoms are slowed down by the Zeeman slower, they are captured by a two-colour narrow-line MOT, which allows to reach samples with a number of atoms around 10^7 for both erbium and dysprosium[4] at a temperature of $10\,\mu$K. This temperature fixes the minimum trap depth necessary to transfer the atoms from the MOT to the ODT. The ratio between the trap depth and the thermal energy ($\hat{U}/k_B T$) has to be higher than 10 as a general rule to get an efficient loading. In our case the maximum power available for the ODT beam is

---

[4]Recently, the MOT atom number was improved up to 10^8. On the other hand, this value does not concern the measurements presented in this thesis.

around 38 W. For a single beam with $P = 38$ W (single hODT) and waist of about 20 μm, we estimate a trap depth of about 1700 μK and 1400 μK[5] for Er and Dy, respectively, which are fulfilling the general rule. When $\hat{U}/k_B T \gg 1$ the integral in Eq. (3.3) saturates and the number of atoms loaded becomes independent from the laser power. Thus, assuming to be in the saturation regime, an efficient loading of the ODT relies on the overlapped volume between MOT and ODT. This requires to increase the laser beam waist through the scanning system described in Chapter 3. Changing the trap geometry during the loading allows to reach the "mode matching" condition. "Mode matching" is referred to the ideal condition in which, after the transfer, the atomic cloud maintains his volume and temperature. The departure from the ideal case is given by a too tight trap, which heats up the atoms, or by a too loose trap, which leads to a non-adiabatic expansion of the atomic cloud [46].

In our experiment, during the MOT loading, the ODT is kept on since the atomic clouds are displaced with respect to the center of magnetic field gradient. The atoms are loaded into the hODT during the MOT compression for a time of 100 ms. During the loading an homogeneous magnetic field of about 1 G is switched on to preserve the spin polarization of the sample.

To test the effect of the scanning system on the ODT loading, the number of atoms loaded from the MOT to the ODT was measured as a function of the scanning parameter V_{gain}. The measurement is shown in Fig. 4.3. The rise of the atom number shows the clear effect of the scanning system, which leads to a number of atoms that is almost twice the value measured with the scanning off[6]. The curve reveals the limit of the current electronics, already discussed in section 3.3.2, indeed after $V_{\text{gain}} = 7$ V the atom number levels out. This measurement was taken during the test of the ODT with a waist of 35 μm with only Dy atoms. When the waist of the hODT is increased along the x-axis, the average power of the laser beam at the atoms decreases due to the reduced diffraction efficiency of the AOD for high modulation amplitude. Thus, when the volume of the ODT increases to get the maximum overlapping with the MOT volume, the power can become the limiting factor of the ODT loading.

A 35-μm waist of the hODT gives a too low axial confinement to efficiently trap the atoms. We thus rebuilt the setup to get a waist of 20.5 μm. This allows us to transfer $\approx 10^6$ atoms from the MOT to the ODT and hold them for a time sufficiently long to go on with further trap frequency measurements. In Fig. 4.4 the absorption images of the ODT shows the simultaneous loading of both species Dy (left) and Er (right).

---

[5]The details on trap depths and trap frequencies are listed in Table 2.5.

[6]The atom number is plotted in arbitrary units (a.u.) because the measurement was taken in a stage in which the imaging was not calibrated yet.
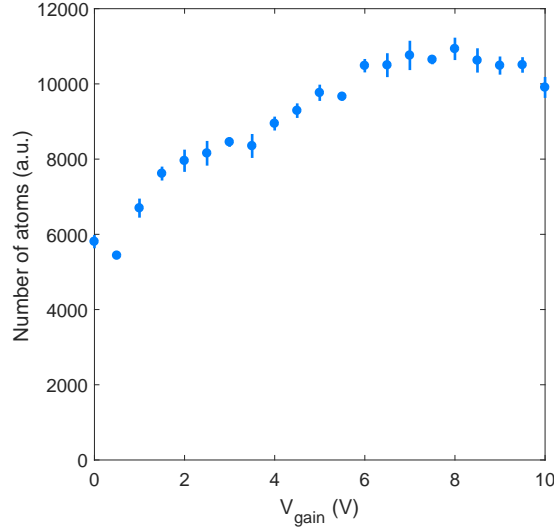
Figure 4.3 Number of atoms loaded into the optical dipole trap as a function of the scanning parameter V_{gain}. This measurement was done with the first setup of the ODT in which the beam waist was $35\,\mu\mathrm{m}$. The points show the clear influence of the scanning system on the enhancement of the atom loading. At around $V_{\mathrm{gain}} = 7\,\mathrm{V}$ the atom number levels out due to technical limits induced by the electronics, discussed in Chapter 3.

4.3 Trap frequencies measurements

An important step to characterize the geometry of the ODT is the measurement of trap frequencies. For this aim, two types of collective modes are usually excited in the atomic cloud: the monopole mode and the dipole mode. The former is referred as "breathing mode" because involves the compression and de-compression of the atomic cloud and for thermal gas has a frequency of twice the trapping frequency [22]. The latter corresponds to a translation of the total cloud and has the same frequency as the confinement.

We now briefly review how to get, using the classical Boltzmann equation, the frequency of the "breathing mode". Let's consider the trapping potential in the harmonic approximation as defined in Eq. (2.18). At low temperature, below the critical temperature T_C for Bose-Einstein condensation, the system can be described by the hydrodynamic equation of superfluidity [70]. On the other hand, when the temperature is much higher than T_C the dynamic of a dilute gas is well described by the Boltzmann equation [41]:

$$\frac{\partial f}{\partial \mathrm{t}} + \mathrm{v} \cdot \nabla_r f + \frac{F_{\mathrm{ext}}}{m} \cdot \nabla_{\mathrm{v}} f = I_{\mathrm{coll}}(f) \,, \tag{4.1}$$

where $f(r, \mathrm{v}, \mathrm{t})$ is the phase space distribution function, r and v are the position and velocity of the particles, F_{ext} is an external force acting on the particles and I_{coll} is the collisional
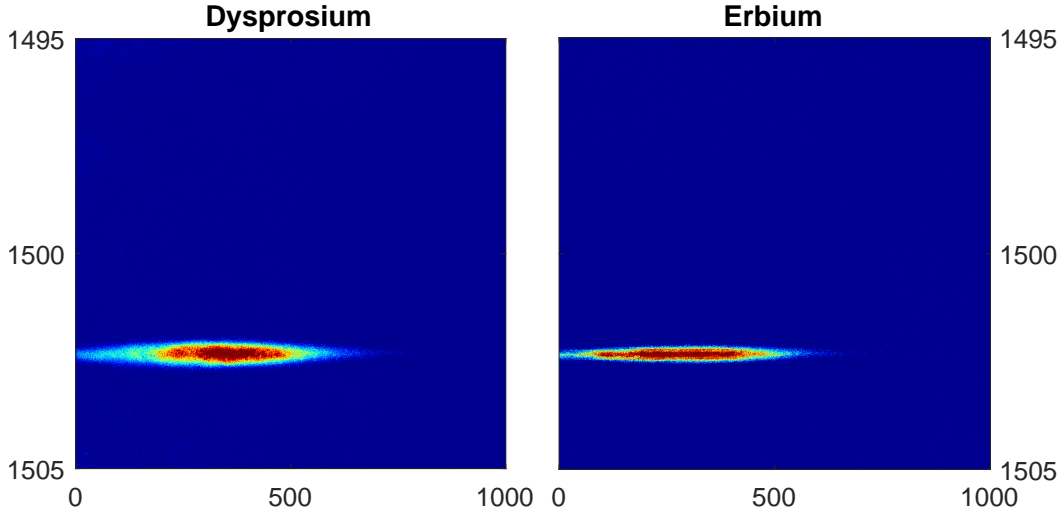
Dysprosium   **Erbium**

Figure 4.4 Simultaneous ODT loading of Er and Dy. During the MOT loading the ODT is kept on since the atomic clouds are displaced with respect to the center of magnetic field gradient. The atoms are loaded in the hODT during the MOT compression for a time of 100 ms. During the loading an homogeneous magnetic field of about 1 G is switched on to preserve the spin polarization of the sample.

integral describing the effect of collisions between particles. In our case $F_{ext} = F_{dip} = -\nabla U_{dip}$. Two regimes can be identified: the hydrodynamic (collisional) and the collisionless regime ($I_{coll} = 0$).

The behaviour of the monopole mode can be obtained applying the Boltzmann equation to the square radius of the atomic cloud [37]. Considering that $I_{coll}(\langle r^2 \rangle) = 0$ because $\langle r^2 \rangle$ is conserved during elastic collisions and assuming an isotropic harmonic potential $\omega_x = \omega_y = \omega_z \equiv \omega_{trap}$, the equation assumes the form:

$$\frac{d\langle r^2 \rangle}{dt} = 2 \langle r \cdot v \rangle. \tag{4.2}$$

Equation (4.2), together with the following two equations:

$$\frac{d\langle r \cdot v \rangle}{dt} = \langle v^2 \rangle - \omega_{trap}^2 \langle r^2 \rangle, \qquad \frac{d\langle v^2 \rangle}{dt} = \omega_{trap}^2 \langle r^2 \rangle,$$

lead to the solution $\omega_m = 2\omega_{trap}$. In the case of a Bose-Einstein condensate at $T = 0$ also the mean field interaction has to be included, thus the solution reads $\omega_m = \sqrt{5}\omega_{trap}$.

There are several methods to determine the trap frequencies, which are based either on parametric heating or on direct observation of the atomic cloud oscillations in the trap. The oscillations are induced by a change of the trap frequencies, e. g. obtained by power variation of the laser beam, a change of the beam waist or applying a magnetic field gradient.

In the parametric heating method, the intensity of the dipole trap beam is modulated forcing the atoms to oscillate. If the modulation is twice the frequency of the confinement, atoms are parametrically excited and are lost. Thus, looking at the number of atoms as a function of the modulation frequency, the position of the resonance corresponds to the measured trap frequency.

Experimental procedure   In our experiment, we measured the trap frequencies by looking at the atoms oscillations. In particular the monopole mode can be excited by suddenly changing the confinement, for example reducing or increasing the power of the laser beam or changing the aspect ratio of the ODT through the scanning system.

The dipole mode, which involves the center of mass oscillation and it does not depend on the temperature of the gas, can be excited by a displacement, in a controlled way, of the cloud from the central position of the trap. The scanning system provides a tool to probe this mode along the horizontal direction (x) changing the radio-frequency that controls the AOD, which corresponds to the scanning parameter V_{offset}.

In the measurement presented in this section, we look at the monopole mode measuring the width of the atomic cloud along the gravity axis z. The isotopes involved in this measurement are ^{168}Er and ^{162}Dy. We load approximately 10^6 atoms of both species from the MOT into the single hODT beam in 100 ms, as explained in the previous section[7]. The hODT laser beam has a power of $P = 37\,\mathrm{W}$[8] and waist $w_x = w_z = 20.5\,\mu\mathrm{m}$. After the loading, we switch off the optical dipole trap for $100\,\mu\mathrm{s}$[9] and switch it on again. The absence of the trap leads to a ballistic expansion of the atomic cloud. When the trapping is restored the atoms are recaptured and they gain potential energy, which is converted into kinetic energy through the oscillation of the radial size of the cloud. The atoms are then held to register the oscillations. The imaging beam hits the atomic cloud at an angle of 45° with respect to the propagation axis of the laser beam (y), in the $x - y$ plane. Due to this reason an oscillation along the x or y direction would not be easily distinguished and the stronger frequency along the x-axis would dominate on the other. This influenced our choice to look at the z-axis. The implementation of an high resolution imaging is planned to image the atomic clouds from the top of the main chamber, along the z direction. Figure 4.5 shows the trap frequency measurements for Er (top) and Dy (bottom). The data points are the measured widths along z, while the orange curve is the fit.

---

[7]The scanning parameter V_{gain} was set to $V_{gain} = 2\,\mathrm{V}$.

[8]Power measured with the thermal power sensor *Thorlabs S322C*, which has a measurements uncertainty of 3% at 1064 nm.

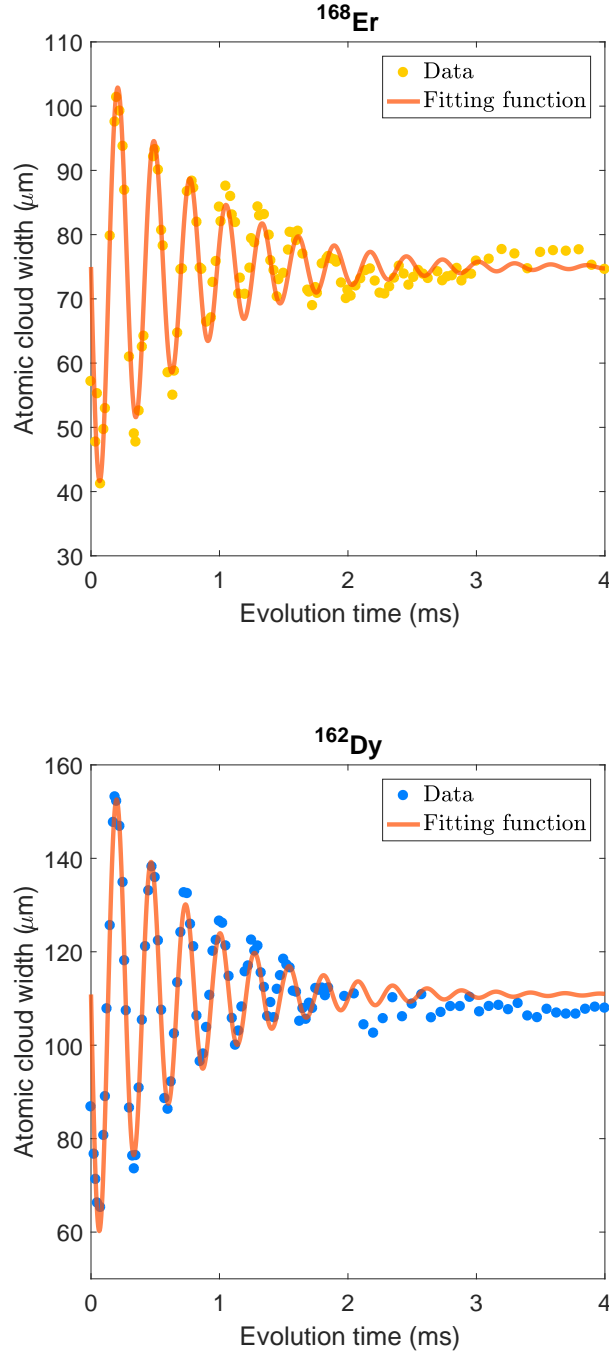[9]This time is usually chosen equal to a fraction of the oscillation period of the atoms in the trap.

Figure 4.5 Trap frequency measurements for Er (top) and Dy (bottom). In this measurement the monopole mode is excited. After the loading, the optical dipole trap is switched off for 100 μs and switched on again to excite the monopole mode. The atoms are then held to register the oscillations, measuring the width of the atomic cloud along the gravity axis z. The widths are fitted by the function $w_{\text{fit}}(t) = Ae^{-\gamma t}\sin(2\pi\nu_{\text{m}}t) + B$. The trapping frequencies are estimated by $\nu_z = \nu_{\text{m}}/2$.

The widths are fitted by an exponentially dumped sine function

$$w_{\mathrm{fit}}(t) = Ae^{-\gamma t}\sin(2\pi\nu_{\mathrm{m}}t) + B, \tag{4.3}$$

where A is the initial amplitude, γ is the decay rate, ν_{m} is the frequency of the mode, t is the evolution time of the oscillation and B is an offset constant.

Table 4.1 Results from the fitting of the width of the atomic cloud with the function $w_{\mathrm{fit}}(t) = Ae^{-\gamma t}\sin(2\pi\nu_{\mathrm{m}}t) + B$. A is the initial amplitude, γ is the decay rate, ν_{m} is the frequency of the mode, t is the evolution time of the oscillation and B is an offset constant. The final trap frequency is given by $\nu_z = \nu_{\mathrm{m}}/2$.

Fit parameters	^{168}Er	^{162}Dy
A (μm)	-36 ± 3	-55 ± 4
γ (ms^{-1})	1.3 ± 0.2	1.4 ± 0.2
ν_{m} (kHz)	3.56 ± 0.02	3.72 ± 0.02
B (μm)	75.0 ± 0.6	110.9 ± 0.8

Table 4.1 shows the results of the fit. The trap frequency along the z axis is obtained by $\nu_z = \nu_{\mathrm{m}}/2$. This leads to the following values:

$$\nu_z = (1.78 \pm 0.01)\,\mathrm{kHz} \qquad \text{for Er}$$
$$\nu_z = (1.86 \pm 0.01)\,\mathrm{kHz} \qquad \text{for Dy}$$

Considering for the polarizability the theoretical values of $\mathrm{Re}\{\alpha\} = 173$ a.u. [12] and $\mathrm{Re}\{\alpha\} = 164$ a.u. [54] for Er and Dy, respectively, and a pure Gaussian beam, we expect trap frequencies of $\nu_z \approx 5.1$ kHz. Our results are about 65% (Er) and 63% (Dy) smaller than the predicted values. The strong deviation could be induced by several reasons. A wrong estimation of the beam waist and astigmatism are two possible reasons. On the other hand, to explain such discrepancy, the beam waist would have to be 70% larger than the measured one[10]. Whereas, the same discrepancy would be explained by an astigmatism of ≈ 10 mm. Reflecting out the beam before the last mirror used to send the hODT light on the atoms, we investigated the beam shape using the CCD-camera beam profiler. The profile exhibited a larger astigmatism with respect to the one mentioned in Chapter 3, which is comparable to the theoretical value needed to get the strong reduction of trap frequencies. The damping of the oscillation is caused by the anharmonicity of the confining potential.

The knowledge of trap frequencies is crucial not only to define the geometry of the trap seen by the atoms, but also to extract the experimental value of the polarizability. Applying

---

[10]Section 3.3.3 shows the measurement of the beam waist for the hODT and vODT.

Eq. (2.27) to the z-axis, the polarizability can be obtained for each specie measuring waist and trap frequencies. The expression, written in atomic units, reads:

$$\text{Re}\{\alpha\} = \frac{m\pi\varepsilon_0 c}{4PK} w_z^3 w_x \omega_z^2 , \tag{4.4}$$

where $K = 1.6488 \times 10^{-41}$ and $\omega_z = 2\pi\nu_z$.

In our case, the absolute values are not reliable because affected by large systematic errors resulting from the astigmatism of the laser beam. On the other hand, this effect concern both species. Thus, the polarizability ratio can be estimated.

In the evaluation of the polarizability ratio the only quantities that survive are the mass ratio and the measured trap frequencies:

$$R \equiv \frac{\text{Re}\{\alpha\}^{\text{Dy}}}{\text{Re}\{\alpha\}^{\text{Er}}} = \frac{m^{\text{Dy}}(\nu_z^{\text{Dy}})^2}{m^{\text{Er}}(\nu_z^{\text{Er}})^2} , \tag{4.5}$$

from which the experimental result reads $R_{\text{Exp.}} = 1.05 \pm 0.02$. Since all the measurements are taken in the same apparatus under the same conditions of the dipole beam, e. g. power, waist and astigmatism, the systematic errors cancel out and the uncertainty is dominated by statistical errors. The predicted polarizability ratio, calculated considering the theoretical values mentioned before, results $R_{\text{Theory}} = 0.95$. In contrast to the theoretical prediction we measure a higher polarizability for Dy with respect to Er. So far, the measurements on the atomic polarizability of Dy manifest large discrepancy from each other ($\text{Re}\{\alpha\} = 116 \, \text{a.u.}$, $\text{Re}\{\alpha\} = 136 \, \text{a.u.}$) and with the theoretical value ($\text{Re}\{\alpha\} = 164 \, \text{a.u.}$). On the other hand, the experimental value measured by the Erbium lab in Innsbruck ($\text{Re}\{\alpha\}^{\text{Er}} = 166 \pm 3_{\text{st}} \pm 61_{\text{sys}} \, \text{a.u.}$ [12]), results in agreement with the predicted one. Taking this value as a reference, from Eq. (4.5) the polarizability of Dy reads $\text{Re}\{\alpha\}^{\text{Dy}} = 175 \pm 4_{\text{st}} \pm 64_{\text{sys}} \, \text{a.u.}$. Thus, we expect for the atomic polarizability of Dy, once correcting the astigmatism, a measured value close to this estimation.

4.4 Towards evaportive cooling

The evaporative cooling is the last step to produce a degenerate quantum gas. Above the critical temperature for the degenerate regime, atoms in the phase space follow the Maxwell-Boltzmann (MB) energy distribution:

$$n(E) = n_0 e^{-\frac{E}{k_B T_1}} , \tag{4.6}$$

where n_0 is the peak atom density and T_1 is the temperature of the atomic cloud. The concept of evaporation is already well know in everyday life and relies on the leaving of more energetic particles from a system with a binding energy. Since the exponential distribution extends to infinity, there is always a finite probability to find particles with high energy that leave the system. Thus, this process happens spontaneously in nature and becomes more and more slow as the energy is carried away and the system cools down, unless further evaporation is forced modifying the system from the outside, in such a way that also the particles with lower energy escape from the system.

Defining $E_t = k_B T_1 \eta$, where η usually assumes values in the range $3 - 6$ [30], let's cut the MB distribution at the energy E_t. The truncated distribution has in total less energy per atom thus, after the rethermalization, the new one is characterized by a lower temperature T_2. Without any energy exchange between atoms the resulting distribution would be just cut and the process would be a selection of the coldest atoms rather than a cooling. The same would happen for a too fast evaporation, in which atoms do not have the time to collide. Thus, the efficiency of the evaporative cooling relies on the elastic collision rate Γ_{el} given, for a 3D harmonic trap, by Eq. (3.4). Considering the expression of the mean thermal velocity $\bar{v} = 4\sqrt{k_B T / \pi m}$ and the total elastic cross section $\sigma = 8\pi a^2$, Γ_{el} reads

$$\Gamma_{el} = \frac{n_0 8\pi a^2}{2\sqrt{2}} 4\sqrt{\frac{k_B T}{\pi m}} . \tag{4.7}$$

For a thermal cloud, once the atom number, trap frequencies and temperature are known, the particle density n_0 can be written as

$$n_0 = N\bar{\omega}^3 \left(\frac{m}{2\pi k_B T} \right)^{\frac{3}{2}} , \tag{4.8}$$

where $\bar{\omega} = (\omega_x \omega_y \omega_z)^{1/3}$ is the average trap frequency. The s-wave scattering length, which determines Γ_{el} and thus fixes the time scale of the evaporation, assumes different values for each Er and Dy isotope. Table 4.2 shows a list of s-wave scattering lengths for two bosonic isotopes of Er and Dy.

In a gas mixture, during the rethermalization, the average energy transferred per each collision is [25]

$$\Delta E_{1-2} = k_B \Delta T \zeta ,$$

where $\Delta T = T_2 - T_1$ is the temperature difference between the components and $\zeta = \frac{4m_1 m_2}{(m_1 + m_2)^2}$. For an Er-Dy mixture, in which atoms have almost the same mass, approximately 3 elastic

Table 4.2 List of s-wave scattering lengths for two bosonic isotopes of Er and Dy. a is usually expressed in terms of the Bohr radius a_0.

Erbium		Dysprosium	
Isotope	a	Isotope	a
^{166}Er	$72(13)\,a_0$ [31]	^{162}Dy	$112(10)\,a_0$ [82]
^{168}Er	$200(23)\,a_0$ [31]	^{164}Dy	$92(8)\,a_0$ [82], $91(15)\,a_0$ [59]

collisions per atom are needed for the thermalization and the stabilization of the new MB distribution [62].

In optical dipole traps the evaporation consists of lowering the trapping potential by reducing the power of the laser beam in several steps. The process can be iterated up to the degenerate regime. At each point all the atoms with an energy greater than the cutoff energy will escape from the trap and the remaining ones rethermalize leading to an overall lower temperature of the sample. The cutoff energy of each step has to be chosen with high care to reach the degenerate regime in an efficient way.

The quantity to keep track of, during the evaporation for the achievement of a BEC, is the phase space density (PSD). Atoms in a gas can be seen as wavepackets with an extension given by the deBroglie wavelength

$$\lambda_{\mathrm{dB}} = \sqrt{\frac{2\pi\hbar^2}{mk_BT}}\,, \tag{4.9}$$

where m and T are the mass and the temperature of the atoms, respectively. For lower temperatures λ_{dB} increases. When the temperature is such that the extension of the particles is comparable to the mean particle distance defined by $n_0^{-1/3}$, a phase transition to the Bose-Einstein condensation takes place. The quantity that relates the mean particle distance to λ_{dB} is the PSD, defined as

$$\mathrm{PSD} = n_0\lambda_{\mathrm{dB}}^3\,, \tag{4.10}$$

which, at the transition point, assumes the value $\mathrm{PSD} \approx 2.6$ [70].

During the experiment, the evaporation is usually interrupted at several points to check atom numbers, temperatures and trap frequencies in order to evaluate the PSD. The overall efficiency of the evaporative process is summarized in the quantity [45]

$$\gamma = -\frac{d(\ln\mathrm{PSD})}{d(\ln N)}\,, \tag{4.11}$$

which is a measure of the orders of magnitude gained in the PSD at the cost of atom number.

Find the right parameters, as the rate of each step at which the trap depth is reduced, is not straightforward. As a starting point we can take advantage of the knowledge on the optimized evaporation scheme used for erbium [31]. Our trap geometry is given by the waists of the hODT and vODT, whose values are $w_x^h = w_z^h = 20.5\,\mu\text{m}$ and $w_x^v = 101.3\,\mu\text{m}$, $w_y^v = 95.0\,\mu\text{m}$, respectively. The maximum available power is $\approx 38\,\text{W}$, which can be distributed between hODT and vODT through a waveplate, as shown in Fig. 3.15. The polarizability values considered for the simulation of the evaporative steps are the experimental ones $\text{Re}\{\alpha\} = 136\,\text{a.u.}$ [60] and $\text{Re}\{\alpha\} = 166\,\text{a.u.}$ [12] for Dy and Er, respectively.

Figure 4.6 shows the simulations of the evaporation ramps for Er and Dy. The power of the hODT and vODT together with the AR is changed in order to reproduce the trap frequency settings used in the Erbium lab (Innsbruck) to get the degenerate phase.

Particular attention was dedicated to the frequency along the y-axis, where the confinement of the trap is weaker and the atoms can spread during the evaporation. This frequency, which in the Erbium setting for the crossed ODT configuration was around $100\,\text{Hz}$, is mainly given by the vertical beam of the ODT. The latter plays an important role during the evaporation, leading to a sudden increase of the PSD when switched on [6]. The process should start with a large AR, to match the ODT volume with the MOT volume, and high power, to provide a trap sufficiently deep to get the saturation regime. After the loading, the power is quickly ($\approx 50\,\text{ms}$) reduced to start the "exponentially-like" ramp and the AR is reduced as well, in such a way to increase the strength of the confinement and compress the atomic cloud. In the central steps of the evaporation the vODT is switched on to confine the atoms that try to spread along the propagation axis of the hODT beam (y-axis). The last steps are crucial and the power of the hODT and vODT and the AR as well are chosen in such a way to optimize the ratio between elastic and inelastic collisions. The AR, at this stage of the evaporation, is usually increased to reduce three-body recombinations. As discussed in the previous section, the atomic polarizability of Dy shows great discrepancy among the values measured by other groups and the theoretical one. This, of course, strongly affect the resulting trap depths and trap frequencies. Figure 4.7 shows trap depths and average trap frequency during the evaporation ramps, calculated choosing different values of the polarizability $\text{Re}\{\alpha\} = (136,\ 116,\ 164)\,\text{a.u.}$, already mentioned in Chapter 2.

An interesting feature of dipolar gases concerns the evaporative cooling of fermions. The key factors for the evaporation are the elastic collisions needed for the thermalization. Due to this reason, forced evaporative cooling to achieve the quantum degeneracy of identical fermions has been a challenge for many years with respect to the BEC, since the Fermi-Dirac statistics forbid s-wave collisions between spin-polarized identical fermions. Indeed, the
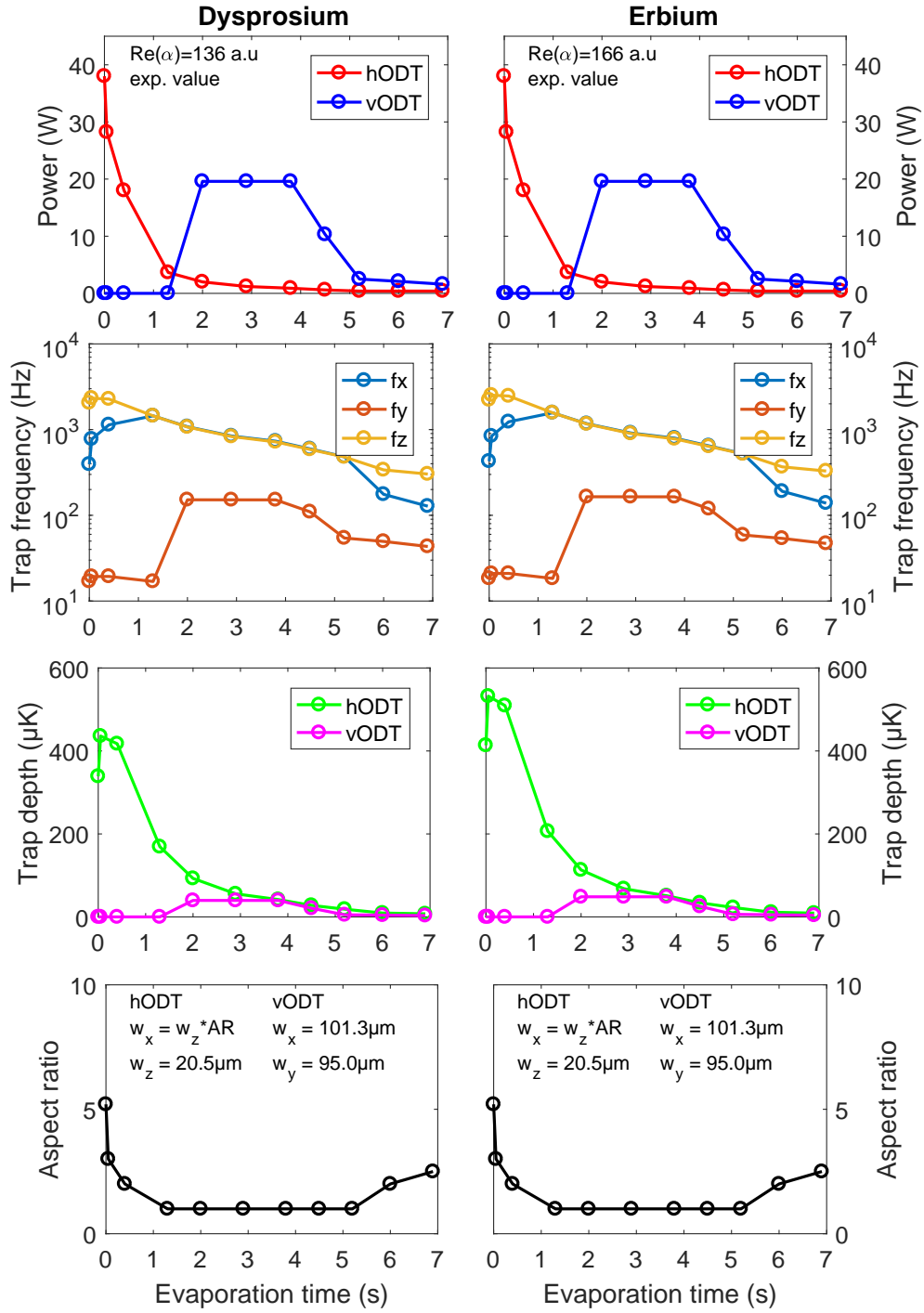
Figure 4.6 Evaporation ramp simulated for Er and Dy. The power of the hODT and vODT together with the AR is changed in order to reproduce the trap frequency settings used in the Erbium lab (Innsbruck) to get the degenerate phase.
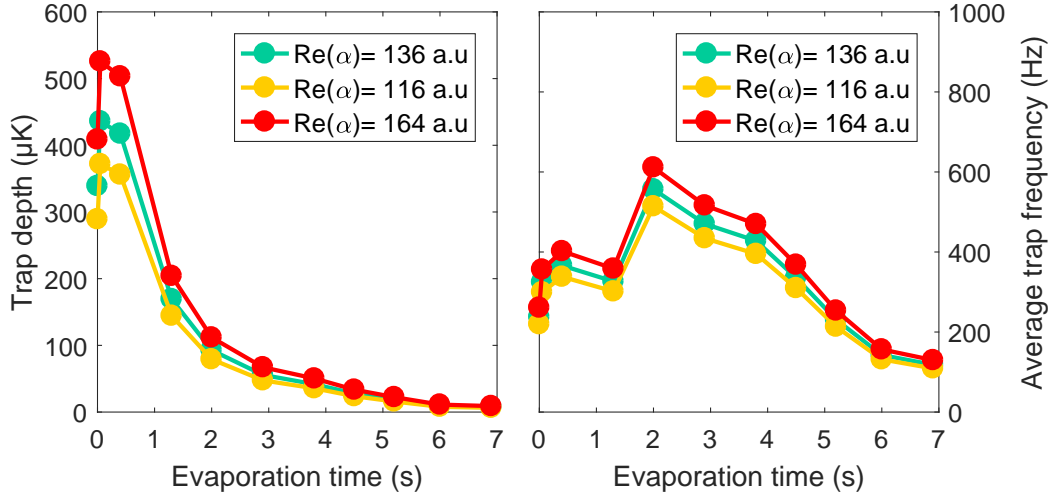
Figure 4.7 Simulations of trap depths and averaged trap frequency for Dy atoms, considering the same settings of power and AR of Fig. 4.6.

total wave function for two identical fermions has to be antisymmetric for particle exchange. At the low temperatures of interest for ultracold physics to reach the degenerate Fermi gas the collisions are primarily s-wave. Several techniques have been adopted to overcome this limit, by sympathetic cooling between fermionic and bosonic species [57, 62] or trapping two different spin states [26]. Provided that these mixtures have to be stable against inelastic collisions.

At temperature lower than $10\,\mu\text{K} - 100\,\mu\text{K}$ when, in the only presence of contact interaction, the total elastic cross section for identical fermions would be zero because containing only s-wave contributions, the scaling as r^{-3} of the DDI prevents the cross section from vanishing. Thus, identical dipolar fermions can collide in the limit of low temperature, making possible the production of a single component degenerate Fermi gas with direct evaporate cooling [2].

Conclusion and outlook

The aim of my master thesis was to design and realize an optical dipole trap for the RARE experiment in Innsbruck, enabling us to simultaneously confine ultracold Er and Dy atoms.

The working principle of the dipole trap relies on the atom-light interaction properties. Erbium and dysprosium are both rare-earth metals with a multi-valence electrons character. This gives rise to a complex and rich energy spectrum. The first task was to simulate the trapping potential for the atoms with a determination of the most important parameters for an efficient confinement of both species, e. g. trap depth and trap frequencies. A fundamental role is played by the atomic polarizability which, due to the anisotropic character of the electronic distribution around the core, for Er and Dy manifest a tensorial nature. Estimating the atomic polarizability is a non-trivial task with lanthanides. Indeed, the experimental values are usually affected by systematic errors induced by the uncertainty on the waist. Moreover, the complex spectrum makes the theoretical determination challenging.

The second part of my thesis was dedicated to the experimental realization of the optical dipole trap with a tunable geometry. The tunability is a fundamental tool to increase the loading efficiency of the optical dipole trap, reaching the "mode-matching" condition with the magneto-optical trap. In this condition the atomic cloud maintains its volume and temperature during the transfer. Additionally, it can be used to optimize the efficiency of the evaporative cooling, which is determined by the elastic collision rate, by tuning the cloud density. Finally, a tunable trap behaves as an additional experimental parameter to manipulate inter-atomic interactions due to the anisotropic character of the dipole-dipole interactions. Several systems were tested to find the most suited for our experiment. These include also a mechanical system consisting of five cylindrical lenses and a translational stage. The tests led us to a setup based on time-averaged potentials created by an acousto-optic deflector. This device deflects the laser beam horizontally according to a certain shape of the driving RF signal. In contrast to an acousto-optic modulator, two RF inputs, with a given delay in phase with respect to each other, overlap in such a way that the resultant signal compensates for the deviation from the Bragg angle condition, allowing a diffraction efficiency almost uniform over a broad range of deflection angles. If the beam deflection is modulated on a timescale

much faster than the atomic oscillation, the atoms behave as in a smooth time-averaged potential. Several trap geometries can be realized by modifying the shape and parameters of the driving RF signal. The ultimate limitations of the setup are mostly due to the VCO that controls the deflector, in particular its limited frequency bandwidth. Indeed, in a region in which the limited bandwidth does not play a role, the maximum aspect ratio (AR) was measured to be AR $\approx$ 11. In contrast, by increasing the modulation to enter the time-averaged potential regime, the AR is reduced to AR $\approx$ 7.

Finally, we describe the integration of the optical setup into the main experiment, and a preliminary characterization of the optical dipole trap. If we denote by x the direction of the atomic beam and by z the axis of gravity, the ODT has a 90°-crossed configuration, created by splitting in two paths the laser beam coming from a 50 W Yb^{3+} fiber laser with a wavelength of 1064 nm. One beam, referred in the text as horizontal beam (hODT), is involved in the creation of the time-averaged potential and propagates along the y direction. The vertical beam (vODT) crosses the hODT and propagates along the z direction. A first test of the hODT was performed with a beam waist of 35 μm on the atoms. In this case, the scanning played an important role in the ODT loading, increasing the atom number by almost a factor of two. However, the weak y-confinement provided by the hODT let the atoms spread along the direction of propagation, preventing accurate trap frequency measurements and further evaporative steps. Reducing the radial waist to $w_x = w_z = 20.5$ μm allowed us to proceed with trap frequency measurements, from which we deduced an efficient loading of $\approx 10^6$ atoms for both species, enabling us to extract the value of the atomic polarizabilities. Probing the breathing mode along the gravity axis, we measured trap frequencies of $^{Er}v_z = 1.78(1)$ kHz and $^{Dy}v_z = 1.86(1)$ kHz, for Er and Dy respectively. The results show great discrepancy from the predicted values, which is probably due to an astigmatism of the laser beam. So far, there have been large discrepancy between polarizability measurements of different groups with dysprosium. For our latest measurements, the absolute values of the polarizablities are not reliable since affected by systematic errors induced by the astigmatism. This request to be corrected in future and leaves room for improvement of our laser source. Independent of this, our experiment enables us to determine the polarizability ratio of Er and Dy, for which the systematic errors cancel out, offering a better understanding of their atomic properties. The beam waist of the vertical beam was chosen to be $w_x = 101.3$ μm and $w_y = 95.0$ μm. The astigmatism does not affect the vODT, for which the distance of the foci is much smaller than the Rayleigh length. The vertical beam plays an important role in the evaporative cooling "closing the door" to the atoms along the weak longitudinal confinement of the hODT.

The RARE experiment plans to combine Er and Dy in a three-chamber apparatus. Atoms will be moved from one chamber to the others by optical transport, which needs to be able to

cover a total distance of around 70 cm. During my thesis I was also involved in the planning of the transport setup. A first test was conducted with focus-tunable lenses which revealed to be not suited for our case. Therefore, the setup will involve the use of a translational stage. Appendix B shows some preliminary consideration of the transport.

Bibliography

[1] P. Ahmadi, B. P. Timmons, and G. S. Summy. Geometrical effects in the loading of an optical atom trap. *Physical Review A - Atomic, Molecular, and Optical Physics*, 72, 2005.

[2] K. Aikawa, A. Frisch, M. Mark, S. Baier, R. Grimm, and F. Ferlaino. Reaching Fermi degeneracy via universal dipolar scattering. *Physical Review Letters*, 112(1), 2014.

[3] K. Aikawa, A. Frisch, M. Mark, S. Baier, A. Rietzler, R. Grimm, and F. Ferlaino. Bose-Einstein condensation of erbium. *Physical Review Letters*, 108, 2012.

[4] AnalogDevices. *Data sheet: AD734*, 2011.

[5] M. H. Anderson, J. R. Ensher, M. R. Matthews, C. E. Wieman, and E. A. Cornell. Observation of Bose-Einstein Condensation in a Dilute Atomic Vapor. *Science*, 269:198–201, 1995.

[6] Simon Baier. *An optical dipole trap for Erbium with tunable geometry*. Master's thesis, Faculty of Mathematics, Computer Science and Physics; University of Innsbruck, 2012.

[7] Waseem S. Bakr, Jonathon I. Gillen, Amy Peng, Simon Fölling, and Markus Greiner. A quantum gas microscope for detecting single atoms in a Hubbard-regime optical lattice. *Nature*, 462(7269):74–77, 2009.

[8] H Y Ban, M Jacka, J L Hanssen, J Reader, J J McClelland, C Y Chen, Y M Li, K Bailey, W R Anderson, and C C Bradley. Laser cooling transitions in atomic erbium. *J. Phys. D – Appl. Phys*, 36:335–385, 2000.

[9] M. A. Baranov, M. Dalmonte, G. Pupillo, and P. Zoller. Condensed matter theory of dipolar quantum gases. *Chemical Reviews*, 112:5012–5061, 2012.

[10] M. D. Barrett, J. A. Sauer, and M. S. Chapman. All-Optical Formation of an Atomic Bose-Einstein Condensate. *Physical Review Letters*, 87:010404, 2001.

[11] Michael Bass and Walter Koechner. *Solid-State Lasers : A Graduate Text*. Springer, 2003.

[12] J. H. Becher, S. Baier, K. Aikawa, M. Lepers, J.-F. Wyart, O. Dulieu, and F. Ferlaino. *in preparation*, 2017.

[13] Thomas A. Bell, Jake A.P. Glidden, Leif Humbert, Michael W.J. Bromley, Simon A. Haine, Matthew J. Davis, Tyler W. Neely, Mark A. Baker, and Halina Rubinsztein-Dunlop. Bose-Einstein condensation in large time-averaged optical ring potentials. *New Journal of Physics*, 18, 2016.

[14] B. J. Bloom, T. L. Nicholson, J. R. Williams, S. L. Campbell, M. Bishof, X. Zhang, W. Zhang, S. L. Bromley, and J. Ye. An optical lattice clock with accuracy and stability at the 10^{-18} level . *Nature*, 506:71–75, 2014.

[15] Bose. Plancks gesetz und lichtquantenhypothese. *Zeitschrift für Physik*, 26(1):178–181, Dec 1924.

[16] Antoine Browaeys, Daniel Barredo, and Thierry Lahaye. Experimental investigations of dipole–dipole interactions between a few Rydberg atoms. *Journal of Physics B: Atomic, Molecular and Optical Physics*, 49(15):152001, 2016.

[17] E. Burt, R. Ghrist, C. Myatt, M. Holland, E. Cornell, and C. Wieman. Coherence, Correlations, and Collisions: What One Learns about Bose-Einstein Condensates from Their Decay. *Physical Review Letters*, 79:337–340, 1997.

[18] W C. Martin, Romuald Zalubas, and Lucy Hagan. *Atomic energy levels: The rare earth elements (the spectra of lanthanum, cerium, praseodymium, neodymium, promethium, samarium, europium, gadolinium, terbium, dysprosium, holmium, ebrium, thulium, ytterbium, and lutetium)*. Tech. report. National Bureau of Standards, U.S. Department of Commerce, 1978.

[19] Cheng Chin, Rudolf Grimm, Paul Julienne, and Eite Tiesinga. Feshbach resonances in ultracold gases. *Reviews of Modern Physics*, 82:1225–1286, 2010.

[20] L. Chomaz, S. Baier, D. Petter, M. J. Mark, F. Wächtler, L. Santos, and F. Ferlaino. Quantum-Fluctuation-driven crossover from a dilute Bose-Einstein condensate to a macrodroplet in a dipolar quantum fluid. *Physical Review X*, 6, 2016.

[21] Lauriane Chomaz, Rick M. W. van Bijnen, Daniel Petter, Giulia Faraoni, Simon Baier, Jan Hendrik Becher, Manfred J. Mark, Falk Waechtler, Luis Santos, and Francesca Ferlaino. Observation of the Roton Mode in a Dipolar Quantum Gas. *arXiv:1705.06914*, 2017.

[22] Claude Cohen-Tannoudji and David Guéry-Odelin. *Advances in Atomic Physics: An Overview*. World Scientific Publishing Company, 2011.

[23] A. Couvert, T. Kawalec, G. Reinaudi, and D. Guéry-Odelin. Optimal transport of ultracold atoms in the non-adiabatic regime. *EPL (Europhysics Letters)*, 83:13001, 2008.

[24] K. B. Davis, M. O. Mewes, M. R. Andrews, N. J. Van Druten, D. S. Durfee, D. M. Kurn, and W. Ketterle. Bose-Einstein condensation in a gas of sodium atoms. *Physical Review Letters*, 75:3969–3973, 1995.

[25] G. Delannoy, S. Murdoch, V. Boyer, V. Josse, P. Bouyer, and A. Aspect. Understanding the production of dual Bose-Einstein condensation with sympathetic cooling. *Physical Review A*, 63(5):051602, 2001.

[26] B. DeMarco. Onset of Fermi Degeneracy in a Trapped Atomic Gas. *Science*, 285:1703–1706, 1999.

[27] Albert Einstein. Quantentheorie des einatomigen idealen Gases. *Sitzungsberichte der Preuss. Akad. der Wissenschaften*, 1:1–5, 1925.

[28] Igor Ferrier-Barbut, Holger Kadau, Matthias Schmitt, Matthias Wenzel, and Tilman Pfau. Observation of Quantum Droplets in a Strongly Dipolar Bose Gas. *Physical Review Letters*, 116, 2016.

[29] Richard P. Feynman. Simulating physics with computers. *International Journal of Theoretical Physics*, 21:467–488, 1982.

[30] Christopher J Foot. *Atomic Physics*. Oxford University Press, U.S.A., 2005.

[31] Albert Frisch. *Dipolar Quantum Gases of Erbium*. PhD thesis, Faculty of Mathematics, Computer Science and Physics; University of Innsbruck, 2014.

[32] Thomas F. Gallagher. *Rydberg atoms*. Cambridge University Press, 1994.

[33] Alexander L. Gaunt, Tobias F. Schmidutz, Igor Gotlibovych, Robert P. Smith, and Zoran Hadzibabic. Bose-einstein condensation of atoms in a uniform potential. *Physical Review Letters*, 110, 2013.

[34] Axel Griesmaier, Jörg Werner, Sven Hensler, Jürgen Stuhler, and Tilman Pfau. Bose-Einstein condensation of chromium. *Physical Review Letters*, 94, 2005.

[35] Rudolf Grimm. Optical Dipole Traps for Neutral Atoms. *Advances in Atomic, Molecular and Optical Physics*, 42:95–170, 2000.

[36] Guenther Gsaller. Visualizing Atomic Orbitals. *Wolfram Demonstrations Project*, 2007.

[37] D. Guery-Odelin, F. Zambelli, J. Dalibard, and S. Stringari. Collective oscillations of a classical gas confined in harmonic traps. *Physical Review A - Atomic, Molecular, and Optical Physics*, 60(6):6, 1999.

[38] T. L. Gustavson, A. P. Chikkatur, A. E. Leanhardt, A. Görlitz, S. Gupta, D. E. Pritchard, and W. Ketterle. Transport of Bose-Einstein condensates with optical tweezers. *Physical Review Letters*, 88:204011–204014, 2002.

[39] Wenjun He, Yuegang Fu, Yang Zheng, Lei Zhang, Jiake Wang, Zhiying Liu, and Jianping Zheng. Polarization properties of a corner-cube retroreflector with three-dimensional polarization ray-tracing calculus. 52:4527–4535, 07 2013.

[40] Myoung-Sun Heo, Tout T. Wang, Caleb A. Christensen, Timur M. Rvachov, Dylan A. Cotta, Jae-Hoon Choi, Ye-Ryoung Lee, and Wolfgang Ketterle. Formation of ultracold fermionic NaLi feshbach molecules. *Phys. Rev. A*, 86:021602, Aug 2012.

[41] Kerson Huang. *Statistical Mechanics, 2nd Edition*. John Wiley & Sons, 1987.

[42] Isomet. *AN1022: All About Bragg Angle Errors in AO Modulators and Deflectors*, 2007.

[43] Jens Jensen and A.R. Mackintosh. *Rare earth magnetism: structures and excitations.* Clarendon Press Oxford.

[44] S. L. Kemp, K. L. Butler, R. Freytag, S. A. Hopkins, E. A. Hinds, M. R. Tarbutt, and S. L. Cornish. Production and characterization of a dual species magneto-optical trap of cesium and ytterbium. *Review of Scientific Instruments*, 87, 2016.

[45] W. Ketterle and N.J. Van Druten. Evaporative Cooling of Trapped Atoms. *Advances In Atomic, Molecular, and Optical Physics*, 37(C):181–236, 1996.

[46] W. Ketterle, D.S. Durfee, and D.M. Stamper-Kurn. Making, probing and understanding Bose-Einstein condensates. In *Bose-Einstein Condensation in Atomic Gases, International School of Physics Enrico Fermi*. Società Italiana di Fisica Bologna, Italy, 1998.

[47] T. Koch, T. Lahaye, J. Metz, B. Fröhlich, A. Griesmaier, and T. Pfau. Stabilization of a purely dipolar quantum gas against collapse. *Nature Physics*, 4:218–222, 2008.

[48] Christoph Kohstall. *A New Toolbox for Experiments with Ultracold ^6Li.* Diploma's thesis, Faculty of Mathematics, Computer Science and Physics; University of Innsbruck, 2007.

[49] Svetlana Kotochigova. Controlling interactions between highly magnetic atoms with Feshbach resonances. *Reports on Progress in Physics*, 77:093901, 2014.

[50] S. Kuhr, W. Alt, D. Schrader, M. Müller, V. Gomer, and D. Meschede. Deterministic Delivery of a Single Atom. *Science*, 293:278–280, 2001.

[51] T Lahaye, C Menotti, L Santos, M Lewenstein, and T Pfau. The physics of dipolar bosonic quantum gases. *Reports on Progress in Physics*, 72:126401, 2009.

[52] Julian Leonard, Moonjoo Lee, Andrea Morales, Thomas M. Karg, Tilman Esslinger, and Tobias Donner. Optical transport and manipulation of an ultracold atomic cloud using focus−tunable lenses. *New Journal of Physics*, 16, 2014.

[53] M. Lepers, J. F. Wyart, and O. Dulieu. Anisotropic optical trapping of ultracold erbium atoms. *Physical Review A - Atomic, Molecular, and Optical Physics*, 89, 2014.

[54] H Li, J-F Wyart, O Dulieu, S Nascimbène, and M Lepers. Optical trapping of ultracold dysprosium atoms: transition probabilities, dynamic dipole polarizabilities and van der Waals C_6 coefficients. *Journal of Physics B: Atomic, Molecular and Optical Physics*, 50:014005, 2017.

[55] Rianne S. Lous, Isabella Fritsche, Michael Jag, Bo Huang, and Rudolf Grimm. Thermometry of a deeply degenerate fermi gas with a Bose-Einstein condensate. *Phys. Rev. A*, 95:053627, May 2017.

[56] Robert Löw, Hendrik Weimer, Johannes Nipper, Jonathan B. Balewski, Björn Butcher, Hans Peter Büchler, and Tilman Pfau. An experimental and theoretical guide to strongly interacting Rydberg gases. *Journal of Physics B: Atomic, Molecular and Optical Physics*, 45, 2012.

[57] Mingwu Lu, Nathaniel Q. Burdick, and Benjamin L. Lev. Quantum degenerate dipolar Fermi gas. *Physical Review Letters*, 108(21), 2012.

[58] Mingwu Lu, Nathaniel Q. Burdick, Seo Ho Youn, and Benjamin L. Lev. Strongly dipolar Bose-Einstein condensate of dysprosium. *Physical Review Letters*, 107, 2011.

[59] T. Maier, I. Ferrier-Barbut, H. Kadau, M. Schmitt, M. Wenzel, C. Wink, T. Pfau, K. Jachymski, and P. S. Julienne. Broad universal Feshbach resonances in the chaotic spectrum of dysprosium atoms. *Physical Review A - Atomic, Molecular, and Optical Physics*, 92, 2015.

[60] Thomas Maier. *Interactions in a Quantum Gas of Dysprosium Atoms*. PhD thesis, Physikalisches Institut; Universität Stuttgart, 2015.

[61] G. Edward Marti and Dan M. Stamper-Kurn. Spinor Bose-Einstein gases. *arXiv:1511.01575*, 2015.

[62] A. Mosk, S. Kraft, M. Mudrich, K. Singer, W. Wohlleben, R. Grimm, and M. Weidemüller. Mixture of ultracold lithium and cesium atoms in an optical dipole trap. *Applied Physics B: Lasers and Optics*, 73(8):791–799, 2001.

[63] Abraham J. Olson, Robert J. Niffenegger, and Yong P. Chen. Optimizing the efficiency of evaporative cooling in optical dipole traps. *Physical Review A - Atomic, Molecular, and Optical Physics*, 87, 2013.

[64] R. Onofrio, D. S. Durfee, C. Raman, M. Köhl, C. E. Kuklewicz, and W. Ketterle. Surface Excitations of a Bose-Einstein Condensate. *Physical Review Letters*, 84:810–813, 2000.

[65] Optotune. *Data sheet: EL-10-30-Series*, 2017.

[66] Optotune. Private communication, 2017.

[67] B. Pasquiou, E. Maréchal, L. Vernac, O. Gorceix, and B. Laburthe-Tolra. Thermodynamics of a Bose-Einstein condensate with free magnetization. *Physical Review Letters*, 108(4), 2012.

[68] Benjamin Pasquiou, Alex Bayerle, Slava M. Tzanova, Simon Stellmer, Jacek Szczepkowski, Mark Parigger, Rudolf Grimm, and Florian Schreck. Quantum degenerate mixtures of strontium and rubidium atoms. *Phys. Rev. A*, 88:023601, Aug 2013.

[69] Christopher Pethick and Harry Everett Smith. *Bose-Einstein Condensation in Dilute Gases*. Cambridge University Press, 2008.

[70] Lev Pitaevskii and Sandro Stringari. *Bose-Einstein Condensation and Superfluidity*. Oxford Science Publications, 2016.

[71] Lukas Reichsoellner, Andreas Schindewolf, Tetsu Takekoshi, Rudolf Grimm, and Hanns-Christoph Nägerl. Quantum engineering of a low-entropy gas of heteronuclear bosonic molecules in an optical lattice. *Phys. Rev. Lett.*, 118:073201, Feb 2017.

[72] Zhi-An Ren, Guang-Can Che, Xiao-Li Dong, Jie Yang, Wei Lu, Wei Yi, Xiao-Li Shen, Zheng-Cai Li, Li-Ling Sun, Fang Zhou, and Zhong-Xian Zhao. Superconductivity and phase diagram in iron-based arsenic-oxides ReFeAsO$_{1-\delta}$ (Re = rare-earth metal) without fluorine doping. *EPL (Europhysics Letters)*, 83:17002, 2008.

[73] Jörg G. Ritter, Jan-Hendrik Spille, Tim Kaminski, and Ulrich Kubitscheck. A cylindrical zoom lens unit for adjustable optical sectioning in light sheet microscopy. *Biomedical Optics Express*, 2:185, 2011.

[74] G. R. B. E. Römer and P. Bechtold. Electro-optic and acousto-optic laser beam scanners. *Physics Procedia*, 56:29–39, 2014.

[75] G. Rosi, F. Sorrentino, L. Cacciapuoti, M. Prevedelli, and G. M. Tino. Precision measurement of the Newtonian gravitational constant using cold atoms. *Nature*, 510:518–521, 2014.

[76] S. Saeed, E. M. L. D. de Jong, K. Dohnalova, and T. Gregorkiewicz. Efficient optical extraction of hot-carrier energy. *Nature Communications*, 5, 2014.

[77] J. A. Sauer, K. M. Fortier, M. S. Chang, C. D. Hamley, and M. S. Chapman. Cavity QED with optically transported atoms. *Physical Review A - Atomic, Molecular, and Optical Physics*, 69, 2004.

[78] Stefan Schmid, Gregor Thalhammer, Klaus Winkler, Florian Lang, and Johannes Hecker Denschlag. Long distance transport of ultracold atoms using a 1D optical lattice. *New Journal of Physics*, 8, 2006.

[79] Matthias Scholl. *Probing an ytterbium Bose-Einstein condensate using an ultranarrow optical line : towards artificial gauge fields in optical lattices*. PhD thesis, Université Pierre et Marie Curie, 2015.

[80] Jacob F. Sherson, Christof Weitenberg, Manuel Endres, Marc Cheneau, Immanuel Bloch, and Stefan Kuhr. Single-atom-resolved fluorescence imaging of an atomic Mott insulator. *Nature*, 467:68–72, 2010.

[81] Y. Shin, M. Saba, T. A. Pasquini, W. Ketterle, D. E. Pritchard, and A. E. Leanhardt. Atom interferometry with Bose-Einstein condensates in a double-well potential. *Physical Review Letters*, 92:050405, 2004.

[82] Yijun Tang, Andrew Sykes, Nathaniel Q. Burdick, John L. Bohn, and Benjamin L. Lev. S -wave scattering lengths of the strongly dipolar bosons Dy 162 and Dy 164. *Physical Review A - Atomic, Molecular, and Optical Physics*, 92, 2015.

[83] V. D. Vaidya, J. Tiamsuphat, S. L. Rolston, and J. V. Porto. Degenerate Bose-Fermi mixtures of rubidium and ytterbium. *Phys. Rev. A*, 92:043604, 2015.

[84] Megan T. Valentine, Nicholas R. Guydosh, Braulio Gutiérrez-Medina, Adrian N. Fehr, Johan O. Andreasson, and Steven M. Block. Precision steering of an optical trap by electro-optic deflection. *Optics Letters*, 33:599–601, 2008.

[85] J.H.L. Voncken. *The Rare Earth Elements: An Introduction*. Springer, 2016.

[86] Matthias Wenzel. *A dysprosium quantum gas in highly controllable optical traps*. Master's thesis, Physikalisches Institut; Universität Stuttgart, 2015.

[87] Seo Ho Youn, Mingwu Lu, Ushnish Ray, and Benjamin L. Lev. Dysprosium magneto-optical traps. *Physical Review A - Atomic, Molecular, and Optical Physics*, 82, 2010.

Appendix A

Scanning circuit

This appendix describes the electronic circuit built to combine the signals used to control the acousto-optic deflector. Figure A.1 shows the scheme of the electronic circuit. The central component is the mixer (Analog Devices AD734). This device takes as inputs the signal coming from the arbitrary function generator (AFG) V_{signal}, which gives the modulation function, and the two signals V_{offset} and V_{gain}, used to tune the central RF frequency (f_c) and the modulation amplitude, respectively. A similar electronic circuit was already implemented in a previous experiment [6]. The output of the mixer is given by the following relation [4]

$$V_{mod} = V_{offset} + \frac{V_{signal}V_{gain}}{10V}.$$ (A.1)

V_{offset} and V_{gain} can be tuned in the range $0\,V - 10\,V$. In the circuit the switch enables to choose the central frequency externally or internally rotating the 10-kΩ potentiometer. The VCO[1] receives as input a voltage from the mixer and sends to the AOD a RF signal. The voltage range, needed to achieve an output RF signal wide enough to cover the AOD's bandwidth is $3\,V - 13\,V$. However, the mixer is specified with a maximum output of $10\,V$, thus an operational amplifier (op-amp) is implemented after the mixer. The full range was reached supplying the op-amp with $\pm 21\,V$. On the other hand, to make the circuit compact the op-amp was supplied with the same voltages as the other electronic elements in the circuit. This reduces the voltage range sent to the AOD resulting in a saturation of the maximum beam waist achievable, as shown in Chapter 3. The VCO has a modulation bandwidth of 180 kHz. This quantity plays a fundamental role in the resulting time-averaged potential and can be a limiting factor for the trapping efficiency, as explained in the main text. Thus, in future the VCO will be probably changed with one with higher modulation bandwidth.

---

[1] Model Mini-Circuits ZX95-100.
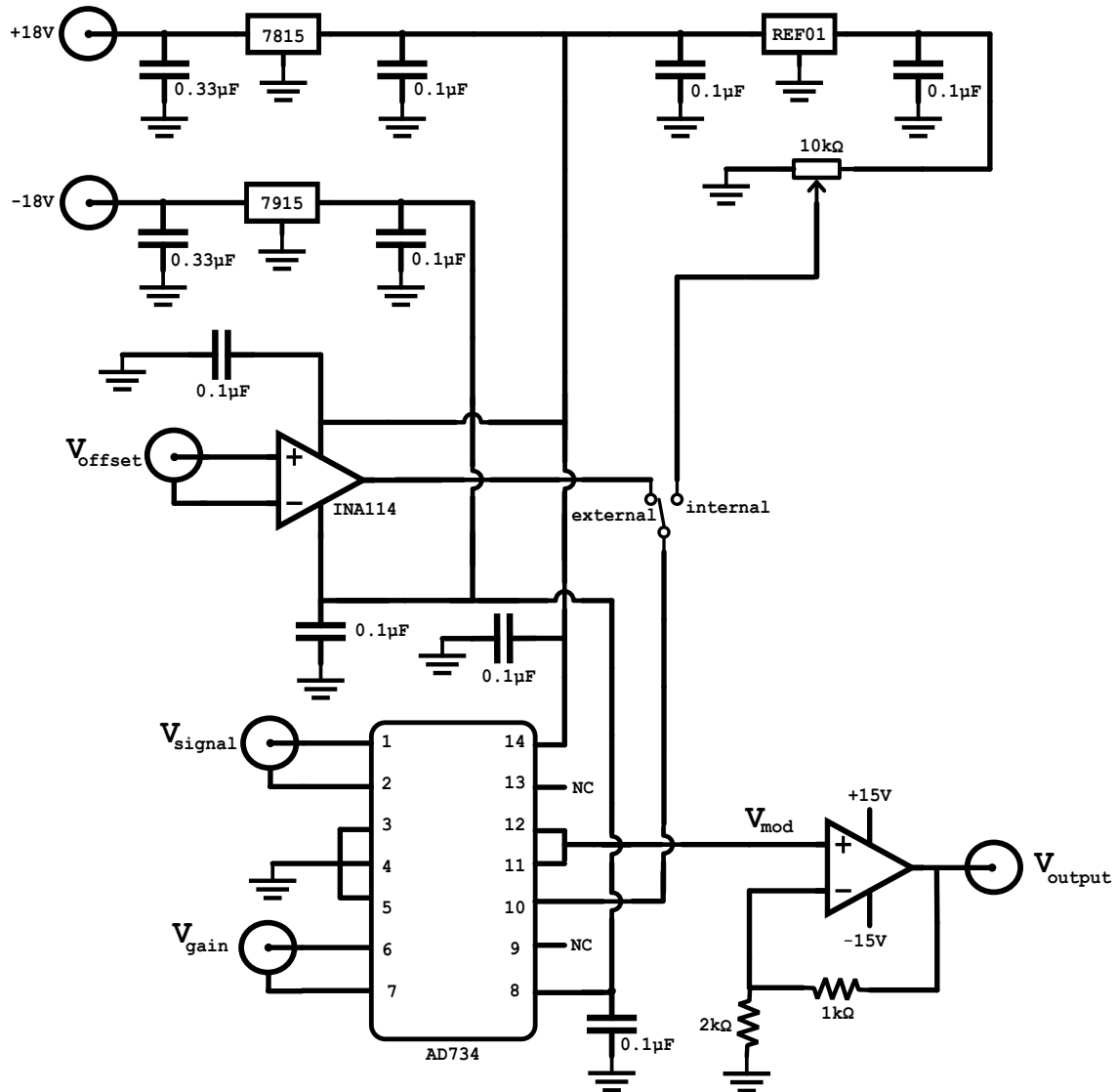
Figure A.1 Electronic circuit implemented to generate the RF signal to control the AOD. The central frequency can be tuned through V_{offset} or through the 10-kΩ potentiometer. The modulation is sent to the circuit from the AFG through V_{signal} and its modulation amplitude is tuned through V_{gain}. The mixer AD734 creates V_{mod} by combining V_{offset}, V_{signal} and V_{gain}. Then, the op-amp OP27 receives V_{mod} and sends V_{output} to the VCO.

Appendix B

Optical transport
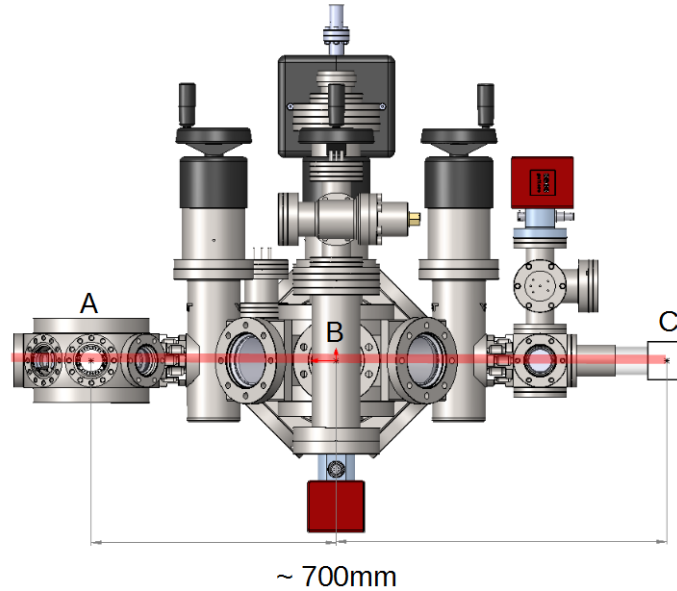
Figure B.1 Side-view of the three chambers of the RARE experimental apparatus. A: Rydberg chamber, B: main chamber and C: single-site imaging chamber.

Figure B.1 shows a side-view of the three chambers that will constitute the RARE experiment. After precooling in the magneto-optical trap and loading into the optical dipole trap, atoms will be optically transported from the main chamber (B) to either the Rydberg chamber (A) or the single-site imaging chamber (C). Even if the latter is not designed yet, the distance from the center of the Rydberg chamber will be approximately $\approx 700\,\text{mm}$. Thus, the optical transport will need a system able to cover the full distance, moving the atoms of $\approx 350\,\text{mm}$ from B in both directions. Optical transport can be performed in several ways. One method relies on the displacement of the focus of a red-detuned Gaussian laser

beam and involves the movement of the focusing lens on a linear stage [38, 60]. Another method involves a one-dimensional optical lattice. In this case the frequencies of the two counter-propagating beams are detuned with respect to each other, resulting in a moving standing wave. The latter is usually used for short displacement [50, 77, 78].

As a possible solution for the optical transport setup we tested the focus-tunable lenses from the company *Optotune*[1] [65]. These lenses are plano-convex with a focal length that can be tuned in the range 100 mm – 200 mm and with an anti-reflection coating which covers the range 700 nm – 1100 nm. A setup with two focus-tunable lenses and an offset lens can be built to reach the requirements of our transport [52]. On the other hand, the tests revealed drifts of the beam position after the change of the focal length. Furthermore, although the damage threshold of the lenses is $10\,\mathrm{kW\,cm^{-2}}$ for 1064-nm light in continuous-wave, the laser beam profile could be affected at a power of $\approx 50\,\mathrm{W}$ [66]. For these reasons we are designing a system which involves the use of a translational stage[2] and a retro-reflector, e. g. two-mirror or a corner-cube retro-reflector [79]. In this way, the laser beam path is folded to save half of the space with respect to the simple scheme in which the last lens, used to focus down the laser beam onto the atoms, is moved on the stage. It is worth noting that, even if the corner-cube is less sensitive to beam fluctuations on both horizontal and vertical planes, small misalignments can strongly affect the polarization of the output beam [39]. This could be a drawback in our case in which, due to the tensorial nature of the atomic polarizability, the polarization of the ODT has to be controlled with high care.

Thus, the optical transport consists in the shift of the focal point of the ODT from position B either to A or to C. This appendix shows simulations performed considering erbium atoms.

In the moving frame, during the transport, atoms are confined by the trapping potential modified by the presence of a new term determined by the acceleration with which the focus is shifted. In particular the effective potential depth is reduced according to the chosen function of the acceleration. The transport axis corresponds to the direction of propagation of the horizontal beam of the ODT, as shown in Fig. 4.2. Thus, from the intensity profile of a Gaussian beam given in Eq. (2.14), for a beam propagating along the *y* axis, the trapping potential during the transport is modified as follows

$$U_{\text{transport}} = \frac{\tilde{U}2P}{\pi w_{\text{h}}^2(y)} \exp\left[-2\left(\frac{r^2}{w_{\text{h}}^2(y)}\right)\right] + may, \qquad (B.1)$$

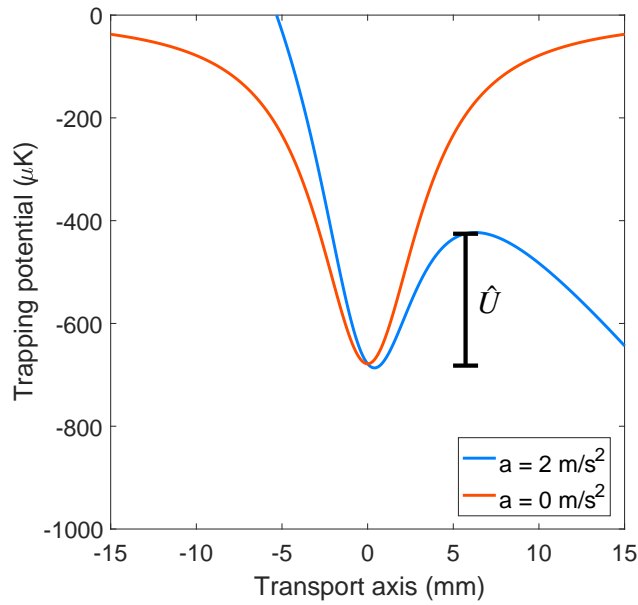[1] Model EL-10-30-CiNIR-LD
[2] Aerotech ABL15040-M-10-NC.

Figure B.2 Trapping potential along the transport axis for a 1064-nm laser beam with power $P = 35\,\text{W}$, waist $w_x = w_z = 35\,\mu\text{m}$. The orange curve shows the potential without any acceleration, whereas the blue curve shows the trapping potential in the case of an acceleration of $a = 2\,\text{m}\,\text{s}^{-2}$. The black bar defines the reduced trap depth $\hat{U}$.

where $r^2 = x^2 + z^2$, $w_\text{h}^2(y) = w_x^2(y) = w_z^2(y)$ and a is the acceleration with which the focus is shifted along the y axis. Figure B.2 shows the trapping potential[3] for a wavelength of $\lambda = 1064\,\text{nm}$, total power $P = 35\,\text{W}$ and a waist of $35\,\mu\text{m}$, without acceleration and with an acceleration of $a = 2\,\text{m}\,\text{s}^{-2}$. The black bar in the figure defines the reduced trap depth $\hat{U}$. In order to not lose atoms during the transport the acceleration function has to be chosen carefully. Figure B.3 presents two of the possible choices, i. e. a trapezoidal and a triangular function, and the corresponding velocity (v) and position (s) of the focus, for a total transport time of 1 s and a total distance of 375 mm. The rising time of the trapezoidal function takes into account that the translational stage will always have a finite response time. The transport time T_t is one of the critical parameters for an optical transport. Usually, T_t is chosen much larger than the oscillation period T_osc, given by the trap frequency along the transport axis ω_y. This situation is referred as adiabatic condition

$$T_\text{t} \gg T_\text{osc} = \frac{2\pi}{\omega_y} \qquad (\simeq 50\,\text{ms} \quad \text{for } v_y = 20\,\text{Hz}). \tag{B.2}$$

In the non-adiabatic regime $T_\text{t} \simeq T_\text{osc}$ energy is transferred to the cloud, leading to heating and oscillations [23]. The choice of the transport time is a trade off between the adiabatic

---

[3]For these simulations, the polarizability values were chosen equal to $^{1064}\text{Re}\{\alpha\} = 166\,\text{a.u.}$, $^{532}\text{Re}\{\alpha\} = 430\,\text{a.u.}$ and $^{1570}\text{Re}\{\alpha\} = 163\,\text{a.u.}$, as reported in Table 2.1 [12].

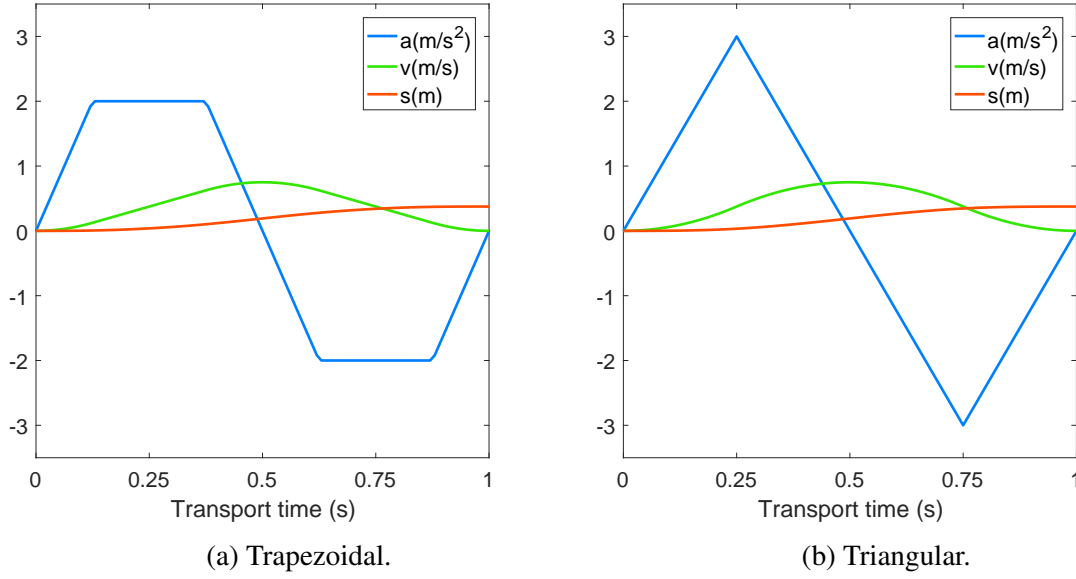(a) Trapezoidal.   (b) Triangular.

Figure B.3 Acceleration, velocity and position curves in the case of a trapezoidal (a) and triangular (b) function of the acceleration.
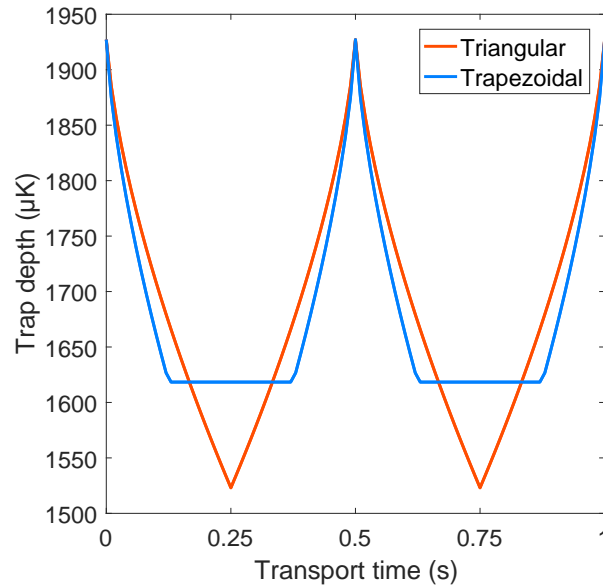

Figure B.4 Trap depth as a function of the transport time for two possible choices: trapezoidal (blue) and triangular (orange) function.

regime and a reasonable time compared with the lifetime of the atomic cloud.

Figure B.4 shows how the trap depth is reduced during the transport for the two configurations previously discussed. In this case the wavelength and the power are the same as in Fig. B.2, while the waist is chosen equal to $w_x = w_z = 20.5\,\mu\text{m}$. Since the distance is fixed by the position of the chambers and the time is approximately given by the adiabatic

condition, an efficient transport relies on the acceleration function. For a triangular shape, higher accelerations are needed to cover the same distance for a given time. Whereas, the trapezoidal function keeps a high value for longer time. Thus, the potential depth is reduced more when the acceleration reaches the maximum in the triangular case. Figure B.5 shows
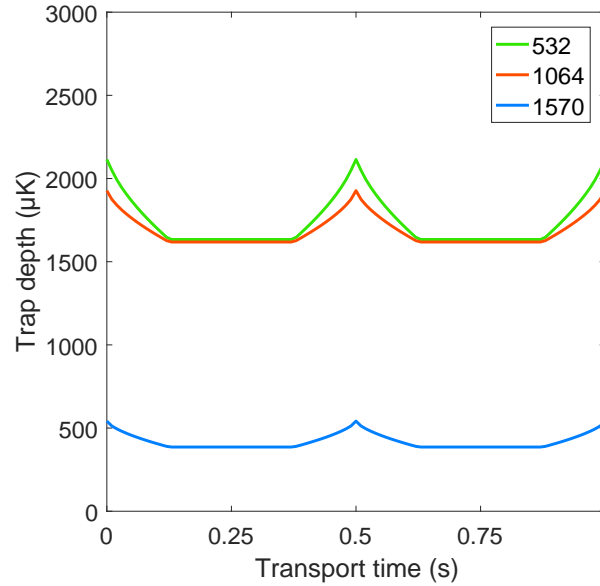
Figure B.5 Trap depth as a function of the transport time, in case of a trapezoidal function of the acceleration, for the wavelengths: 532 nm, 1064 nm and 1570 nm .

the reduction of the potential depth for three different wavelengths for a trapezoidal function of the acceleration. In this simulation the power was set to 10 W, 35 W and 15 W for 1570 nm, 1064 nm and 532 nm, respectively. These are wavelengths suitable for red-detuned optical dipole trap for Er and Dy. The trap depth determined by the available power of the 1570-nm light could not be enough with a waist of 20.5 μm[4] to confine the atoms, if additional heating is transferred to the atomic cloud during the transport. On the other hand, the 532-nm light could be an alternative to the 1064 nm.

---

[4]Due to constraints imposed by the experimental apparatus, however, such small focus would not be achievable with the 1570-nm light.

Acknowledgements

allowing me to recovery before starting my thesis in Innsbruck. Thanks to my sister Giulia for the encouragements and for being my official advisor on everything. Finally, I would like to thank my parents for giving me the possibility to study away from home and for supporting me in every choice I made.